UNIVERSITY OF CALIFORNIA, MERCED

Fast and Three-dimensional Focused X-ray Luminescence Tomography

A dissertation submitted in partial satisfaction of the requirements for the degree Doctor of Philosophy

in

Bioengineering

by

Yile Fang

Committee in charge:
Professor Jennifer Lu, Chair
Professor Joel A. Spencer
Professor Changqing Li

2024

The dissertation of Yile Fang is approved, and it is acceptable in quality and form for publication on microfilm or electronically:

Professor Jennifer Lu, Chair

Professor Joel A. Spencer

Professor Changqing Li

University of California, Merced 2024

This dissertation is dedicated to my family and friends.

TABLE OF CONTENTS

LIST OF SYMBOLS

∇	Gradient operator
$\Phi(\mathbf{r}, p)$	Time-dependent photon density
p	Laplace transform factor
$\mu_a(\mathbf{r})$	Position dependent absorption coefficient
$\mu'_s(\mathbf{r})$	Position dependent reduced scattering coefficient
$\mathbf{r}$	Position vector
$D(\mathbf{r})$	Position dependent diffusion coefficient
c	Velocity of light in the media
$\mathbf{e}_n$	Normal vector at boundary under consideration
$\partial\Omega$	Boundary under consideration
K	Robin boundary coefficient
R_f	Internal reflection coefficient at the boundary
Ω	Domain under consideration
$S_k(\mathbf{r}, p)$	Source term representing the k^{th} X-ray beam illumination pattern
$\eta\mu_{af}(\mathbf{r})$	Light yield of optical contrast agent
$\tau(\mathbf{r})$	Lifetime of the optical contrast agent
$T_k(\mathbf{r})$	X-ray beam intensity distribution
T_0	Initial x-ray beam intensity
$\mathbf{x}_{m,1}(p)$	XLCT contrast agent concentration for a transform factor p
$\mu_x(\mathbf{r})$	X-ray attenuation coefficient at position $\mathbf{r}$
$L(\mathbf{r})$	Distance from x-ray's origin position to current position $\mathbf{r}$

$\mathbf{A}_{n_d \times I \times J,m}(p)$	XLCT System matrix for a transform factor p
$\mathbf{b}_{n_d \times I \times J,1}(p)$	Measurements from XLCT scan for a transform factor p
$\Gamma_j(s)$	Mask prior constraint vector
n_d	Number of detector nodes in finite element mesh
m	Number of XLCT/XFCT finite element nodes/image pixels
I	Number of angular projections in the XLCT scan
J	Number of linear scan steps per angular projection in XLCT scan
$\Phi_{n_d}(p)$	XLCT Sensitivity Matrix for detector node n_d
α, λ	Regularization parameter
L^q	The L^q-norm where ($q \geq 0$)
$\mu_a^{(B)}$	Background optical absorption coefficient
$\tau^{(B)}$	Background lifetime coefficient
$\mu_e(\mathbf{r})$	Linear attenuation coefficient at the X-ray excitation energy for position $\mathbf{r}$
$\mu_f(\mathbf{r})$	Linear attenuation coefficients at the X-ray fluorescent energy for position $\mathbf{r}$
$P_{i,m}$	XFCT Sensitivity Matrix
$F_{j,m}$	XFCT Excitation Matrix
d_n	XFCT discretization number of the detector surface
$\mathbf{A}_{n_d \times I \times J,m}$	XFCT System Matrix
$\mathbf{B}_{n_d \times I \times J,1}$	Measurements from XFCT scan
$\mathbf{X}_{m,1}$	XFCT contrast agent concentration

LIST OF FIGURES

LIST OF TABLES

ACKNOWLEDGEMENTS

First and foremost, I extend my sincerest gratitude to my advisor, Dr. Changqing Li, for entrusting me with the opportunity to contribute to this research endeavor and work in the Biomedical Imaging Lab at the University of California, Merced. His unwavering support and encouragement have been instrumental throughout my graduate studies, continuously fueling my motivation. I am deeply grateful for his provision of resources and opportunities essential for my growth. Under his guidance, I have not only expanded my knowledge but also honed invaluable skills crucial for my future career.

In addition, I am indebted to my esteemed committee members, Dr. Jennifer Lu and Dr. Joel A. Spencer. The time and effort they have contributed to serving as my committee members is truly appreciated.

During my academic journey, I have had the privilege of collaborating with remarkable individuals. Dr. Michael C. Lun's contributions to XLCT system design and methodologies have been indispensable to my research. I extend my heartfelt thanks to Dr. Yiping Guo for her invaluable guidance and support during my transition into graduate studies. Working closely with Dr. Ignacio Romero, I have acquired profound insights into XFCT imaging and GATE simulation. I immensely appreciate their invaluable mentorship and valuable advice on both research and career.

I am sincerely grateful to my colleagues and members of the biomedical imaging lab, including Yibing Zhang, Jarrod Cortez, Casey Hashimoto, Wei Shang, Jason Ngo, Salmanali Mohammad, Kurtis Brent, Steven Soe, Jonathan Soon, and Amir Hojaiji for their unwavering support and camaraderie. Our collaborative efforts have made this journey truly rewarding.

I extend my appreciation to all collaborators, particularly Dr. Jeffrey N. Anker's lab at Clemson University, Dr. Ge Wang's lab at RPI, Dr. Xuecai Ge’s lab at UC Merced, and Vatthana Vongphakham from the department of animal research service UC Merced, whose collaborations have significantly enriched this work.

I am grateful to the Society of Photo-Optical Instrumentation Engineers (SPIE), IOS Press, the Optical Society of America (OSA), and the American Association of Physicists in Medicine (AAPM) for granting permissions to utilize copyrighted materials in this dissertation.

I acknowledge the support of various grants and funds, including those from the National Institutes of Health (NIH) under Dr. Li's leadership [EB026646 and R42GM142394], the summer fellowships from the Bioengineering graduate program of UC Merced, the MacKenzie Scott Graduate Student Supplemental Travel Award from the Graduate Council of UC Merced, and the student travel fellowship from the Northern California Chapter of the AAPM.

I would like to express my gratitude to Quanpeng Yang, Sikai Yang, Yuning Chen, Anqi Li, Jianan Chen, Jingyi Zhang, Jinzhao Wang, and Bin Ma, who have shown precious

friendship and support during my time in Merced.

Lastly, I express my deepest gratitude to my family for their unwavering support. I'm proud to be the second Dr. Fang in the family, and I'm so lucky to have such great parents always at my back. Special thanks to my twin sister, Yifang, for her unconditional support, understanding, companionship, and encouragement. I cannot think of a better family to live with, and your love has been a constant source of inspiration. I love you all.

CURRICULUM VITAE

Education

University of California, Merced. Merced, CA, USA. (2019-2024)

- Ph.D. in Bioengineering
- Supervised by Professor Changqing Li
- Imaging system design and integration
- Imaging processing

Beijing University of Posts and Telecommunications. Beijing, China. (2012-2016)

- B.E. in Communication Engineering
- Signal processing
- Pattern Recognition

Publications

Peer-Reviewed

J1. M. C. Lun, M. Ranasinghe, M. Arifuzzaman, **Y. Fang**, Y. Guo, J.N. Anker, C. Li, "Contrast agents for x-ray luminescence computed tomography," Appl. Opt., vol. 60, no. 23, p. 6769, Aug. 2021, doi: 10.1364/AO.431080.

J2. I. O. Romero, **Y. Fang**, M. Lun, and C. Li, "X-ray Fluorescence Computed Tomography (XFCT) Imaging with a Superfine Pencil Beam X-ray Source," Photonics, vol. 8, no. 7, p. 236, Jun. 2021, doi: 10.3390/photonics8070236.

J3. I. O. Romero, **Y. Fang**, and C. Li, "Correlation between X-ray tube current exposure time and X-ray photon number in GATE," XST, vol. 30, no. 4, pp. 667–675, Aug. 2022, doi: 10.3233/XST-221126.

J4. **Y. Fang**, Y. Zhang, M. C. Lun, and C. Li, "Superfast Scan of Focused X-Ray Luminescence Computed Tomography Imaging," IEEE Access, vol. 11, pp. 134183–134190, 2023, doi: 10.1109/ACCESS.2023.3336615.

J5. **Y Fang**, Y Zhang, MC Lun, C Li, "Evaluations of Quantitative Accuracy and Spatial Resolution Imaging Investigations of a Multichannel X-ray Luminescence Computed Tomography System," (drafted).

J6. **Y Fang**, Y Zhang, MC Lun, JN Anker, G Wang, C Li, "Three-dimensional Focused X-ray Luminescence Tomography: In vivo Imaging of Mice with Xenografted Tumors," (drafted).

Conference Proceedings

C1. M. C. Lun, **Y. Fang**, and C. Li, "Fast three-dimensional focused x-ray luminescence computed tomography," in Medical Imaging 2021: Biomedical Applications in Molecular, Structural, and Functional Imaging, B. S. Gimi and A. Krol, Eds., Online Only, United States: SPIE, Feb. 2021, p. 44. doi: 10.1117/12.2584335.

C2. I. Romero, **Y. Fang**, M. C. Lun, and C. Li, "Benchtop x-ray fluorescence computed tomography (XFCT) imaging," in Medical Imaging 2021: Biomedical Applications in Molecular, Structural, and Functional Imaging, B. S. Gimi and A. Krol, Eds., Online Only, United States: SPIE, Feb. 2021, p. 38. doi: 10.1117/12.2584577.

C3. M. C. Lun, **Y. Fang**, and C. Li, "Focused X-ray Luminescence Computed Tomography using a Continuous Scanning Scheme," Bioengineering, preprint, Feb. 2021. doi: 10.1101/2021.02.04.429805.

C4. **Y. Fang**, M. C. Lun, Y. Zhang, J. N. Anker, G. Wang, and C. Li, "Super-fast three-dimensional focused x-ray luminescence computed tomography with a gated photon counter," in Medical Imaging 2022: Biomedical Applications in Molecular, Structural, and Functional Imaging, B. S. Gimi and A. Krol, Eds., San Diego, United States: SPIE, Apr. 2022, p. 8. doi: 10.1117/12.2613157.

C5. Y. Zhang, **Y. Fang**, V. Abbaraju, S. Bhattacharya, J.N. Anker, G. Wang, C. Li, "Oxygenation imaging in deep tissue with x-ray luminescence computed tomography (XLCT)," in Medical Imaging 2023: Biomedical Applications in Molecular, Structural, and Functional Imaging, B. S. Gimi and A. Krol, Eds., San Diego, United States: SPIE, Apr. 2023, p. 16. doi: 10.1117/12.2654446.

C6. **Y. Fang**, Y. Zhang, M. C. Lun, J. N. Anker, G. Wang, and C. Li, "Development of fast and three-dimensional focused x-ray luminescence tomography system," in Medical Imaging 2023: Biomedical Applications in Molecular, Structural, and Functional Imaging, B. S. Gimi and A. Krol, Eds., San Diego, United States: SPIE, Apr. 2023, p. 34. doi: 10.1117/12.2654091.

C7. **Y. Fang**, Y. Zhang, and C. Li, "Quantitative study of x-ray luminescence computed tomography," in Medical Imaging 2024: Clinical and Biomedical Imaging, B. S. Gimi and A. Krol, Eds., San Diego, United States: SPIE, Apr. 2024, p. 37. doi: 10.1117/12.3009033.

Conference and Symposium Presentations

P1. **Y. Fang**, M. C. Lun, Y. Zhang, J. N. Anker, G. Wang, and C. Li, *et al*., "Super-fast three-dimensional focused x-ray luminescence computed tomography with a gated photon counter," SPIE Medical Imaging Conference, San Diego, CA, Feb. 2022 (Oral Presentation).

P2. **Y. Fang**, Y. Zhang, C. Li, "Fast X-ray Luminescence Computed Tomography Imaging using a Continuous Scanning Scheme," UC Merced BIOE 2022 Young Investigator Symposium, Merced, CA, Apr. 2022 (Oral Presentation).

P3. **Y. Fang**, Y. Zhang, M. C. Lun, C. Li, "Fast and High Spatial Resolution X-ray Luminescence Computed Tomography Imaging," Northern California AAPM Chapter 2022 Young Investigators Symposium, Walnut Creek, CA, May. 2022 (Oral Presentation).

P4. **Y. Fang**, Y. Zhang, J. N. Anker, G. Wang, and C. Li, *et al*., "High Spatial Resolution Three-dimensional X-ray Luminescence Computed Tomography

Imaging," 22nd Annual UC Systemwide Bioengineering Symposium, Santa Barbara, CA, Aug. 2022 (Oral Presentation).

P5. **Y. Fang**, Y. Zhang, M. C. Lun, J. N. Anker, G. Wang, and C. Li, "Development of fast and three-dimensional focused x-ray luminescence tomography system," SPIE Medical Imaging Conference, San Diego, CA, Feb. 2023 (Oral Presentation).

P6. **Y. Fang**, Y. Zhang, C. Li, "Development of Fast X-ray Luminescence Computed Tomography Imaging," UC Merced BIOE 2023 Young Investigator Symposium, Merced, CA, Apr. 2023 (Oral Presentation).

P7. **Y. Fang**, Y. Zhang, M. C. Lun, J. N. Anker, G. Wang, and C. Li, "Three-dimensional focused x-ray luminescence tomography Imaging for small animals," Northern California AAPM Chapter 2023 Young Investigators Symposium, San Francisco, CA, May. 2023 (Oral Presentation).

P8. **Y. Fang**, Y. Zhang, M. C. Lun, J. N. Anker, G. Wang, and C. Li, "Whirling Wonders: A Rotary Gantry to Rescue Small Animals from a Skewer Stick in X-ray Luminescence Imaging," 65th AAPM annual meeting, Houston, TX, Jul. 2023 (Oral Presentation).

P9. **Y. Fang**, Y. Zhang, C. Li, "Quantitative Study of X-ray Luminescence Computed Tomography," SPIE Medical Imaging Conference, San Diego, CA, Feb. 2024 (Oral Presentation).

P10. **Y. Fang**, Y. Zhang, M. C. Lun, J. N. Anker, G. Wang, and C. Li, "Three-dimensional Focused X-ray Luminescence Tomography: In vivo Imaging of Mice with Xenografted Tumors," Northern California AAPM Chapter 2024 Young Investigators Symposium, Davis, CA, May. 2024 (Oral Presentation).

Scholarships and Honors

H1. 2023 May: 1st place award in SLAM competition, Northern California AAPM Chapter, USA

H2. 2023 May: 2nd place award of the graduate student presentations, Northern California AAPM Chapter, USA

H3. 2020-2023: Bioengineering summer research fellowship, UC Merced, USA

H4. 2015 April: Honorable Mention, Mathematical Contest in Modeling, USA

H5. 2013-2015: Chang Lin Foundation Endeavor Scholarship, BUPT, China

H6. 2013 December: 2nd Prize, 30th National Reginal College Students Physics Competition, China

H7. 2013 November: 2nd Prize, 5th Chinese Mathematics Competitions, China

ABSTRACT

Fast and Three-dimensional Focused X-ray Luminescence Tomography
Ph.D. Dissertation by **Yile Fang**
University of California, Merced, 2024
Bioengineering
Ph.D. Advisor: **Professor Changqing Li**

X-ray luminescence computed tomography (XLCT) is a hybrid molecular imaging modality with the merits of both x-ray imaging (high spatial resolution) and optical imaging (high sensitivity to trace nanophosphors). Narrow x-ray beam based XLCT imaging has shown promise for both the high spatial resolution of X-ray imaging and high molecular sensitivity of optical imaging. However, its slow scan speed limits its applications for in vivo and three-dimensional imaging.

We have improved the imaging speed of the pencil beam based XLCT by introducing a fly-scanning scheme. In the fly-scanning scheme, the main factor limiting the scanning speed is the data acquisition time at each interval position. To further increase the imaging speed, we used a gated photon counter (SR400, Stanford Research Systems) to replace the high-speed oscilloscope (MDO3104, Tektronix) to acquire measurement data. The photon counter records much less data without losing acquired signals (the peaks). We have achieved 43 seconds per transverse scan, which is 28.6 times faster than before without compromising the XLCT image quality.

To perform quantitative study of pencil beam XLCT in imaging x-ray excitable nanophosphor targets in deep scattering media, we then have scanned a cylindrical agar phantom containing twelve targets filled in with three different phosphor concentrations (2.5 mg/ml, 5 mg/ml, and 10 mg/ml) using an upgraded XLCT imaging system in our laboratory. We have, for the first time, quantitatively analyzed the reconstructed phosphor concentrations of deep targets of pencil beam XLCT and evaluated the performance of filtered back-projection (FBP) algorithm using setups of one, two, and four detectors. Then we have scanned phantoms with 3D printed targets and obtain 3D functional images and 3D structural images simultaneously.

Then, based on all the work we have done in XLCT imaging, we have designed, built and developed a first-of-its-kind three-dimensional focused X-ray luminescence tomography (FXLT) imaging system for small animals. There is a co-registered cone beam based microCT imaging system using a cone beam X-ray tube. We are able to perform both FXLT imaging and a pencil beam based microCT using the superfine focused X-ray tube. The system is specially designed for in vivo imaging of small animals. All the major devices rotate on a powerful rotary gantry while the small animals lie down and keep stationary on a linear stage. We developed a lab-made C++ program to control and automate all data acquisition. We applied a high scanning speed method to obtain high-resolution 3D XLCT images in a reasonable time. To evaluate the performance of the FXLT system, we performed both 2D phantom experiments and 3D phantom experiments and achieved good DICE coefficient.

In the end, we have performed mice experiments using the proposed FXLT imaging

system. We first have scanned two euthanized nude mice with glass capillary tube targets of different sizes filled with phosphor particles. Then we scanned a live nude mouse with two xenografted tumors for in vivo imaging at four different transverse slices. Before scanning, for each tumor, we intratumorally administrated 0.1 mL of nanoparticle $Gd_2O_2S:Eu^{3+}$ solution at a concentration of 1 mg/mL. After the in vivo experiment, the mouse was euthanized. Then, we performed a 10-slice FXLT scan of the euthanized mouse. After all the scans were finished, the tumors were sliced and imaged with an electron-multiplying charged coupled device (EMCCD) camera when excited by a cone beam X-ray tube. Finally, the tumor slices were also scanned by an optical microscope for cross validation. We have, for the first time, reconstructed 3D in vivo XLCT images of nanoparticles at superhigh resolution, which demonstrated that the FXLT system is a power tool in molecular imaging and has the capabilities of performing in vivo and 3D imaging for small animals.

CHAPTER 1

INTRODUCTION TO BIOMEDICAL IMAGING AND X- RAY LUMINESCENCE COMPUTED TOMOGRAPHY IMAGING, AND X-RAY FLUORESCENCE COMPUTED TOMOGRAPHY

1.1 Introduction

As per the National Institutes of Health (NIH), biomedical imaging encompasses the realm of medicine dedicated to developing and utilizing imaging devices and techniques for acquiring internal anatomical images and conducting biochemical and physiological analyses of tissues and organs. Notably, the discovery of x-rays by German physicist Wilhelm Roentgen in 1895 stands as a pivotal moment in medical imaging [1]. Since then, the field has witnessed remarkable growth, witnessing the introduction of numerous innovative techniques and instruments. This chapter will delve into several popular imaging modalities, followed by an exploration of x-ray luminescence computed tomography (XLCT) and X-ray Fluorescence computed tomography (XFCT).

1.2 Review of Biomedical Imaging Modalities

This section will cover various imaging modalities, beginning with x-rays and their medical applications. It will then explore other popular modalities such as magnetic resonance imaging (MRI), nuclear imaging techniques, and optical imaging methods. Additionally, it will discuss multiple-modality and hybrid imaging methods.

X-rays, discovered shortly after Roentgen's breakthrough, were swiftly employed for clinical and diagnostic purposes. They function as electromagnetic radiation, akin to visible light, and can be understood as either electromagnetic waves or individual photons. In most x-ray imaging techniques, the premise is that as x-rays traverse and penetrate the body or imaging sample, there is minimal scattering, allowing for precise object localization within tissue. The resulting image contrast is formed by the differential attenuation of x-rays. The initial use of x-rays in medical imaging gave rise to radiography, primarily two-dimensional projection imaging. Subsequent advancements led to the development of other x-ray imaging methods such as fluoroscopy, enabling real-time visualization of x-ray projection images, and x-ray angiography, which utilizes iodine-based contrast agents for visualizing blood vessels [2]. The most prevalent x-ray modality today is computed tomography (CT), pioneered by Sir Godfrey N. Hounsfield

and Allan M. Cormack in 1971 [3]. CT offers high-spatial resolution 3D images and is indispensable in both preclinical and clinical studies. However, its contrast mechanism, based on attenuation, lacks sensitivity in differentiating soft tissues and probing molecular features. Moreover, typical x-ray contrast agents are unsuitable for molecular imaging due to their viscosity and osmolality limitations [4].

Magnetic resonance imaging (MRI), introduced clinically in 1977, provides superior soft tissue contrast compared to CT [5]. It offers functional information by exploiting proton density, perfusion, diffusion, and biochemical contrasts, enabling the co-registration of molecular and anatomical information in a single modality. MRI delivers high-spatial resolution and deep tissue penetration but suffers from low sensitivity in detecting targeted contrast agents and negative contrast limitations [6]. Additionally, MRI scanners are costly and large.

Nuclear medicine imaging techniques such as positron emission tomography (PET) and single photon emission computed tomography (SPECT) employ radiotracers injected into the subject to gather tissue function information crucial for diagnosing malignancies [7]. Various radiotracers, including fluorodeoxyglucose 18 (FDG-18) for PET imaging and Technetium 99m for SPECT imaging, are available to map molecular processes. In PET imaging, FDG-18 tracks glucose metabolism through positron decay, generating gamma rays upon positron annihilation, while SPECT imaging utilizes Technetium 99m for perfusion studies, detecting gamma rays emitted during gamma decay. Reconstruction of PET and SPECT images can be achieved using algorithms like filtered back projection or statistical methods [8]. Despite their high sensitivity and imaging depth, PET and SPECT have limitations in spatial resolution, with PET reaching approximately 0.7 mm, close to its physical limits [9].

Optical imaging methods offer valuable insights into cellular-level activities with high sensitivity and spatial resolution at shallow depths. Fluorescence and bioluminescence imaging, predominant in preclinical research, are favored for their mature technology, affordability, and non-ionizing radiation properties [10, 11]. Near-infrared optical photons enable deep tissue imaging up to 10 cm, with techniques like two-photon microscopy achieving a lateral resolution of 0.64 μm [12, 13]. However, optical imaging's spatial resolution is often compromised by tissue scattering, particularly for targets deeper than 2 mm, and its quantification is hindered by uncertainty in tissue optical properties [14]. Ongoing efforts focus on enhancing spatial resolution and quantification through experimental systems and reconstruction algorithms [15, 16].

Recently, hybrid imaging modalities integrated molecular and anatomical imaging techniques to overcome individual modality limitations. Examples include PET/CT, SPECT/CT, and PET-MRI, combining high sensitivity with high spatial resolution or contrast [9, 17, 18]. Additionally, emerging hybrid modalities like X-ray luminescence computed tomography (XLCT) and X-ray fluorescence computed tomography (XFCT) aim to provide complementary information and will be further explored in subsequent section.

1.3 Review of X-ray Luminescence Computed Tomography (XLCT)

This section begins by examining the phenomenon of x-ray luminescence, followed by an exploration of its applications in imaging, particularly focusing on x-ray-induced luminescence imaging, with an emphasis on XLCT imaging.

1.3.1 The X-ray Luminescence process

X-ray luminescence (XL) is a scintillation process wherein the absorption of an X-ray photon stimulates the emission of optical photons. Scintillator materials, comprising high Z nanoparticles with phosphor groups, facilitate this emission of optical photons [19]. In scintillating materials, X-rays from an excitation beam deposit their energy, ionizing the atoms in the material and releasing electrons with high kinetic energy. These high-energy electrons then ionize other atoms, resulting in a cascade of lower-energy electrons. These lower-energy electrons migrate to luminescent centers within the material, leading to transient electronic excitations. Upon electronic relaxation, optical photons are emitted. In non-scintillating materials, lower-energy electrons release energy as heat instead of migrating to luminescent centers. The XL process is highly sensitive as it emits thousands of optical photons per absorbed X-ray [20]. This process serves as the fundamental principle for radiation detectors employing scintillating material to detect ionizing radiation.

1.3.2 X-ray Luminescence Computed Tomography (XLCT)

X-ray Luminescence imaging was initially demonstrated as a 2D chemical imaging modality by Chen et al., where lanthanide-doped phosphor concentrations in thin pork tissues were imaged [21, 22]. XLCT imaging integrates XL principles with tomographic imaging, enabling the reconstruction of 3D distributions of luminescent phosphors within a biological medium. XLCT imaging, a hybrid modality, combines the high contrast of optical imaging with the high spatial resolution of CT imaging. The principle of XLCT imaging involves sequential scanning of the imaging object with a collimated X-ray beam at each rotational position, akin to the 'scan and shoot' method in first-generation CT imaging. Upon X-ray excitation, luminescent contrast agents emit optical photons, which are measured by sensitive detectors like electron multiplying charge coupled devices (EMCCDs) or photomultiplier tubes (PMTs) placed on the object's surface. Simultaneously, a CT image is acquired with an X-ray detector to provide an anatomical reference image. Unlike optical imaging, XLCT utilizes X-rays to excite the luminescent targets, overcoming major limitations imposed by optical imaging. X-rays can excite contrast agents in thicker samples without easy scattering, and the spatial information is provided along the X-ray beam line, overcoming strong optical scattering limitations in deep tissues [23]. Image resolution in XLCT is primarily limited by X-ray beam collimation [24].

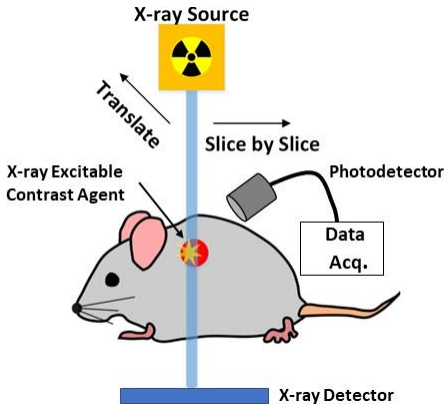

Figure 1.1. Schematic of a typical X-ray luminescence computed tomography (XLCT) imaging system.

The feasibility of XLCT imaging was initially demonstrated by Pratx et al. in 2010 using a selective excitation-based (pencil beam) imaging approach to scan a 4.5 cm diameter cylindrical phantom composed of tissue-equivalent material embedded with nanophosphor targets. Sub-picomolar sensitivity was achieved with 1 cGy of radiation dose and a spatial resolution of 1 mm [20, 25]. However, significant X-ray scatter in tissue excited nanophosphors outside the beam volume, increasing noise and limiting sensitivity. Cong et al. explored the feasibility of a scatter-estimating forward model, improving image quality by considering X-ray scattering effects in the reconstruction algorithm [26]. In the same study, they simulated multiplexing to image multiple luminescent contrast agents simultaneously. Carpenter et al. demonstrated in vivo multiplex XLCT imaging on a mouse with nanoparticles doped with different lanthanides [27]. To reduce the scan time of pencil beam imaging protocols, Li et al. proposed a limited angle tomographic approach, showing that two orthogonal projections were sufficient to reconstruct phosphor contrast agents within the imaging object [28].

The pencil-beam-based XLCT imaging method achieves high spatial resolution images but suffers from lengthy scan times due to its sequential line excitation imaging protocol. To address this issue, alternative imaging geometries have been investigated, such as cone beam and fan beam imaging geometries. Chen et al. proposed cone X-ray beam XLCT imaging, wherein the entire imaging object is irradiated, significantly reducing scan time [29]. However, this reduction in scan time comes at the expense of degraded image resolution for deep targets, as the structural guidance in image reconstruction from selective excitation is compromised. Various methods have been explored to enhance image spatial resolution and mitigate the ill-posed nature of XLCT imaging reconstruction with cone beam XLCT imaging. Zheng et al. introduced a Gaussian Markov field model with a Bayesian method approach, demonstrating improved image quality compared to conventional methods [30]. Liu et al. proposed a compressed sensing method, achieving a target location error of 1.5 mm with single-view data from an in-vivo mouse imaging study [31]. Tzoumas et al. applied a coded aperture compressed sensing method, reporting better spatial resolution than conventional cone beam methods with Tikhonov regularization [32]. Additionally, Liu et al. utilized a wavelet-based single-view approach to accelerate image reconstruction, resulting in a target location error of 0.8 mm [33].

Another potential X-ray beam geometry is the fan or sheet-beam-based XLCT imaging. Cong et al. proposed the fan-beam X-ray geometry for XLCT imaging, demonstrating through numerical simulation studies that it offers faster measurement

times compared to narrow-beam methods, with less spatial resolution loss [34]. Chen et al. proposed a reconstruction algorithm based on an X-ray distribution model and adaptively split Bregman method for fan-beam-based XLCT, achieving a location error of approximately 1.1 mm in experimental studies [35]. Quigley et al. introduced a selective-plane sheet-beam XLCT imaging method using a slit collimator, resolving two targets separated by 1 cm up to a depth of 1.75 cm in a turbid media phantom [36].

Despite extensive efforts with both cone-beam-based XLCT and fan-beam-based XLCT, the selective excitation strategy of the narrow-beam approach still provides an advantage in terms of achievable spatial resolution. This dissertation will primarily focus on enhancing pencil-beam-based XLCT imaging, as detailed in the following chapters.

1.4 Review of X-ray Fluorescence Computed Tomography

This section introduced and reviewed the second hybrid functional X-ray imaging modality. This section begins by examining the X-ray fluorescence process, followed by the application for this process: X-ray fluorescence computed tomography (XFCT).

1.4.1 The X-ray Fluorescence process

X-ray fluorescence (XF) occurs through the photoelectric effect, where an inner shell electron in the K or L shells of a high Z material is ejected upon absorbing an X-ray photon. Subsequently, an outer shell electron fills the vacancy, emitting a characteristic (fluorescent) X-ray with discrete energies. These energies are unique to each element and are always lower than the incident X-ray beam's energy that induced the fluorescence. XF has been extensively utilized to characterize a material's elemental composition, typically employing energy dispersive detectors. The intensity of fluorescent X-rays peaks when the excitation beam's energy slightly exceeds the L-edge or K-edge of the target element, where X-ray absorption is notably increased. While fluorescent energies resulting from X-ray absorption above the L-edge are lower than those above the K-edge, L-shell X-rays exhibit higher intensity due to their larger cross section compared to K-edge absorption. However, XF is less sensitive than X-ray luminescence (XL) since only one fluorescent X-ray is emitted per absorbed X-ray.

1.4.2 X-ray Fluorescence Computed Tomography (XFCT)

X-ray fluorescence imaging serves to nondestructively identify chemical species within a sample. XFCT imaging integrates XF principles with tomographic imaging to reconstruct the 3D elemental distribution within the object. This hybrid modality combines CT imaging's high spatial resolution with X-ray fluorescence imaging's material analysis capabilities. A pencil beam imaging protocol akin to pencil beam XLCT imaging is employed in XFCT imaging. For each rotational position, the object undergoes sequential scanning with a collimated X-ray beam. An energy-resolving detector measures the fluorescent X-rays, while an X-ray detector simultaneously acquires an anatomical reference image.

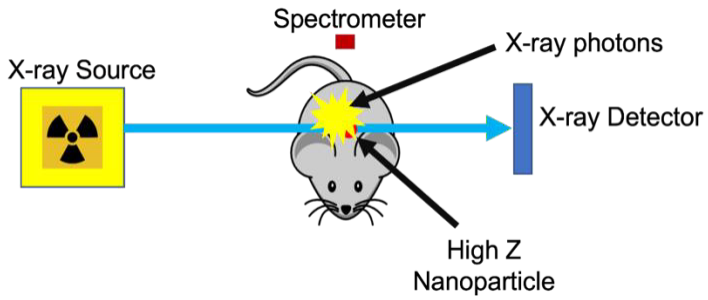

Figure 1.2. Schematic of a typical X-ray fluorescence computed tomography (XFCT) imaging principle.

XFCT imaging was initially showcased in 1987 by Boisseau et al. using synchrotron X-ray sources at Brookhaven National Laboratories, achieving micrometer spatial resolutions to image trace elements like titanium and iron in glass fibers and a bee [37]. Takeda et al. further demonstrated in vivo and ex vivo XFCT imaging to visualize the distribution of an iodine contrast agent in mouse brains [38]. While synchrotron sources offer bright monochromatic X-ray energies, ideal for tuning just above the K-edge or L-edge absorption energies of the target element, they are costly and not easily accessible.

In 2010, Cheong et al. introduced benchtop XFCT imaging using conventional laboratory X-ray sources, successfully imaging a 5 cm diameter cylindrical object with gold nanoparticles (AuNPs) targets via a pencil beam imaging approach with a collimator [39]. This pioneering study implemented K-edge XFCT imaging and reconstructed AuNPs distribution at relatively low concentrations (10 mg/ml) using a polychromatic X-ray source and a single detector. Subsequently, Bazalova et al. utilized numerical simulations in 2012 to compare conventional CT, K-edge CT, and XFCT, finding greater sensitivity with XFCT at the same dose [40]. In 2013, Kuang et al. demonstrated multiplex XFCT imaging of Au, Gadolinium (Gd), and Barium (Ba) targets in a 3.5 cm diameter water phantom using a 5 mm pencil beam X-ray source [41].

Similar to pencil beam XLCT imaging, pencil beam XFCT imaging offers high spatial resolution and sensitivity, albeit with a challenge posed by long scan times. Jones et al. experimentally showcased cone beam XFCT imaging, using a pinhole collimator to remove Compton scatter and improve resolution when imaging a 5 cm diameter phantom with 5-10 mm diameter AuNPs targets [42]. However, resolution is constrained by the pinhole size. Fu et al. demonstrated selective-plane (fan beam) XFCT imaging experimentally, employing a collimator slit and position-sensitive detector to image trace metals in biological samples with a synchrotron source [43]. Nonetheless, the authors acknowledged that long scan times would still be required, especially when imaging with a polychromatic source. In both geometries, the potential reduction in scan times comes at the expense of sensitivity.

While fan beam and cone beam scanning geometries offer dose and acquisition speed advantages [44], the pencil beam scanning approach provides the best spatial resolution and sensitivity for detecting smaller probe concentrations [45]. This dissertation focuses on refining the pencil beam imaging protocol.

To enhance sensitivity in XFCT imaging, benchtop systems have adopted X-ray sources with greater intensity and a narrower energy spectrum [46]. Traditional narrow collimators are inefficient, prompting exploration of alternative methods like liquid anode X-ray sources [47] and internally reflective lenses [48]. Additionally, advancements in inverse Compton scattering sources and free electron lasers are expected to yield synchrotron radiation with smaller facilities in the future [49].

Compton scatter poses a challenge to sensitivity in benchtop XFCT imaging, but system design optimizations, such as back-scatter configurations and background signal acquisition, can mitigate its effects [50]. Interpolation techniques can further remove scatter contributions from fluorescent signals [41].

XFCT imaging with K-shell fluorescence energies may be suitable for whole-body imaging due to its greater penetrability, but L-shell emission energies offer higher sensitivity [51]. Recent studies have demonstrated significant progress in L-shell XFCT imaging, with advancements in X-ray optic lenses reducing imaging times substantially [52].

While L-shell XFCT imaging is primarily limited to preclinical applications and organ-specific imaging due to biological tissue attenuation [53], the use of lower energy X-ray beams makes it more accessible for laboratory use.

1.5 X-ray Excitable Contrast Agents

XLCT imaging primarily relies on exogenous agents, with rare-earth nanoprobes extensively studied as contrast agents [54]. These nanoprobes, typically consisting of lanthanide-doped materials encased in a non-doped shell, offer promising applications. For instance, Gadolinium oxysulfide (GOS) doped with Eu or Tb is favored in X-ray detectors due to its high diagnostic energy X-ray cross-section and light yield [55]. Nanoscale particles like GOS:Eu^{3+} and NaGdF4:Eu, doped with lanthanides, emit light at wavelengths optimal for tissue penetration, typically around 710 nm [56]. Coating these nanoparticles with a plasmonic gold shell enhances their biocompatibility [57, 58]. Numerous studies, including those by Karanthanasis et al. and Hainfeld et al., have reported on the synthesis of efficient Eu^{3+} doped X-ray excitable nanophosphors [57, 59].

XFCT imaging employs various contrast agents, including exogenous agents, metal-based therapeutics, and endogenous contrast agents. Exogenous agents, such as high Z nanoparticles, offer versatility without hindering molecular target affinity [53]. Metal-based therapeutics enable visualizing drug distribution in tissues, aiding in understanding drug metabolism and therapy response [60, 61]. Endogenous contrast agents, observed to be linked to diseases, demonstrate heightened sensitivity when utilized with synchrotron radiation [62, 63]. This dissertation emphasizes exogenous contrast agents for XFCT imaging due to their lower excitation energies compared to other agents.

High Z nanoparticles, notably Molybdenum (Mo) and Gold (Au) nanoparticles (NPs), are prominent in XFCT imaging [64, 65]. Their K-shell and L-shell emission energies offer deeper tissue imaging compared to optical emissions from scintillation nanoprobe counterparts. The K-shell characteristic energies for Mo (17.48 keV and 19.61 keV) and the L-shell energies for Au (9.71 keV and 11.44 keV) align with typical laboratory X-ray source capabilities [68, 69]. These nanoparticles exhibit high biocompatibility, enabling increased injection doses with reduced cell toxicity concerns. They serve as both CT and functional imaging contrast agents, often employed as passive targeting agents in cancer imaging due to the enhanced permeability and retention (EPR) effects of tumors [65-68].

1.6 Dissertation Outline

In the following chapters, I discuss advancements made towards pencil-beam-based XLCT imaging and XFCT imaging methods.

Chapter 2 discusses the new scanning schemes based on the photon counter detector and a fly-scanning method that can achieve a superfast scan of focused XLCT imaging [69-72]. The system improvements and scanning strategies are presented, and results are compared to conventional run-and-shoot scanning scheme. The parallel beam CT imaging is performed with the XLCT imaging simultaneously in this study.

Chapter 3 discusses a quantitative study of pencil-beam-based XLCT imaging. The system set-up and phantom design are reported [73]. The experimental results are analyzed quantitatively on the correlations between the reconstructed signals of the phosphor targets and the target concentrations. The DICE similarity coefficients are also calculated and compared with set-ups of different number of detectors.

Chapter 4 discusses a first-of-its-kind fast and three-dimensional Focused X-ray Luminescence Tomography (FXLT) imaging system we built and developed based on our previous XLCT work [74]. There is a co-registered cone-beam-based microCT imaging system with a flat panel detector on the same rotary gantry of the FXLT system. The system design, a lab-made C++ based program controller are present. The system calibration and evaluation are also discussed in this chapter.

Chapter 5 discusses the small animal studies performed by the FXLT imaging system. In vivo and three-dimensional mice experiments are reported for the first time in pencil-beam-based XLCT imaging. The experimental set-ups and reconstruction result for both enthused and in vivo mice experiments are discussed in this chapter.

In the end, Chapter 6 concludes the dissertation work and provides a discussion for future works in XLCT and XFCT imaging.

CHAPTER 2

SUPERFAST SCAN OF FOCUSED XLCT IMAGING

2.1 Introduction

X-ray luminescence computed tomography (XLCT) was introduced in the past decade as a hybrid molecular imaging modality with great potentials for small-animal imaging by combining the high-spatial resolution of conventional x-ray imaging with the superb measurement sensitivity of optical imaging. Particularly, the narrow x-ray beam based XLCT has been shown to obtain very high spatial resolution, even at depths of several centimeters with good molecular sensitivity inside of turbid media [75, 76]. Briefly, a focused or collimated beam of x-ray photons is utilized to penetrate deeply through the specimen with minimal scattering. The x-ray excitable contrast agents within the path of the x-ray beam will absorb the x-ray energy and emit optical photons. Some emitted optical photons can propagate to object surface to be measured by sensitive optical detectors such as an electron multiplying charge-coupled device (EMCCD) camera or photomultiplier tube (PMT) for XLCT image reconstruction. The first demonstration of XLCT imaging was reported by Pratx et al. using a selective excitation scanning scheme, much like first generation x-ray CT scanners [77, 78] and then by many other groups [79-81]. Since then, due to many advantages of XLCT compared with other optical methods, several research groups, including our own, have pursued the improvement of XLCT from different aspects [82-86].

We have shown that by using a focused beam of x-rays as the excitation source for performing XLCT, orders of magnitude of better sensitivity can be achieved due to higher flux and efficient use of x-ray photons compared with the collimation-based method. In addition, higher measurement sensitivity can also be obtained by using PMTs as the optical detector compared with the EMCCD cameras [87]. To perform multi-color FXLT imaging, we have synthesized biocompatible nanophosphors with bright and distinct x-ray luminescence spectra and compared them with commercially available nanophosphors [88]. Our studies have demonstrated that the spatial resolution could be improved to be close to the x-ray beam size by reducing the scanning step size to be smaller than the x-ray beam size [89].

While our results with this set-up are promising, the main drawback of this method is the relatively long measurement time due to the small beam size and selective excitation scanning scheme where the beam is moved or stepped along the object at predefined positions and the emitted photon intensity is acquired at each position before moving to the next position. To improve the scan time, in this work we have first introduced a continuous scanning scheme where the x-ray beam will move across the object in a single continuous motion, and at predefined intervals, data will be acquired and saved by a high-speed oscilloscope such as the optical photon emission intensity from the object and the x-ray beam intensity by use of a single-pixel detector set-up used for automatic phantom

boundary detection purposes [90, 91].

Under the continuous scanning scheme, the main factor that limits the scanning speed is the data acquisition time at each interval position. Here, we have reported that the gated photon counter collects and transfers XLCT measurement data much faster than the oscilloscope. The gated photon counter only counts the photon peaks in each measurement time window, while the oscilloscope records the entire waveform including both background noise data and photon peak data. The photon counter records much less data without losing any relevant information, which makes it ideal for fast XLCT imaging [92].

In the photon counter based system with a continuous scanning scheme, the data is only acquired at predefined positions although the x-ray beam moves in a continuous motion. The majority of imaging time is wasted when waiting for the stage to translate the x-ray beam to predefined positions. In order to further improve the scanning speed, we have introduced a fly-scanning scheme where the photon counter constantly collects imaging data and the position information is recorded from the high-resolution encoder of the motorized linear stage at the beginning of each data acquisition time window.

To evaluate these scan schemes, we have performed experiments by scanning the same phantom using four different schemes described above: (1) the oscilloscope based XLCT imaging system with the run-and-shoot scheme; (2) the oscilloscope based XLCT imaging system with a continuous scanning scheme; (3) the photon counter based XLCT imaging system with a continuous scanning scheme; and (4) the photon counter based XLCT imaging system with fly-scanning scheme. Furthermore, for the scan scheme (4), 180 projections of x-ray beam intensity data were acquired by using the single-pixel x-ray detector so that the parallel beam CT image was reconstructed to verify the XLCT images.

The remainder of this chapter is organized as follows: In Section 2.2, we describe the upgraded design of the focused XLCT imaging system, the four scan schemes including the superfast scheme 4, and the experimental set-up. In Section 2.3, we report the results of the imaging experiments. Finally, in Section 2.4, we discuss our findings and conclude the chapter.

2.2 Methods

2.2.1 XLCT experimental system set-up

Fig. 2.1 shows a computer-aided design (CAD) model of the proposed imaging system and Fig. 2.2 shows a photograph of the physical system in our laboratory. This imaging system is an upgraded version of the focused x-ray beam based XLCT imaging system described previously in [87]. Briefly, an x-ray tube with a fixed polycapillary lens (X-Beam Powerflux [Mo anode], XOS) generated x-ray photons with a maximum energy of 50 kVp and a tube current of 1.0 mA. The lens focused the x-ray photons into a superfine x-ray beam with an approximate focal spot diameter of 150 μm at the focal distance of 44.5 mm. The imaged object was placed on a stage that within the focal spot of the x-ray beam and was fixed on top of a rotation stage (RT-3, Newmark Systems Inc.) mounted to a motorized vertical lift stage (VS-50, Newmark Systems Inc.) and linear stage (NLE-100, Newmark Systems Inc.) for rotating and translating the object at required depths and positions. Compared with the previous imaging system in [84], the addition of a motorized vertical lift made it feasible for future 3D scans. The x-ray beam's intensity was monitored with a single scintillator crystal based detector. Emitted optical photons

from the single pixel scintillator were collected by an optical fiber cable (labeled as Fiber 2 in Figs. 2.1 and 2.2) and then delivered to a PMT (H8259-01, Hamamatsu). The signal from the PMT was collected by a gated photon counter (SR400, Stanford Research Systems) via IEEE-488 cable [93] in the photon counter based XLCT imaging system. Monitoring of the beam intensity was used to tell the object boundary and replaced the slow flat-panel x-ray detector used in the old system. During the XLCT scans, emitted optical photons from the imaged object propagated to the surface and then were collected by a single optical fiber cable (labeled Fiber 1) to be delivered to a fan-cooled PMT (H7422-50). The signal from the PMT was then amplified using a broadband amplifier (SR455A, Stanford Research Systems) with a gain of 125 and then filtered with a low-pass filter (BLP-10.7+, fc = 11 MHz, Mini-Circuits) to reduce high-frequency noise before finally collected by a channel of the high-speed oscilloscope or a gated photon counter. The entire imaging system up to the PMTs were placed inside of a light-tight and radiation shielding cabinet and was controlled with a lab computer [91].

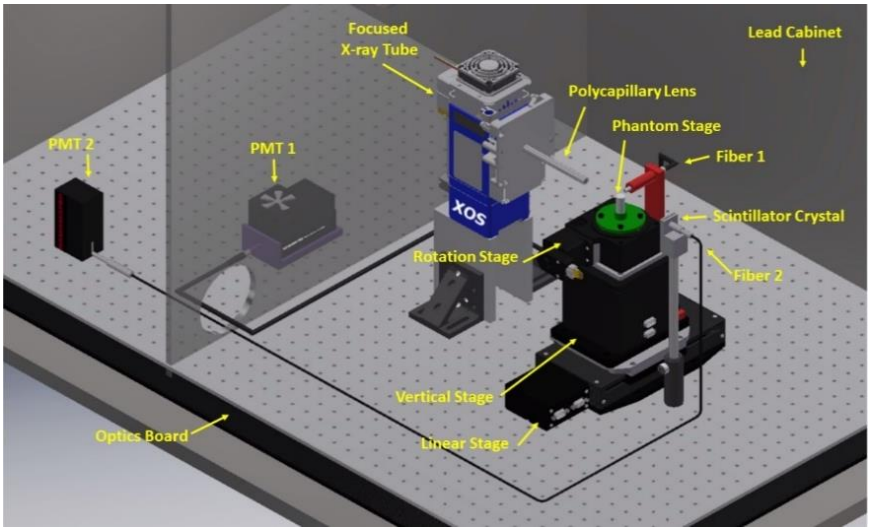

Figure 2.1. Computer-Aided Design (CAD) model of the focused x-ray beam based XLCT imaging system.

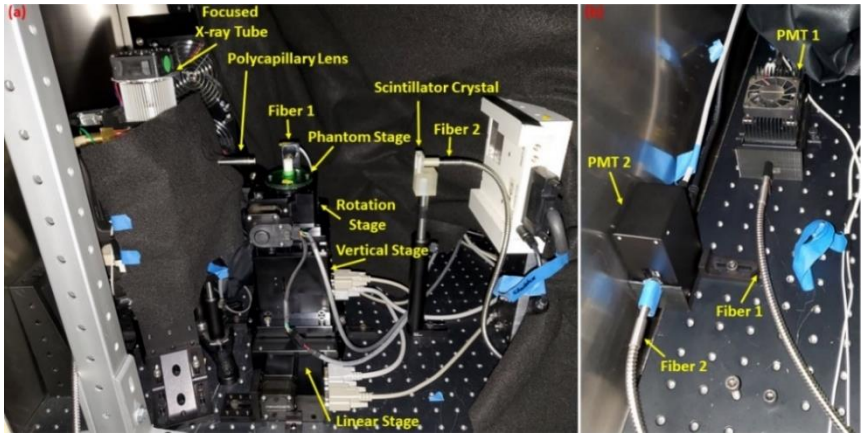

Figure 2.2. Photograph of the imaging system.

2.2.2 High scanning speed methods

2.2.2.1 Improvement in DAQ device

One main factor that limits the scanning speed is the data acquisition time of signals from PMTs at each position. To increase the scanning speed, we replaced the high-speed oscilloscope with the dual channel gated photon counter to collect the pulse signals from the PMT via an IEEE-488 cable. This photon counter was programmed with the NI-488M functions using Microsoft Visual Studios IDE in C++ [92]. We have reported that the gated photon counter collects and transfers XLCT measurement data much faster than the oscilloscope [91]. Because the gated photon counter only counts the pulse peaks in each measurement interval, while the oscilloscope records the entire waveform including both background noise data. The photon counter based schemes collects much less data without losing any relevant information, which makes the total scan time much shorter compared with the oscilloscope based schemes.

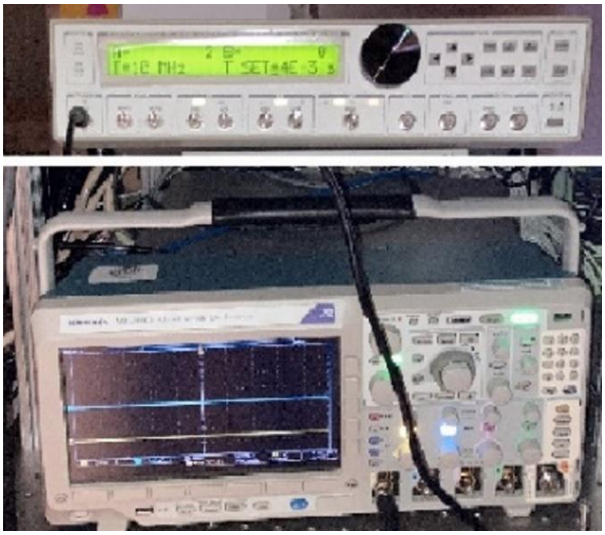

Figure 2.3. DAQ devices: Gated photon counter (top) and high-speed oscilloscope (bottom).

2.2.2.2 Four scan schemes

The scan scheme 1 as shown in Fig. 2.4(a), run-and-shoot, was used in the last generation of XLCT systems. To compare it with other schemes, we have re-installed all the components and took measurements. With the scan scheme 1, the linear stage stops and waits for the oscilloscope to collect data at every measurement interval, which is very time consuming.

Recently, we applied scan schemes 2 and 3, as shown in Fig. 2.4(b), in the existing XLCT imaging system. We implemented a continuous scanning mode to significantly reduce the total scan time. For each angular projection, a single continuous movement of the linear stage was applied. For example, for a 15 mm diameter phantom, the linear stage moved continuously for 15 mm in one motion. We selected the data acquisition position and collection time window for each liner scan. The encoder of the motorized linear stage was monitored continuously to select the right data collection time. We used the oscilloscope as the DAQ device for scan scheme 2 and the photon counter for scan scheme 3. We developed a macro program with Microsoft Visual Studios IDE in C++ to

control and automate the XLCT scan for both schemes. For each XLCT scan, we need to input the total scanning distance (determined by the object size), the interval spacing for data acquisition for each linear scan, the linear translation speed which depends on parameters such as the interval spacing (finer spacing requires slower translation to save the data), the exposure time of the DAQ device at each acquisition, the number of angular projections for each transverse section (in degrees), the number of slices or transverse sections, and the distance between slices. However, we found that the majority of imaging time was wasted while waiting for the movement of the linear stage.

To further improve the scan speed and to reduce the input numbers of each scan, we introduced the scan scheme 4, the flying scan, in which the photon counter constantly collected the pulse signals in a short data collection window (10 ms) and the position information was recorded for each measurement data at the beginning of time window as shown in Fig. 2.4 (c). When the position information indicated the end of a linear scan, the program rotated the object to the next projection and started the next linear scan. The program collected as much data as possible after we set the total scanning distance and linear translation speed. The data collection window length of the DAQ device, the number of angular projections for each transverse section, the number of slices or transverse sections, and the spacing between slices could be adjusted for each XLCT imaging.

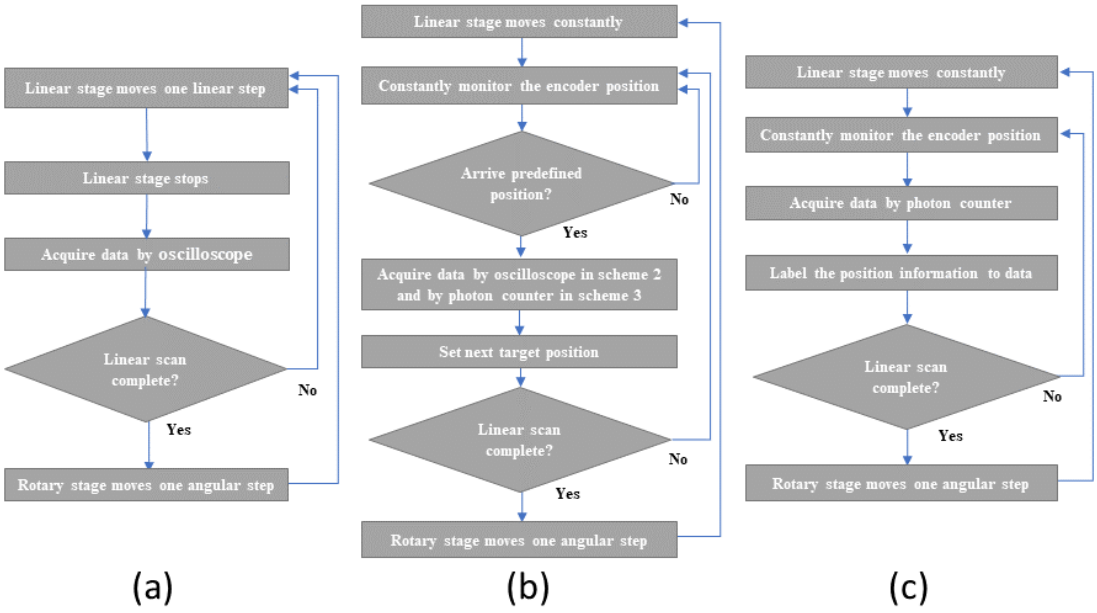

Figure 2.4. Schematic of four schemes: (a) oscilloscope based XLCT imaging system with the run-and-shoot scheme, (b) oscilloscope based XLCT imaging system and photon counter based XLCT imaging system with a continuous scanning scheme, and (c) photon counter based XLCT imaging system with fly-scanning scheme.

2.2.3 Phantom experimental set-up

2.2.3.1 Geometry and fabrication of phantom

Fig. 2.5 shows the schematic of the designed phantom. A cylindrical phantom composed of 1% intralipid, 2% agar, and water with a diameter of 12 mm and height of

20 mm were made at our lab. Two glass capillary tube targets (outer diameter: 0.8 mm; inner diameter: 0.4 mm, Drummond Scientific) and another two glass capillary tube targets (outer diameter: 1.0 mm; inner diameter: 0.58 mm, standard glass capillaries, WPI) were filled with a solution of $Gd2O2S:Eu^{3+}$ (GOS:Eu) (UKL63/UF-R1, Phosphor Techn. Ltd.) at a concentration of 10 mg/mL. The four targets were embedded vertically side-by-side in the background phantom.

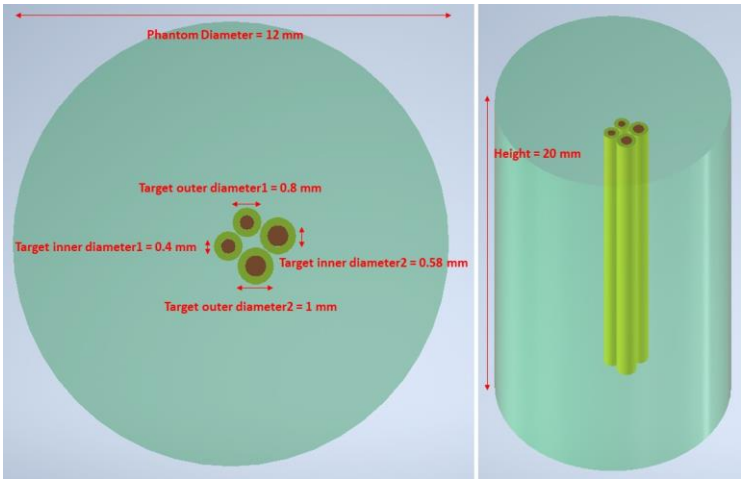

Figure 2.5. Phantom design: four targets of two different sizes.

2.2.3.2 Scan phantom by 4 different schemes

The phantom was first placed into the oscilloscope based XLCT imaging system and scanned with the run-and-shoot scheme (scheme 1). During the scan, the x-ray tube was operated at 30 kVp and 0.5 mA. The measurements were acquired from 6 angular projections (30º/projection). For each angular projection, the linear stage moved in 150 run-and-shoot motions (0.1mm/motion) and scanned a total distance of 15 mm to make sure that the phantom of 12 mm diameter was scanned completely. The oscilloscope used two channels to acquire all the photon peaks (data length of 100k points) in a period of 10 ms from both PMTs for each acquisition (150 acquisitions per projection). One channel of the PMT signal recorded the information of the x-ray beam intensity and was used to detect the boundary of the phantom.

After the stages were reset to their original positions, the phantom was then scanned by the continuous scanning scheme with the oscilloscope as detector (scheme 2). The parameters of the x-ray tube, the rotary and vertical stages, and the settings of the oscilloscope were the same as those in scheme 1. For each projection, the linear stage scanned in a continuous motion for 15 mm in which the measurement data were acquired every 0.1 mm (150 acquisitions per projection).

Then, we reset all stages and the phantom was scanned by the continuous scanning scheme with the photon counter as detector (scheme 3). The parameter of the x-ray tube, the rotary and vertical stages were the same as those in scheme 2 as described above. For each data acquisition, the photon counter acquired the photon pulses in a measurement time of 10 ms (150 acquisitions per projection).

At last, the phantom was scanned by the fly-scanning scheme with the photon counter as detector (scheme 4). The parameters of the x-ray tube, the rotary and vertical stages,

and the settings of the photon counter were the same as those in scheme 3. For each projection, the linear stage scanned in a continuous motion for 15 mm in which the measurement data and the encoder position information were continuously acquired during the entire linear scan. In this experiment, the photon counter collected 335-350 acquisitions per projection. Based on the position information, we select 300 acquisitions of data for imaging reconstruction.

2.2.3.3 Scan phantom by parallel beam CT and cone beam CT

After the XLCT scans by 4 schemes, the phantom was then scanned again for 180 projections using the scheme 4 to perform XLCT imaging and parallel beam CT imaging simultaneously. The parallel beam CT images were reconstructed from the x-ray beam intensity measured by the single pixel scintillator detector. Those images could provide the ground-truth images of the background phantom and the capillary tubes in the XLCT images. The parameter of the x-ray tube, the linear and rotary movements of the stages were the same as those in scheme 4 except the 180 angular projections. With the superfast scanning scheme, 180 angular projections (1^{o}/projection) of measurements were able to be acquired within 17 minutes.

In the end, the phantom was placed inside of the lab-made microCT scanner to perform a cone beam microCT scan for cross validation [94]. For the microCT scan, a cone beam x-ray tube (XTF5011, Oxford Instruments) was operated at 50 kVp and 0.4 mA and an x-ray detector (Shad-o-Box 1KHS, Teledyne DALSA) was operated at an exposure time of 456 ms. We acquired data of 360 projections with the angular step size of 1 degree.

2.2.2.4 Reconstruction algorithms

The cone beam microCT images and the parallel beam CT images were reconstructed in MATLAB using a filtered back-projection (FBP) algorithm with a Shepp-Logan filter. For XLCT imaging, the reconstruction is similar to fluorescence molecular tomography (FMT) [95], in which images were reconstructed using an optical photon propagation model (radiative transport equation) inside turbid media which also included information such as the x-ray beam's size and location as anatomical priors. We used the L1 regularized majorization-minimization (MM) algorithm. Details of the algorithm are described in [95-99].

For the XLCT experiment with 180 angular projections of measurements using the scan scheme 4, we selected four sets of data with different angular projections to study the effects of angular projection number on the FBP reconstruction of parallel beam CT and XLCT images. These angular projection numbers (and the step size) are 6 projections (30^{o}/projection), 20 projections (9^{o}/projection), 60 projections (3^{o}/projection), and 180 projections (1^{o}/projection), respectively.

2.3 Result

2.3.1 Cone beam CT and parallel beam CT images

Fig. 2.6 shows the reconstructed cone beam CT image (left) and parallel beam CT image (right) at the transverse section of the XLCT scan. We can see both CT images have plotted the targets and the background phantom very well. While both CT images can be used as the cross validation of the target position, the parallel beam CT is a better choice because the parallel beam CT images were scanned simultaneously with the XLCT imaging. With the parallel beam CT image, the center of the phantom and the distance of the phantom center to each target center were calculated as the true distances to evaluate the XLCT image quantitatively in the next sections. While the cone beam CT image is slightly out of the field of view, the reconstructed image is sufficient for the cross validation.

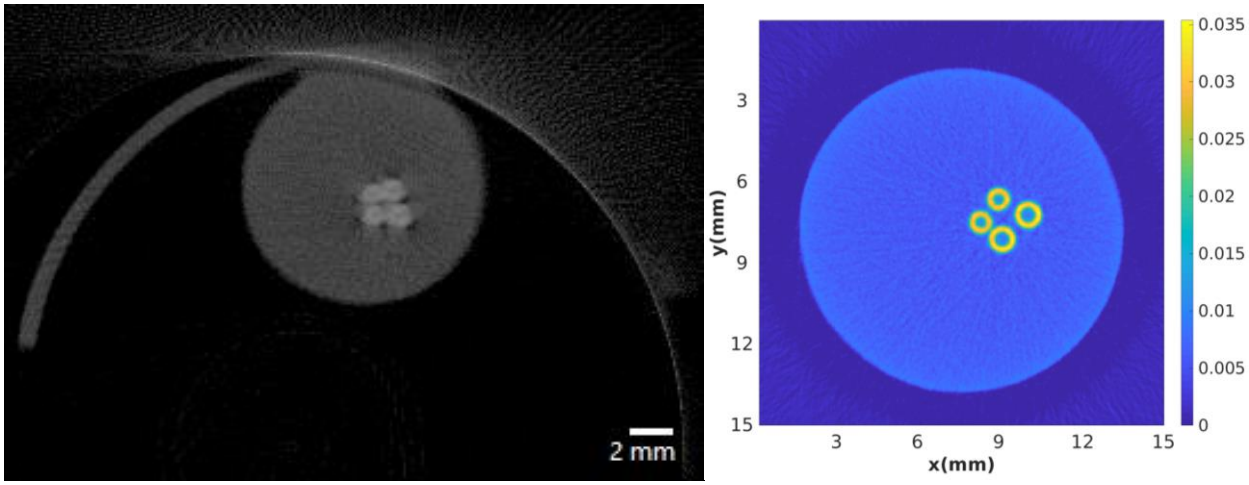

Figure 2.6: Reconstructed CT images of the phantom: the cone beam CT (left); the parallel beam CT (right).

2.3.2 Reconstructed XLCT images with 4 different scan schemes

XLCT reconstruction is a model-based (optical photon propagation model) algorithm, in which the geometry of the background phantom or object are required to generate the system [96-99]. In the above four XLCT scan schemes, we scanned a total distance of 15 mm to make sure the whole 12 mm-phantom was scanned completely in each projection. To sense the edge of the phantom, we used a single pixel scintillator crystal coupled to a PMT as the x-ray intensity detector. From the changed intensity, we could calculate the phantom boundary as shown in Fig. 2.7. The horizontal axis in each figure represents projection number and the vertical axis represents linear position. We see that the boundary position of the phantom changed a little bit in different projections, which indicates that the phantom is not placed at the perfect rotary center.

For the XLCT reconstructions, the sensitivity matrix defined in the finite element mesh of the scanned section was interpolated onto a fine 2D grid with pixel size of 25 μm2 [89]. The details of the reconstruction algorithm were reported in [95]. The reconstructed XLCT images for the four different scan schemes at the same scanning depth are plotted in Fig. 2.8 and the zoomed-target regions are plotted in Fig. 2.9, where the green circles represent the ground truth obtained from the parallel beam CT images. For all four schemes, we can see that the four targets have been successfully resolved and are reconstructed at the right locations. To quantitatively evaluate the reconstructions, the

DICE coefficients (using full width 10% maximum) were calculated. For the scan scheme from 1 to 4, the DICE coefficients were calculated to be 82.0%, 80.4%, 81.1%, and 83.2%, respectively. Based on these metrics, there is no noticeable difference in terms of the DICE coefficients among the four scan schemes, while the scan scheme 4 resulted in slightly better results, which is reasonable because more measurement data were collected for the scan scheme 4.

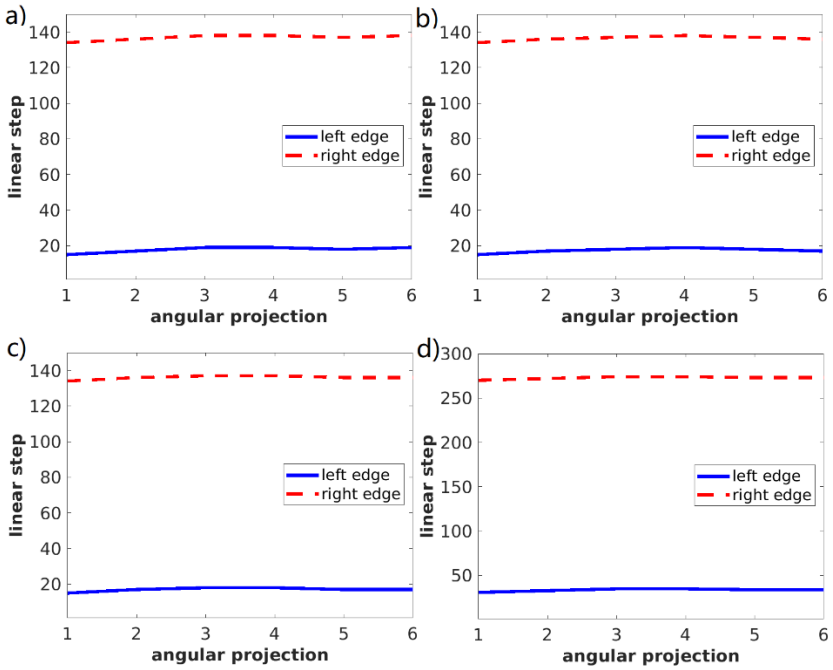

Figure 2.7. Boundary detection results for the four different scan schemes: (a) for 1, (b) for 2, (c) for 3, and (d) for 4.

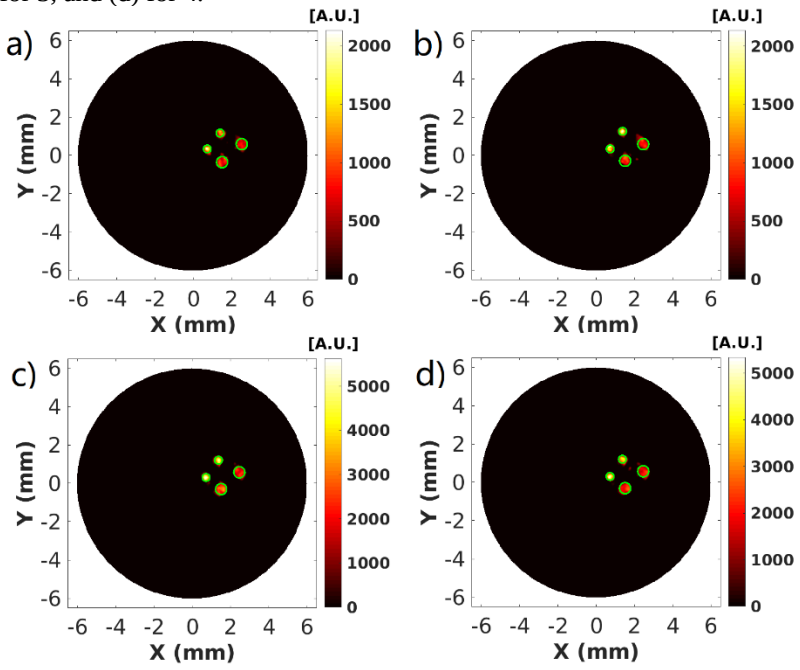

Figure 2.8. Reconstructed XLCT images for the four different scan schemes: (a) for 1, (b) for 2, (c) for 3, and (d) for 4.

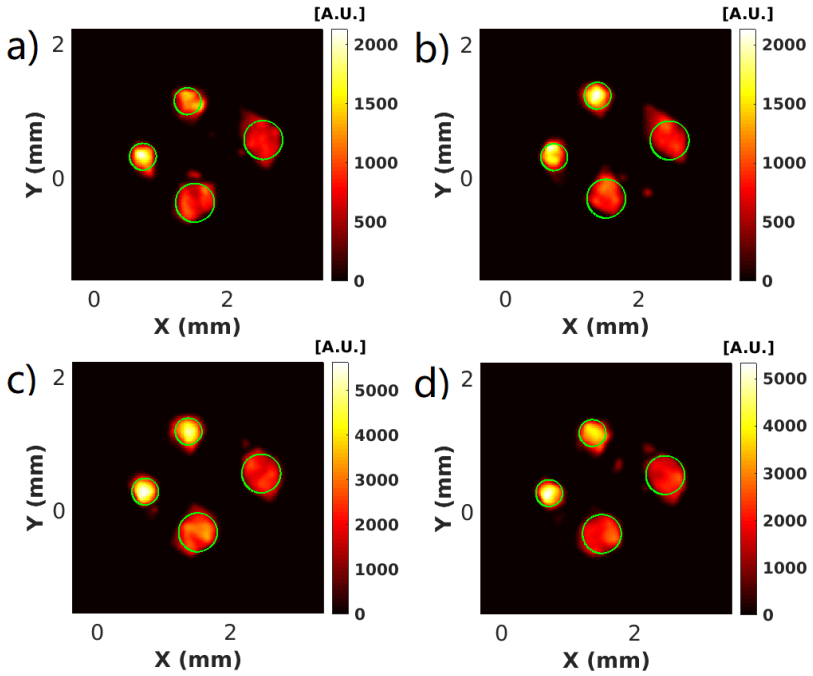

Figure 2.9. Zoomed-in reconstructed XLCT images from Fig. 2.8 for the four different scan schemes: (a) for 1, (b) for 2, (c) for 3, and (d) for 4.

2.3.3 Comparison of XLCT scan time

To compare the scan time of four different scan schemes, we list their data acquisition window of each measurement data, linear scan speed, data number, total scan time for one linear scan (15 mm), and the total scan time for one transverse section in Tab. 2.1. The total scan times are 1232, 513, 70, and 43 seconds for scan schemes 1 to 4, respectively. While both scan scheme 2 and 3 utilized the same continuous scan mode, the oscilloscope based scheme 2 took much longer time because the slow data collection speed so that the linear scan speed was slower. We can see that the photon counter based scan scheme 4 is 28.6 times faster than the reported scan scheme 1. In fact, with the scan scheme 4, we are able to perform a parallel beam CT scan with180 angular projections in 974 seconds.

Scan scheme	Data acquisition window (and transfer time)	Linear scan speed	Data number	Total time for 1 projection (15 mm)	Total time for 1 transverse section (6 projections)
1	420 to 460 ms	Run-and-shoot mode	150	190.8 seconds	1232 seconds
2	420 to 460 ms	0.18 mm/s	150	83.6 seconds	513 seconds
3	20 to 25 ms	1.6 mm/s	150	9.6 seconds	70 seconds
4	20 to 25 ms	3 mm/s	335 to 350	5.3 seconds	43 seconds

Table 2.1. Data acquisition window, linear scan translation speed, number of measurement data, and total time.

2.3.4 Effects of angular projection number

The parallel beam CT images were reconstructed with FBP from the measurements of the single pixel x-ray detector. The CT images are plotted in Figs. 10(a), 10(b), 10(c), 10(d) for angular projections of 6, 20, 60, and 180, respectively. The targets (the capillary

tubes) were reconstructed very well in Figs. 10(b) to 10(d). The x-ray luminescent targets (the particles) could not be detected in the parallel CT images due to their low concentrations, which is the reason why we are developing the XLCT imaging.

The parallel beam XLCT measurements were taken simultaneously and the XLCT images (as shown in Fig. 2.11) were constructed with FBP too. The reconstructed XLCT images are plotted in Figs. 11(a), 11(b), 11(c), 11(d) for angular projections of 6, 20, 60, and 180, respectively. The XLCT targets are barely seen in Fig. 2.11(a), which indicates that 6 projections are not sufficient for FBP based XLCT imaging, while Fig. 2.8(d) indicates that the MM algorithm is able to reconstruct XLCT targets with 6 angular projections. The targets can be observed clearly in Fig. 2.11(b), while there are some artifacts, which tells us that the FBP based XLCT imaging needs angular projection up to 20. We cannot see the capillary tubes in Fig. 2.11, which means that the capillary tube does not emit optical photons or their luminescence can be ignored. We have overlaid Fig. 2.10(d) with Fig. 2.11(d) in Fig. 2.11(e), in which the CT targets (the green circles) are overlaid very well with the XLCT targets (the red dots). It is encouraging because the parallel CT images could tell the locations of the reconstructed XLCT targets in future studies.

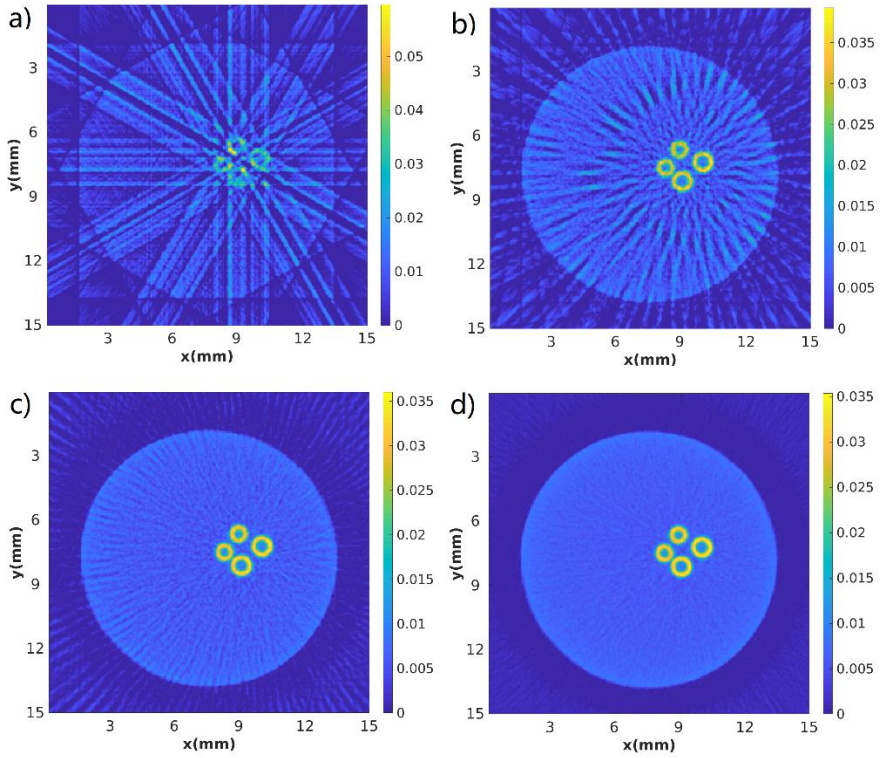

Figure 2.10. Reconstructed parallel beam CT images with FBP for different angular projection numbers: (a) 6 projections (30º/projection), (b) 20 projections (9º/projection), (c) 60 projections (3º/projection), and (d) 180 projections (1º/projection).

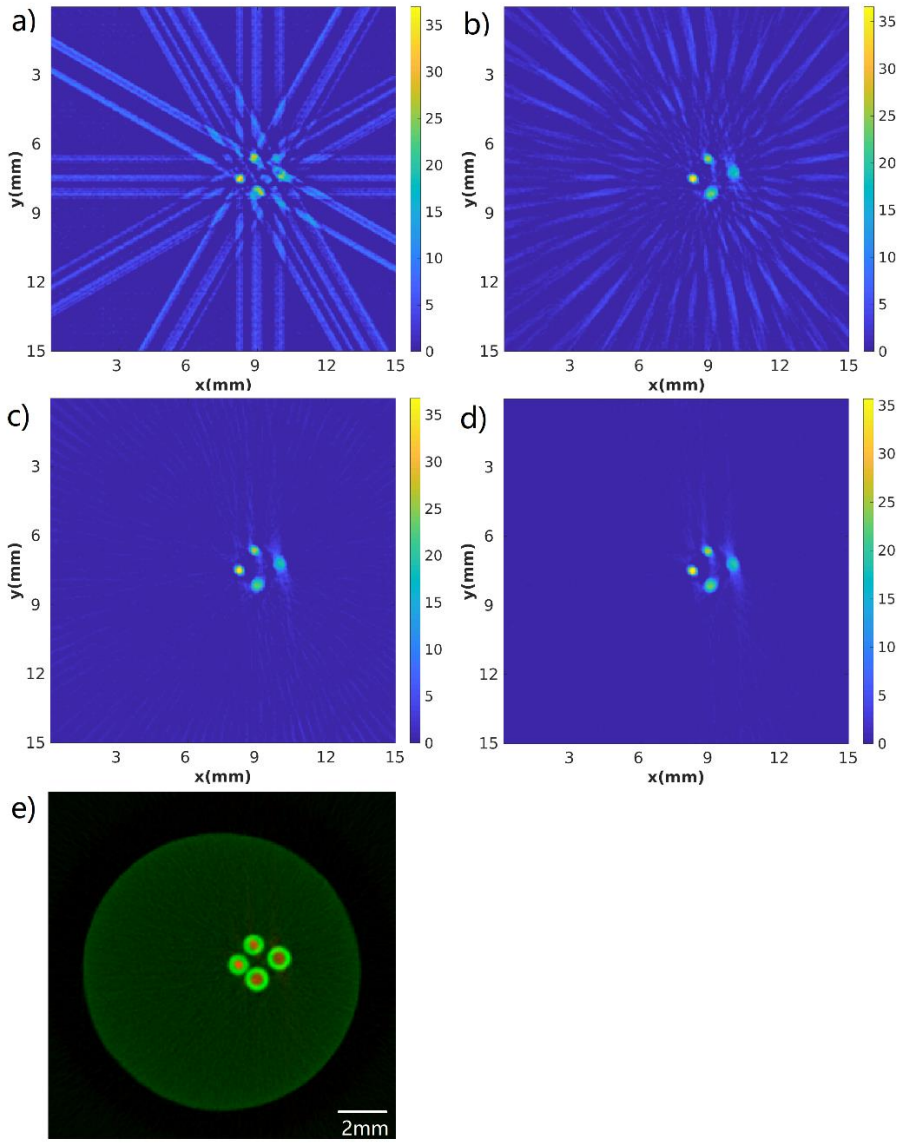

Figure 2.11. Reconstructed XLCT images with FBP for different angular projection numbers: (a) 6 projections (30º/projection), (b) 20 projections (9º/projection), (c) 60 projections (3º/projection), and (d) 180 projections (1º/projection). (e) The overlaid figure of (d) with Fig. 2.10(d).

2.4 Discussions and conclusions

In this work, we have introduced three new scan schemes (schemes 2 to 4) including the superfast scan scheme, the scheme 4 of the focused XLCT Imaging. By comparing the scan times and the image quality among all four scan schemes, we can see that the scan speed is improved by 28.6 times compared with the previously reported run-and-shoot scheme. With the superfast scan scheme, we were able to take measurements for each transverse section (with 6 angular projections and scanning distance of 15 mm per projection) in 43 seconds (31.4s scan time and 11.6s rotary time) including all stage movements. Furthermore, we collected more measurement data and achieved better DICE coefficients for multiple targets XLCT experiments as shown in Fig. 2.8 and Fig. 2.9. Moreover, we used a scintillator crystal coupled to a PMT to act as a single-pixel detector to replace the flat-panel x-ray detector. This improvement decreased the size and the price of the imaging system. This also made the fast and automatic phantom boundary detection feasible, which allowed us to perform the parallel beam CT imaging simultaneously with the XLCT imaging. As shown in Fig. 2.10 and Fig. 2.11, we compared the reconstructed XLCT images and the parallel beam CT images with different angular projection numbers and demonstrated that sufficient angular projections number (up to 20) is needed for the FBP reconstruction with the acceptable image quality. The total scan time of 180 projections was 974 seconds, which indicates the XLCT imaging system with the proposed superfast scheme has capabilities to perform three dimensional XLCT imaging in a reasonable time. We also demonstrated the performance of the L1 regularized MM algorithm is significantly better than the FBP algorithm when there are not enough projections (as small as 6) of measurements.

Multi-pinhole collimated XLCT has reduced the translational scanning time [100]. However, the collimated x-ray beam has less intensity and relatively undesired larger beam size compared with the focused x-ray beam. If we could utilize multiple focused superfine x-ray beams, the scanning time could be improved further.

The MM reconstruction has the advantage of less angular projections and shorter scan time for the pencil beam based XLCT imaging. However, the MM reconstruction is a model based algorithm, in which we usually calculate the photon propagation with the diffusion equation that is solved with a finite element method. A finite element mesh is needed for the finite element method, which is tedious. The FBP reconstruction algorithm is very straightforward to apply, while it needs at least 20 angular projections and might need up to 60 angular projections for better quality. This is why we would like to improve the scanning speed so that we can use FBP in XLCT with a reasonable scanning time. The shorter scanning time makes it possible for us to scan multiple transverse sections of irregular shaped mice to obtain the 3D XLCT images straightforwardly.

In summary, the introduced superfast scan scheme im- proved the XLCT times by 28.6 times and achieved a scan time of 43 seconds per transverse section with slightly better XLCT image quality. The single pixel x-ray detector allowed us to perform parallel beam CT imaging simultaneously with the XLCT imaging.

In future studies, we will use the proposed scan scheme to perform quantitative studies of superfine and in vivo 3D XLCT imaging. We will also scan the image object over 360 degrees instead of 180 degrees to collect the emitted photons from all directions for better sensitivity. And we will also use machine learning algorithms for better XLCT reconstruction and will apply the bright nanoparticle to save the measurement time [101-105].

Acknowledgements: I would like to thank Yibing Zhang who made the ager phantom used in the experiments and assisted me to build the XLCT imaging system. I also would like to thank Dr. Michael C. Lun who built the conventional oscilloscope based XLCT imaging system and taught me to perform the XLCT experiments at early stages. I have developed the three new scanning schemes, designed, and built the upgraded XLCT imaging system, developed a C++ based program controller, operated the phantom experiments, and performed the data analysis and image reconstruction in this work.

CHAPTER 3

QUANTITATIVE AND THREE-DIMENSIONAL IMAGING OF X-RAY LUMINESCENCE COMPUTED TOMOGRAPHY

3.1 Introduction

X-ray luminescence computed tomography (XLCT) was introduced in the past decade as a hybrid molecular imaging modality with great potentials for small-animal imaging by combining the high-spatial resolution of conventional x-ray imaging with the superb measurement sensitivity of optical imaging. Particularly, the narrow x-ray beam based XLCT has been shown to obtain very high spatial resolution, even at depths of several centimeters with good molecular sensitivity inside of turbid media [75], [76]. Briefly, a focused or collimated beam of x-ray photons is utilized to penetrate deeply through the object with minimal scatter. The x-ray excitable contrast agents within the path of the x-ray beam emit optical photons when excited by x-ray photons. Some emitted optical photons can propagate to object surface to be measured by sensitive optical detectors such as an electron multiplying charge-coupled device (EMCCD) camera or photomultiplier tube (PMT) for XLCT image reconstruction. The first demonstration of XLCT imaging was reported by Pratx et al. using a selective excitation scanning scheme, much like first generation x-ray CT scanners, and demonstrated the potentials of this imaging method [77], [78]. We have shown that by using a focused beam of x-rays as the excitation source for performing XLCT, orders of magnitude of better sensitivity can be achieved due to higher flux and efficient use of x-ray photons compared with the collimation-based method. In addition, higher measurement sensitivity can also be obtained by using PMTs as the optical detector compared with the EMCCD cameras [76], [87]. To perform multi-color XLCT imaging, we have synthesized biocompatible nanophosphors with bright and distinct x-ray luminescence spectra and compared them with commercially available nanophosphors [88]. Furthermore, we have shown that the scan time could be improved by introducing a fly-scanning scheme and a dual channel gated photon counter as data acquisition device [69], [72], [106]. However, so far there is no quantitative study of pencil beam XLCT in imaging x-ray excitable nanophosphor targets in deep scattering media.

Here, we have, for the first time, analyzed quantitatively the reconstructed phosphor concentrations of deep targets through phantom experiments. We have scanned a cylindrical agar phantom containing twelve targets filled with three different phosphor concentrations (2.5 mg/ml, 5 mg/ml, and 10 mg/ml) using an upgraded XLCT imaging system in our laboratory and evaluated the performance of filtered back-projection (FBP) algorithm using setups of one, two, and four detectors. Then we have scanned phantoms with 3D printed targets and obtain 3D functional images and 3D structural images simultaneously.

3.2 Methods

3.2.1 XLCT experimental system set-up

Fig. 3.1 shows the schematic (top) and the photograph (bottom) of the XLCT imaging system. This imaging system is an upgraded version of the focused x-ray beam based XLCT imaging system previously described in [69]. Briefly, an x-ray tube with a fixed polycapillary lens (X-Beam Powerflux [Mo anode], XOS) generates x-rays with a maximum energy of 50 kVp and tube current of 1.0 mA and are focused to an approximate focal spot size of 150 μm (focal distance: 44.5 mm). The imaged object is placed on a stage that within the focal spot of the x-ray beam and is fixed on top of a rotation stage (RT-3, Newmark Systems Inc.) mounted to a motorized vertical lift stage (VS-50, Newmark Systems Inc.) and linear stage (NLE-100, Newmark Systems Inc.) for rotating and translating the object at various depths. Compared with our previous imaging system in [69], we used four optical fiber cables coupled with fan-cooled PMTs (H7422-50) to collect the x-ray induced photons for improving the measurement sensitivity. We also used a single scintillator crystal coupled with a PMT (H8259-01, Hamamatsu) to monitor the pencil x-ray beam's intensity to sense phantom boundary and to preform parallel beam based CT imaging simultaneously, which can be used to verify the true locations of the XLCT targets. The signal from the PMTs was then amplified using a broadband amplifier (SR455A, Stanford Research Systems) with a gain of 125 and then filtered with a low-pass filter (BLP-10.7+, fc = 11 MHz, Mini-Circuits) to reduce high-frequency noise. This signal was collected by the dual channel gated photon counters via IEEE-488 cables. The entire imaging system up to the PMTs were placed inside of a light-tight and radiation shielding cabinet and controlled with a lab computer.

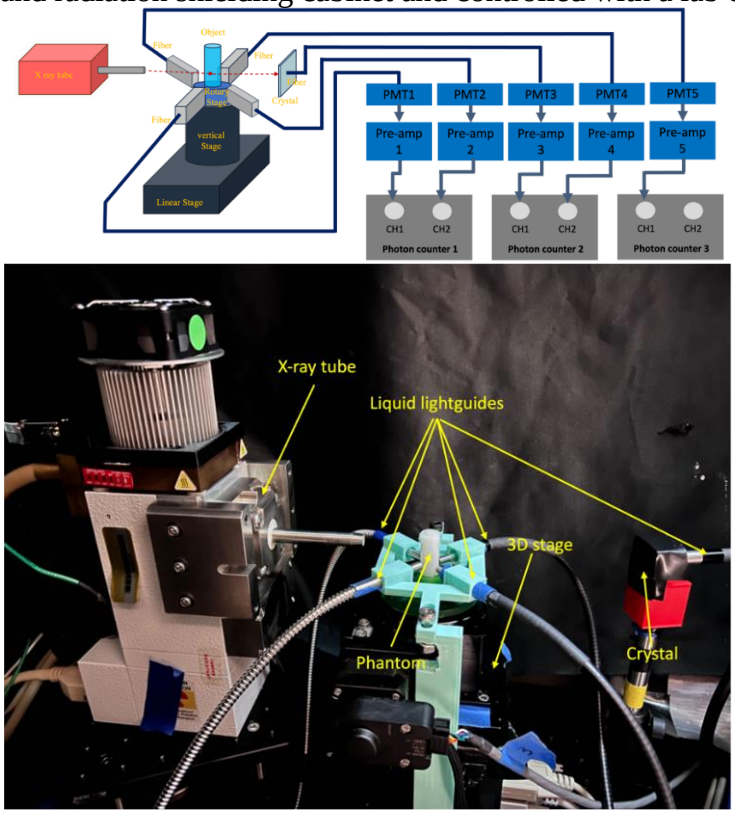

Figure 3.1. Schematic (top) and photograph (bottom) of the multiple channel XLCT imaging

system.

3.2.2 Phantom experimental set-up

Nine phantoms were manufactured in our lab to be scanned by the XLCT imaging system. Eight cylindrical phantoms were composed of 1% intralipid, 2% agar, and water with a diameter of 12 mm and height of 20 mm. To perform quantitative study of pencil beam XLCT imaging, twelve glass capillary tube targets (Drummond Scientific) were equally divided into three groups and filled with $Gd_2O_2S:Eu^{3+}$ (UKL63/UF-R1, Phosphor Techn. Ltd.) solutions at different concentrations. (2.5, 5, and 10 mg/mL) in the first phantom. Each concentration group has 4 targets. The capillary tube targets have an inner diameter of 0.4 mm and an outer diameter of 0.8 mm. The three groups of targets were embedded vertically in the phantom as shown in Fig. 3.2 (a). To perform spatial resolution study of pencil beam XLCT imaging, three glass capillary tube targets (0.15mm of inner diameter, 0.3 mm of outer diameter) were filled with the same solution at concentration of 10mg/mL and embedded side-by-side in the second phantom as shown in Fig. 3.2 (b). And in Fig. 3.2 (c), there were ten targets filled with $Gd_2O_2S:Eu^{3+}$ solution at a concentration of 10 mg/mL that were inserted vertically in third phantom to demonstrate that the scanner is able to image non-sparse targets as well. In the fourth phantom, twelve glass capillary tube targets filled with the same solution at concentration of 10mg/mL were equally divided into three groups at different size (outer diameter: 1 mm, 0.8mm, and 0.4mm; inner diameter: 0.58 mm, 0.4mm, and 0.2mm). Each size group has 4 targets. A “M” shaped target was 3D-printed using clear resin blended with 10 mg/mL of $Gd_2O_2S:Eu^{3+}$ powder through a 3D printer (ANYCUBIC Photon Mono X) and placed in the fifth phantom as shown in Fig. 3.2 (d). A cube grid target and a triangular slot bar target were 3D-printed using the same method and placed in the sixth and the seventh phantom, respectively. The diagram of the 3D-printed targets are shown in Fig. 3.3. Eight glass capillary tube targets (outer diameter: 0.8mm; inner diameter: 0.4mm) filled with $Gd_2O_2S:Eu^{3+}$ solution at a concentration of 10 mg/mL were embedded in the eighth target. The nineth ager phantom was a concaved phantom composed of the same materials, but has a diameter of 20 mm and height of 20 mm.

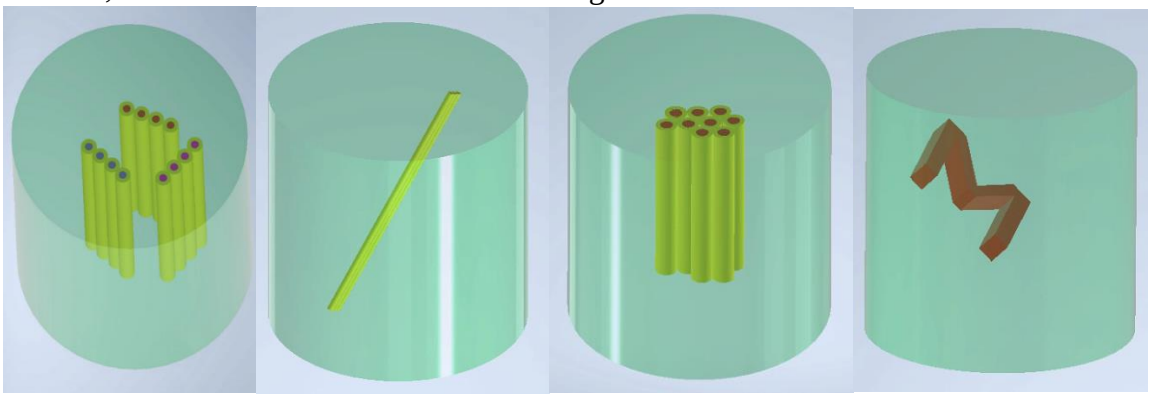

Figure 3.2. Phantom design with: (a) twelve capillary tube targets, (b) three capillary tube targets, (c) ten capillary tube targets, and (d) 3D printed “M” shaped target.

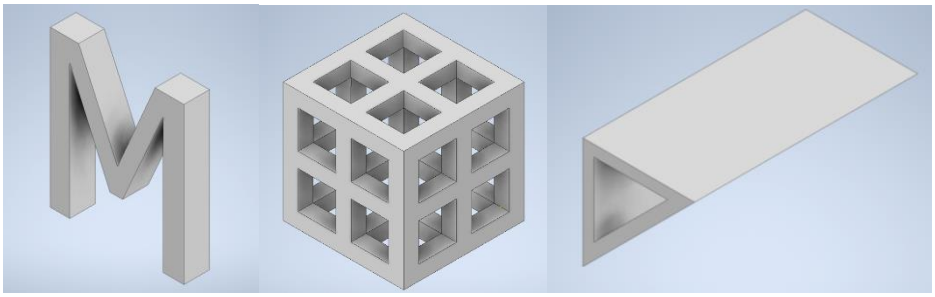

Figure 3.3. 3D-printed targets design: (a) “M” shaped target, (b) cube grid target, and (c) triangular slot bar target.

The nine phantoms were scanned by the XLCT imaging system. The x-ray tube was operated at a setting of 30 kVp and 0.5 mA. From the first phantom to the fourth phantom, the measurements were acquired from one transverse section and 360 angular projections (1^o/projection). For each projection, a fly-scanning scheme was used to translate the linear stage in one continuous motion for 15 mm to make sure the phantom of 12 mm diameter was scanned completely. Under the fly-scanning scheme, the three photon counters constantly collected the pulse signals from each of the five PMTs in a short data collection window (10 ms) and the position information was recorded constantly, which dramatically reduced the linear scanning time. Details of the fly-scanning scheme are described in [72]. For the nineth phantom, the linear stage translated a distance of 24mm for each angular projection and all the other scanning parameters were the same. From the fifth phantom to the eighth phantoms, the measurements were acquired from multiple transverse sections and 90 angular projections (4^o/projection) per section to obtain 3D images. The fifth, sixth, and seventh, and eighth phantom were scanning for 15 slices,18 slices and 6 slices, respectively, with a vertical step size of 0.5 mm/slice.

3.2.3 Imaging reconstruction and evaluation

The phantom region (diameter of 12mm) was selected from the FOV (diameter of 15mm) of the XLCT sinograms and the parallel beam based CT sinograms in MATLAB using a lab-made boundary detection program based on the information of the x-ray beam intensity measured by the scintillator crystal. The parallel beam based CT images were reconstructed in MATLAB using an FBP algorithm with the Hamming filter to provide ground truth of the target locations. For the XLCT imagines, we selected three sets of data with three different numbers of detectors, respectively, to perform FBP reconstruction for investigating the detector number’s effect on the quantitative accuracy of XLCT images. In the one channel setup, the images were reconstructed using the data from one of the four detectors. For the reconstruction of the two channels system, the angle between two fibers is 180 degrees (opposite to each other). For the four channels setup, all the four detectors were employed and the angle between each fiber was 90 degrees.

To perform quantitative study on the reconstructed nanophosphor target concentrations, we have calculated the integration of the reconstruction signals over the location of each target for all the three reconstructions. We also have calculated DICE similarity coefficients to evaluate the similarity between the reconstructed targets and the ground truth.

3.3 Results

3.3.1 Quantitative and two dimensional phantom experiments

For the first phantom, Fig. 3.4 shows the phantom boundary computed by a lab-made boundary detection program using the x-ray beam intensities measured by the scintillator crystal. The plot indicates the edge of the phantom in each angular projection. From this plot, we calculate the phantom boundary from the sinogram of both the XLCT scan and the parallel beam based CT scan. Fig. 3.5 plots the original sinogram of the parallel beam CT scan and the processed sinogram calibrated with the boundary information.

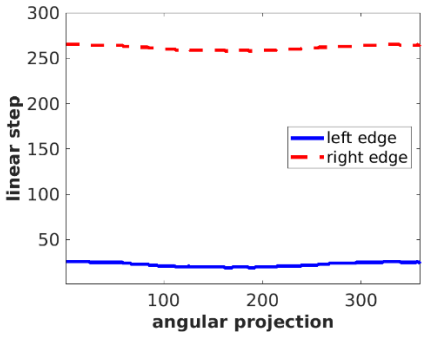

Figure 3.4. Boundary detection results based on the information of the x-ray beam intensity.

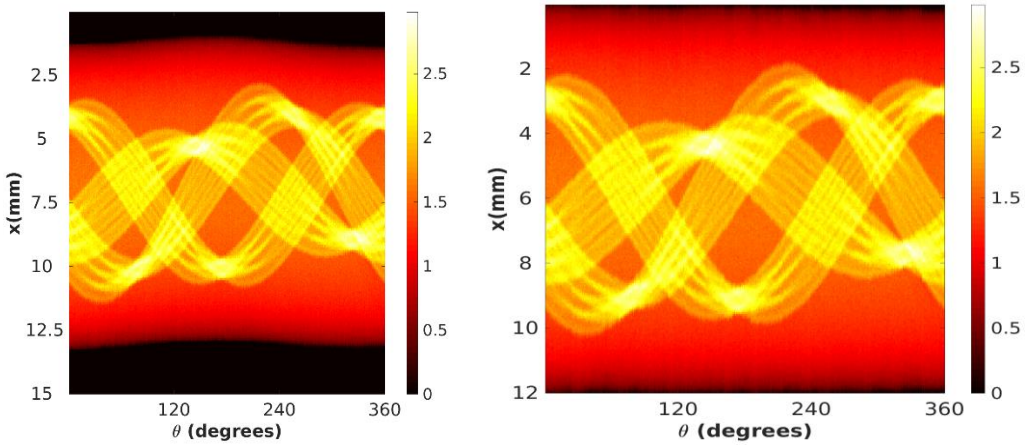

Figure 3.5. Original (left) and calibrated (right) sinograms of the parallel beam CT scan.

From the calibrated parallel beam CT sinogram, we reconstructed the CT image with the FBP algorithm as shown in Fig. 3.6. We can see the pencil beam based CT image has great spatial resolution and can tell the true locations of the glass capillary tubes which were filled with the XLCT targets (GOS solutions).

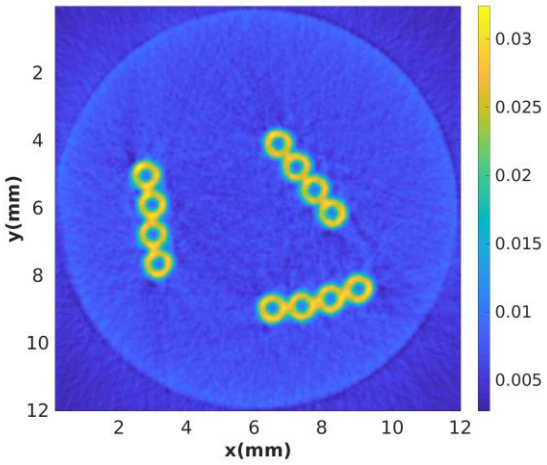

Figure 3.6. Reconstructed CT image with the FBP algorithm

XLCT Reconstructed images from the three different fiber setups are shown below in Fig. 3.7, with the detector numbers of (a) one, (b) two, and (c) four, respectively. We can see that all the targets are successfully reconstructed at the correct locations. And in Fig. 3.7(d), we have overlaid Fig. 3.6 with Fig. 3.7(c), in which the CT targets (the green circles) are overlaid very well with the XLCT targets (the red dots). As shown in Table 3.1, the DICE similarity coefficients are calculated to be 79.92, 80.24, and 81.37 % with one, two, and four detectors, respectively. Based on these metrics, we can find that all the three setups have a high similarity between the reconstructed targets and the ground truth. And the setups with more detectors achieved slightly better DICE coefficients, which is as expected because of better efficiency of collecting photons from different directions.

And the reconstructed XLCT images also showed the reconstructed concentrations of the targets are correlated with the target concentrations. We have integrated the reconstructed signals of each targets group with the same concentration. The corresponding quantitative ratios among the three groups are calculated to be 1: 1.98: 3.06 for the one detector case, 1: 2.14: 3.42 for the two detectors case, and 1: 2.17: 3.55 for the four detectors case, as shown in Tab. 3.1. Those results have shown that the reconstructed target concentration ratio is very close to the real ratio.

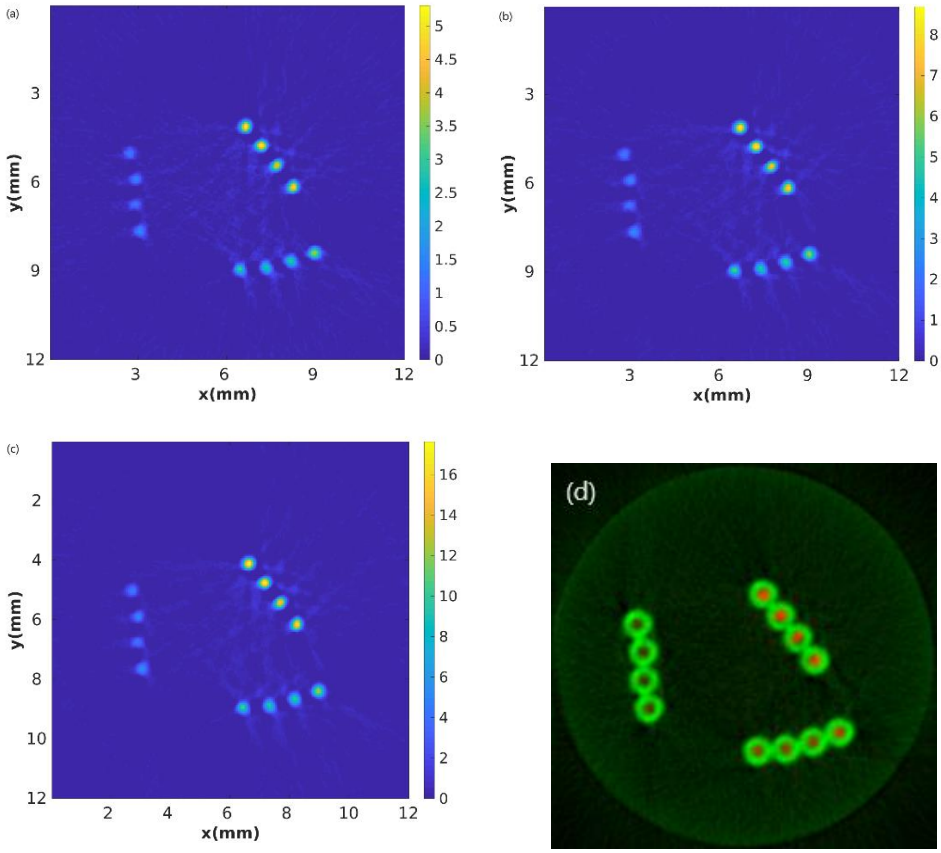

Figure 3.7. Reconstructed XLCT images with FBP for different detector numbers: (a) 1 detector, (b) 2 detectors, and (c) 3 detectors. (e) The overlaid figure of (c) with Fig. 3.6.

Detector numbers	DICE similarity coefficients	Quantitative ratios
1 detector	79.92%	1 : 1.98: 3.06
2 detectors	80.24%	1 : 2.14 : 3.42
4 detectors	81.37%	1 : 2.17 : 3.55

Table 3.1. Quantitative ratios and DICE similarity coefficients

The reconstructed images of the second phantom are shown below in Fig. 3.8. The reconstructed XLCT image is shown in Fig. 3.8 (left) and the parallel beam CT image is shown in Fig. 3.8 (middle). Fig. 3.8 (right) plots the overlaid image of 3.8 (left) and 3.8 (middle). From reconstructed XLCT image and the overlaid image, we can see that the XLCT imaging system is able to resolve all the three targets at the correct locations and separate them successfully. The edge-to-edge distance among the targets is 0.15 mm. It indicate the system has a spatial resolution of 0.15mm, which is equal to the focal x-ray beam size of the focus x-ray tube in the system.

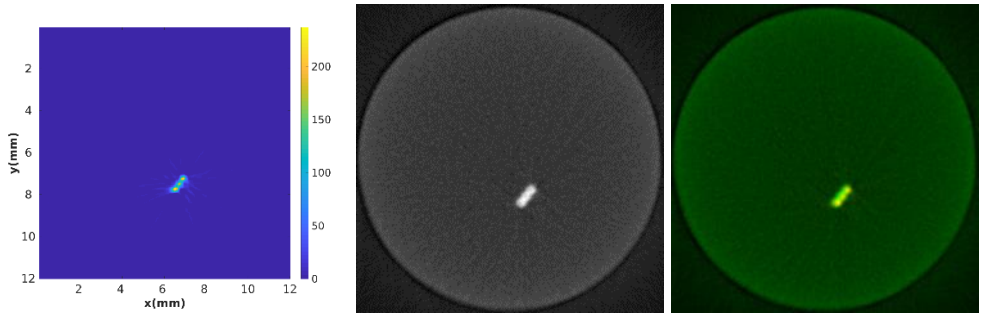

Figure 3.8. Reconstructed XLCT image (left), parallel beam CT image (middle), and the overlaid image (right) of the second phantom.

Similarly, the reconstructed results of the third phantom are shown below in Fig. 3.9. From these reconstructed images, we can see that the ten targets have been successfully resolved and are reconstructed at the correct locations, which the scanner is able to image non-sparse targets as well.

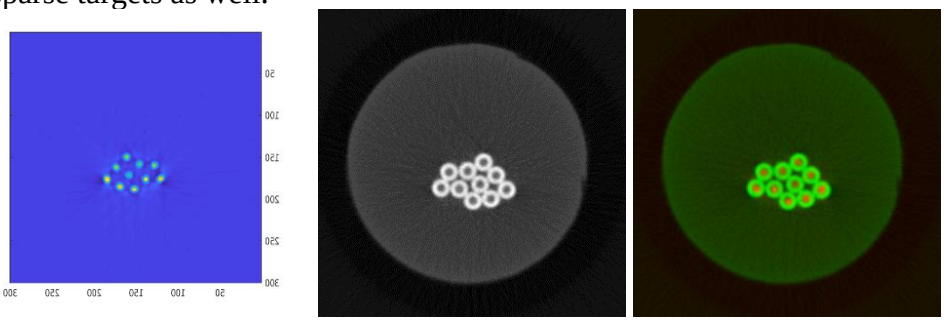

Figure 3.9. Reconstructed XLCT image (left), parallel beam CT image (middle), and the overlaid image (right) of the third phantom.

Fig, 3.10 shows the reconstruction images of the third phantom. The reconstructed XLCT image, parallel beam CT image, and corresponding overlaid image are shown in the left, middle and right, respectively. Fig. 3.10 (right) plots the overlaid image of 3.10 (left) and 3.10 (right). From these images, we can tell that the targets group with inner diameters of 0.58 mm, 0.4 mm, and 0.2 mm have all been resolved with great image quality.

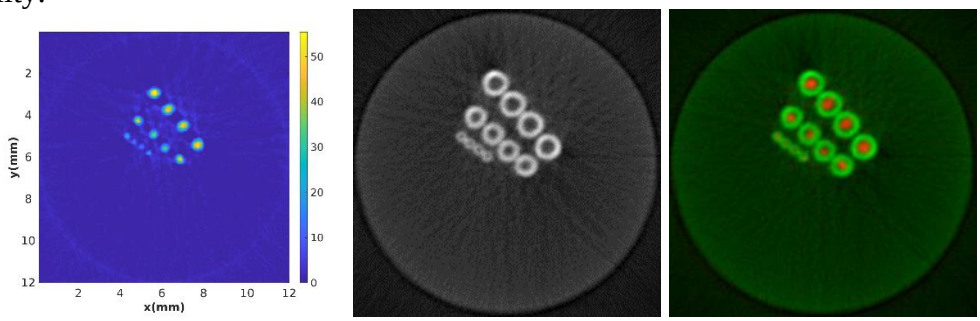

Figure 3.10. Reconstructed XLCT image (left), parallel beam CT image (middle), and the overlaid image (right) of the fourth phantom.

The reconstructed images of the nineth phantom are shown in Fig. 3.11. The reconstructed XLCT image, parallel beam CT image, and corresponding overlaid image are shown in the left, middle and right, respectively. Fig. 3.11 (right) plots the overlaid

image of 3.11 (left) and 3.11 (right). Here, we can conclude that the proposed XLCT imaging system has the capability of imaging a phantom with inregular structure,

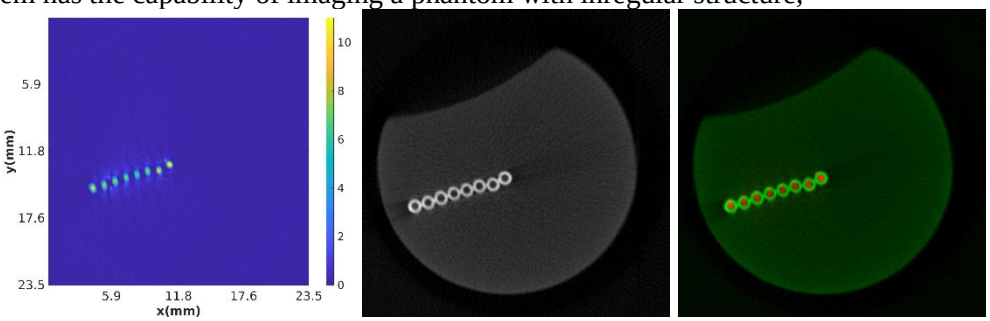

Figure 3.11. Reconstructed XLCT image (left), parallel beam CT image (middle), and the overlaid image (right) of the nineth phantom.

3.3.2 Three dimensional phantom experiments

The reconstructed 3D XLCT image (functional image) which indicates the $Gd_2O_2S:Eu^{3+}$ distribution of the fifth phantom is shown in Fig. 3.12 (left) and the 3D parallel beam CT image (structural image) is shown in Fig. 3.12 (middle). The overlaid result of the 3D functional image and the 3D structural image is shown in Fig. 3.12 (right). The parallel beam CT can show the boundary of the ager phantom, but the target is invisible because there are no glass tubes in this phantom. The X-ray luminescence imaging is the only way to reconstruct it.

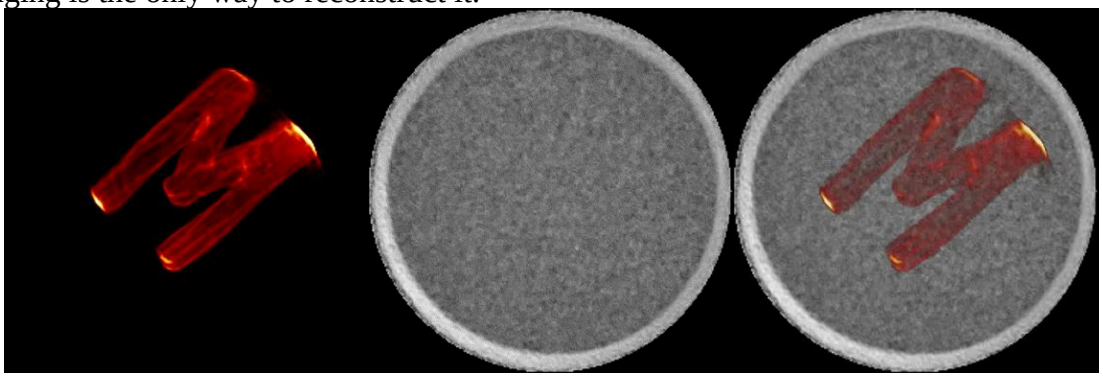

Figure 3.12. Reconstructed 3D XLCT image (left), 3D parallel beam CT image (middle), and 3D overlaid image (right) of the fifth phantom.

Similarly, the reconstructed 3D XLCT image, 3D parallel beam CT image and their overlaid image of the fifth phantom are shown in Fig. 3.13. We can see this custom designed 3D-printed target with complex structure has been reconstructed successfully with impressive spatial resolution.

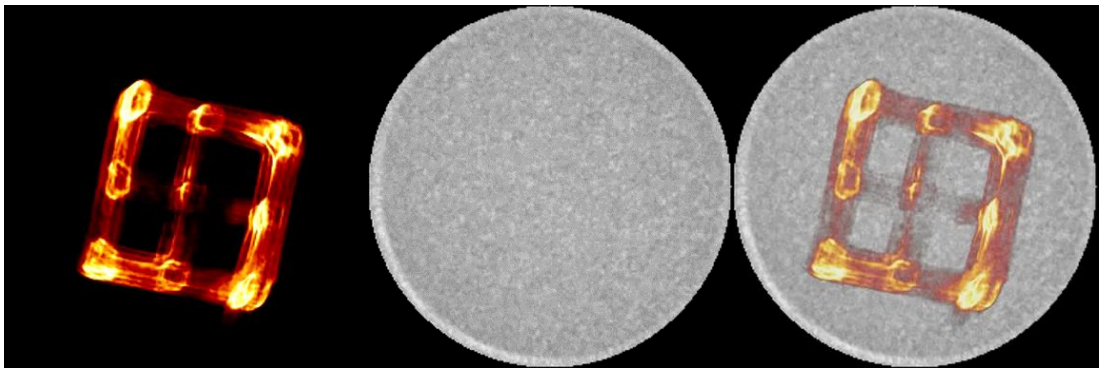

Figure 3.13. Reconstructed 3D XLCT image (left), 3D parallel beam CT image (middle), and 3D overlaid image (right) of the sixth phantom.

The reconstructed 3D XLCT image, 3D parallel beam CT image and their overlaid image of the seventh phantom is shown in Fig. 3.14, The angles of the triangular slot in the image is measured to be 90 degrees, 45 degrees and 45 degrees, which is consistent with the 3D design of the target.

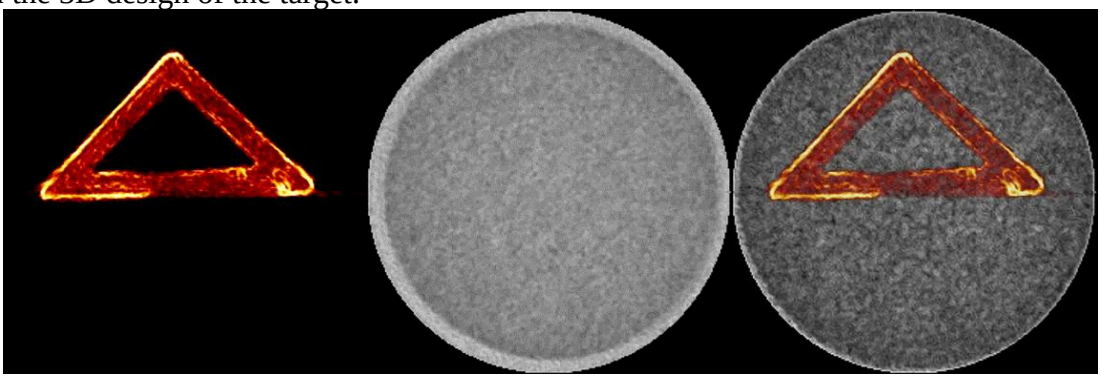

Figure 3.14. Reconstructed 3D XLCT image (left), 3D parallel beam CT image (middle), and 3D overlaid image (right) of the seventh phantom.

For the eighth phantom, the reconstructed 3D XLCT image which indicates the distribution of the $Gd_2O_2S:Eu^{3+}$ solution is shown in Fig. 3.15 (left) and the 3D parallel beam CT image which indicates the location of the glass capillary tubes is shown in Fig. 3.15 (middle). The overlaid result of the 3D functional image and the 3D structural image is shown in Fig. 3.15 (right). From the overlaid 3D image, we can see the 3D distribution of the $Gd_2O_2S:Eu^{3+}$ nanoparticles has been reconstructed successfully at the correct locations.

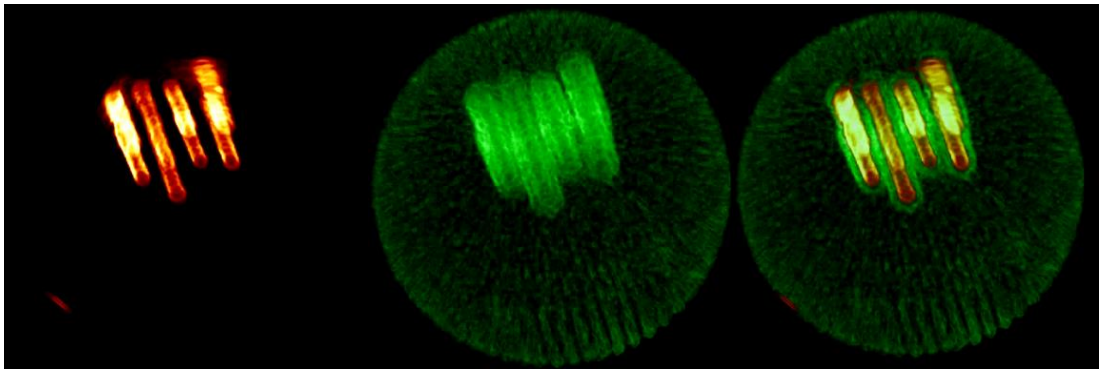

Figure 3.15. Reconstructed 3D XLCT image (left), 3D parallel beam CT image (middle), and 3D overlaid image (right) of the eighth phantom.

3.4 Discussion and conclusions

In this work, we have for the first time performed phantom studies on the quantitative correlations between the reconstructed signals of the phosphor targets and the target concentrations. We have upgraded the XLCT imaging system to increase the sensitivity in detecting x-ray induced photons. We have performed XLCT imaging with the parallel beam based CT image simultaneously. We have also developed a MATLAB program to sense the phantom boundary automatically. We have scanned a cylindrical agar phantom containing twelve targets filled with three different phosphor concentrations (2.5 mg/ml, 5 mg/ml, and 10 mg/ml) and successfully reconstructed both the parallel beam based CT image and the XLCT images using the FBP algorithm. We found a good correlation between the reconstructed signal of the targets and the target concentrations. Our experiments have shown that we have achieved good DICE similarity coefficients, especially for the case with four detectors. We have also performed 3D phantom experiments with custom designed 3D-printed targets and for the first time, obtained 3D functional images and 3D structural images simultaneously with a superfine x-ray beam. In future studies, we plan to apply this imaging system in preclinical applications [101], [106], and develop model-based reconstruction algorithm to achieve better quantitative result [107].

Acknowledgements: I would like to thank Yibing Zhang who made the ager phantom used in the experiments and assisted me to perform the phantom experiment. I have built and upgraded the XLCT imaging system, developed a C++ based program controller, operated the phantom experiments, and performed the data analysis and image reconstruction in this work.

CHAPTER 4

DEVELOPMENT OF FAST AND THREE-DIMENSIONAL FXLT SYSTEM

4.1Introduction

X-ray luminescence computed tomography (XLCT) was introduced in the past decade as a hybrid molecular imaging modality combining the merits of both X-ray imaging (high spatial resolution) and optical imaging (high sensitivity to tracer nanophosphors). Particularly, the narrow X-ray beam based XLCT has been shown to have very high spatial resolution at depths of several centimeters with good molecular sensitivity inside turbid media [75, 76]. Briefly, X-ray photons excite X-ray excitable contrast agents inside specimens to emit optical photons that propagate to the object surface to be measured by photodetectors. These measurements are used for model based XLCT image reconstructions usually with the anatomical guidance of X-ray beam position for better spatial resolution. The first demonstration of XLCT imaging was reported by Pratx et al. using a selective excitation scanning scheme, much like the first generation pencil beam based X-ray CT scanners [77, 78] and then by many other groups [79-81]. Our studies have demonstrated that the spatial resolution could be improved to be close to the X-ray beam size by reducing the scanning step size to be smaller than the X-ray beam size [89]. Our previous work has showed that the scan time could be improved by introducing a continuous scanning scheme where the X-ray beam moves across the object continuously [69]. Furthermore, we have showed that the data acquisition time can be further reduced by using a gated photon counter to replace the high-speed oscilloscope [71]. In another work, we have developed a deep-learning based reconstruction algorithm to reduce the number of angular projection views [101]. To perform multi-color FXLT imaging, we have synthesized biocompatible nanophosphors with bright and distinct X-ray luminescence spectra and compared them with commercially available nanophosphors [88]. In this study, based on our previous studies, we have designed and built a hybrid X-ray and optical molecular imaging tool, termed "focused X-ray luminescence tomography" (FXLT), which produces three-dimensional multi-agent/multi-probe XLCT images within a reasonable time, at high spatial resolution, and with high molecular sensitivity in deep tissue.

4.2 Methods

4.2.1 Design and build a fast and three-dimensional FXLT imaging system

Fig. 4.1 shows the design of the proposed FXLT imaging system. Briefly, there is a co-registered microCT imaging system on the same rotary gantry of the FXLT system. A custom-made optics board was mounted onto a ring track with a diameter of 650 mm, which was mounted to an aluminum frame. We used a high-precision servomotor

(SGM7A-04A6A6C, Yaskawa) to drive ring track and an encoder to track angular positions. On the rotary gantry, there is a cone beam X-ray tube (XTF5011, Oxford Instruments) for the microCT imaging and a focused beam X-ray tube (fleX-Beam, XOS) with a superfine focal spot size of 49.9 micrometer for FXLT imaging. The high voltage power supplies of each tube, and an X-ray detector (Shad-o-Box 1KHS, Teledyne DALSA) for the microCT, and a scintillator crystal as a single pixel detector to sense the focused beam intensity were mounted on the rotary gantry. A PMT (H8259-01, Hamamatsu) connected with the scintillator via light guide was also mounted on the gantry. We used a heavy-duty linear stage (NLS4-20-12, Newmark Systems Inc.) to translate the XOS X-ray tube at a high speed and a good position precision [101]. The heavy-duty linear stage was also mounted on the rotary gantry. All the power cables and wires from the instruments on the gantry were bundled into a single big cable which was wired on a rotary disk so that the gantry could be rotated up to 540 degrees freely without any problems with the cable. So far, we used four fiber bundles mounted in the gantry center through a big hole to measure the emitted optical photons at four wavelengths. These four fiber bundles were not rotated with the gantry. These four fiber bundles delivered photons to four PMTs (H7422-50, Hamamatsu) with four different bandpass optical filters. We used four broadband pre-amplifiers (SR455A, Stanford Research Systems) with low-pass filters (BLP-10.7+, fc = 11 MHz, Mini-Circuits) to amplify the PMT signals and then used two dual-channel gated photon counters (SR400, Stanford Research Systems) to record the measurements. We used another gated photon counter to record the data from the scintillator crystal to sense the object boundary. A large adapter wheel was designed for cable management. Two custom plastic boards were placed between the wheel and the optics board for cable protection and light shielding. We used another linear stage mounted on the bottom surface of the cabinet to move the imaged object into the field of view (FOV) of the microCT and then the FXLT. The object stage was designed to have low X-ray attenuation. And there are two slots in the stage so that the two fiber bundles can measure the photons about 1 mm away from the object's surface. Custom designed lead-lined stainless-steel panels and door were used to shield X-ray radiation and to prevent ambient light photons into the scanner. In the bottom layer of the frame, we placed the power supply and linear stage controllers.

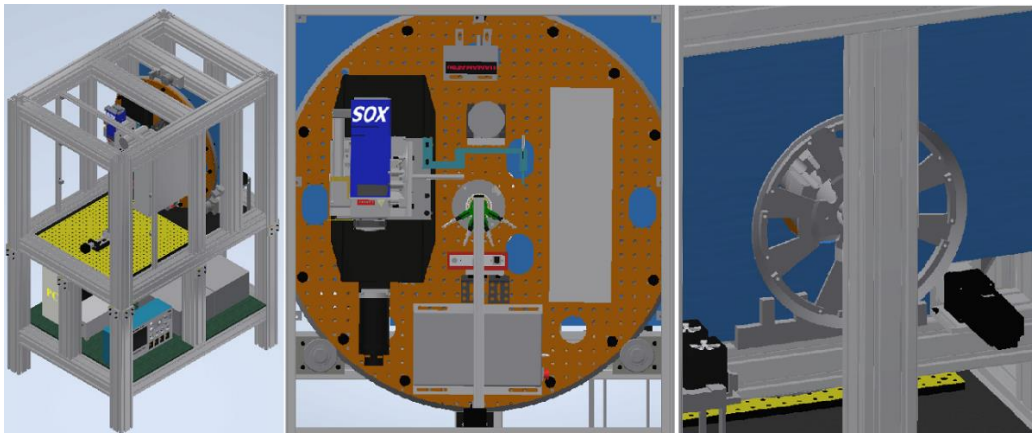

Figure 4.1. Design of the FXLT imaging system.

4.2.2 Develop a lab-made C++ based program controller

A lab-made C++ program was coded to control both FXLT and microCT imaging systems. The schematic of the program is shown in Fig. 4.2. Three motions were needed to obtain the 3D FXLT imaging. The first motion was to select the scanning transverse section by moving the object with the object linear stage controlled by the Performax communication API. Then, the angular projection was selected by the gantry rotation which was controlled by the servomotor which was programmed with the PLCi API. At last, the linear scan at each angular projection was performed by moving the focused X-ray tube with the heavy-duty linear stage that was programmed through the gclib (Galil Communication Library). The microCT detector was programmed through the Sapera™ LT API provided by the vendor. For each angular projection of microCT, we obtained one projection image with the X-ray detector. The single pixel detector, the crystal mounted by a specially designed holder onto the focused X-ray tube, was measured by the PMT with output of TTL signals which were recorded directly with the photon counter. This photon counter was programmed with the NI-488M functions [93]. Together with the two PMTs for the two-wavelengths measurements, we used three channels of two photon counters so that we were able to collect the boundary information of the scanned objects and the X-ray luminescent signals simultaneously during each linear scan. An automatic boundary detection program was developed to identify the object boundary by analyzing the measurements from the scintillator crystal. The interlock and the power control of two X-ray tubes were controlled by a lab-made Labview program. All the desired imaging parameters such as angular projection numbers, linear stage steps, and scan speed were fixed as program parameters before we performed the data acquisition.

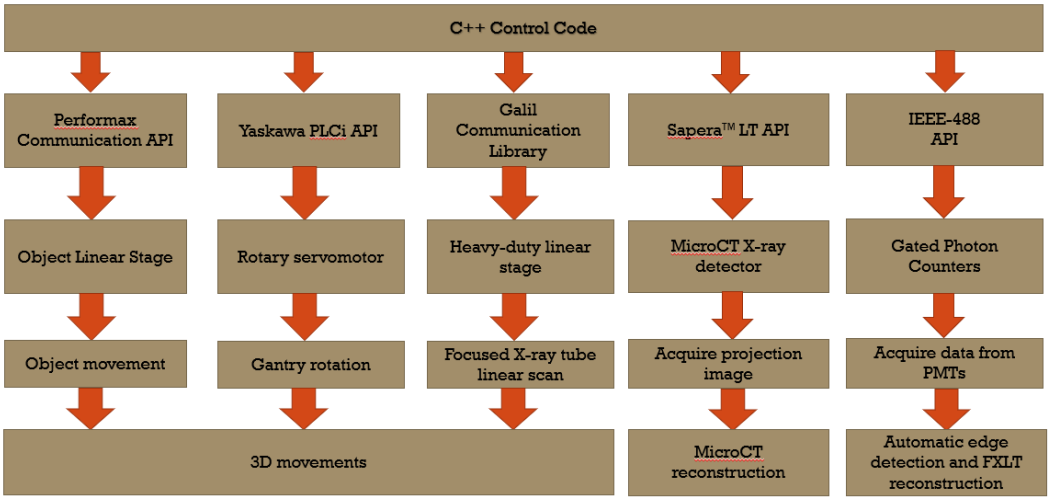

Figure 4.2. schematic of the C++ based program controller.

4.2.3 Cone beam microCT system calibration and evaluation

The microCT system was calibrated using a geometric calibration method as described in reference [108]. A ball-bearing phantom (BB phantom) was scanned three times using our microCT system. After the system was calibrated with the BB phantom, a cuvette made of plastic and metal was filled with water (Fig. 4.3) and then was scanned to evaluate the performance of the microCT system. For all microCT experiments in this study, the experimental parameters were the same. The X-ray tube was operated at 50 kVp and 0.4 mA. The measurements were acquired at 360 angular projections with an

angular step of 1 degree. For each angular projection, the expose time of the X-ray detector was 500 ms. A dark field image with the X-ray tube powered off and a flat field image without the object were captured after the scan. MicroCT images were reconstructed in MATLAB using a filtered back-projection algorithm with a Shepp-Logan filter.

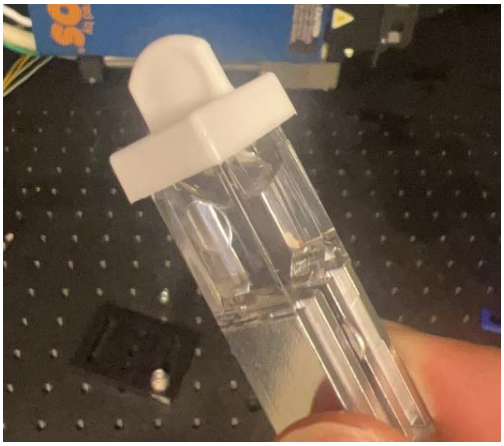

Figure 4.3. Cuvette filled with water and air.

4.2.3 Phantom experimental set-up

Multi-targets phantom experiments were performed in our system. A cylindrical phantom composed of 1% intralipid, 2% agar, and water with a diameter of 12 mm and height of 20 mm were made at our lab. Two glass capillary tube targets (outer diameter: 1.0 mm; inner diameter: 0.58 mm, standard glass capillaries, WPI) were filled with a solution of $Gd_2O_2S:Eu^{3+}$ (GOS:Eu) (UKL63/UF-R1, Phosphor Techn. Ltd.) at a centration of 10 mg/mL. The targets were embedded vertically and side by side in the background phantom. The phantom was first placed in the FOV of the cone beam microCT scanner to perform cone beam microCT scan to acquire the ground truth of the FXLT image. Then, the phantom was moved about 4 centimeters to the FOV of the FXLT scanner via the object linear stage for XLCT scanning. During the XLCT experiments, the XOS X-ray tube was operated at 30 kVp and 0.5 mA. The measurements were acquired at 6 angular projections with an angular step of 30 degrees. For each angular projection, the linear stage scanned in a continuous motion for an over-travelled distance of 20 mm to ensure covering the whole phantom. During each linear scan, the photon counter acquired the photon peaks in a measurement time of 10 ms every 50 μm. We took measurements at the transverse section at the scan depth of 3.0 mm. The automatic boundary detection program selected the measurement data for each linear scan.

After the 2 targets phantom experiment was finished, three cylindrical phantoms composed of the same ingredients with a diameter of 20 mm and height of 30 mm were made. The first phantom was vertically embedded 9 glass capillary tube targets (outer diameter: 0.8 mm; inner diameter: 0.4 mm, Drummond Scientific). 8 of the targets were filled with the same solution of $Gd_2O_2S:Eu^{3+}$ and placed side by side in a line. One of the targets was empty and placed away from the other eight targets to provide negative contrast. The second phantom was vertically embedded 20 glass capillary tube targets filled with the same solution of $Gd_2O_2S:Eu^{3+}$. The 20 targets were equally divided into four groups at different size (outer diameter: 1 mm, 0.8mm, 0.4mm, and 0.3 mm; inner diameter: 0.58 mm, 0.4mm, 0.2mm, and 0.1mm). Each size group has 5 targets. The third phantom was vertically embedded 12 glass capillary tube targets of the same size as the

first one. The 12 targets were equally divided into three groups and filled with $Gd_2O_2S:Eu^{3+}$ solutions at different concentrations (2.5, 5, and 10 mg/mL). Each concentration group has 4 targets. The cone beam microCT scans of the three phantoms were performed with the same experimental parameters as pervious experiments. And for the XLCT scans, 180 angular projections of measurements with an angular step of 2 degrees were captured to perform pencil beam XLCT imaging and the parallel beam CT imaging simultaneously. For each angular projection, the linear stage translated an over-travelled distance of 24 mm to ensure covering the whole phantom. All the other experimental parameters in the XLCT scans were the same as in the 2 targets phantom experiment.

Following the single section scan of phantom experiments, we made another two cylindrical phantoms to perform XLCT scans of multiple transverse sections and achieve three dimensional XLCT imaging. The two phantoms were also composed of the same ingredients and had a diameter of 20 mm and height of 30 mm. The first phantom was obliquely embedded with 10 glass capillary tube targets. The targets all have an outer diameter of 0.8 mm and an inner diameter of 0.4 mm. All the targets were filled with the solution of $Gd_2O_2S:Eu^{3+}$ at a centration of 10 mg/mL. The 10 targets were equally divided into two groups and inserted into the phantom at symmetrical angles. The two sets of tubes were cross inside the phantom. The second phantom was embedded with a unique 3D-printed target. The target was 3D-printed from UV-Curing resin blended with $Gd_2O_2S:Eu^{3+}$ powder at a centration of 10 mg/mL. The target was designed printed into a board with a "UCM" shaped hollow. The two phantoms were scanned by the cone beam microCT scanner with the same experimental parameters. And for the XLCT scans, the XOS tube was operated at 30 kVp and 1 mA. The first phantom was scanned for 15 transverse slices with a vertical step size of 0.5 mm. And 9 transverse slices of scan with a vertical step size of 0.78 mm were performed for the second phantom. For each transverse section, 90 angular projections of measurements with an angular step of 4 degrees were captured. And for each angular projection, the photon counter acquired 10 ms of data every 100 μm. All the other experimental parameters in the XLCT scans were the same as in previous XLCT experiments.

The cone beam microCT images and the parallel beam CT images were reconstructed in MATLAB using a filtered back-projection (FBP) algorithm with a Shepp-Logan filter. For XLCT imaging, the results from the 2 targets phantom experiment were reconstructed with the L_1 regularized majorization-minimization algorithm. The reconstruction is similar to fluorescence molecular tomography (FMT) [95]. XLCT images were reconstructed using an optical photon propagation model (radiative transport equation) inside turbid media and the X-ray beam's size and location were included as anatomical priors. Details of the algorithm were described in references [95-99]. For all the other phantom experiments, the reconstructions of both the XLCT imaging and the parallel beam CT imaging were used the FBP algorithm because sufficient number of projections were measured during the experiments.

4.3Results

4.3.1 System construction

A photo of the custom-manufactured optics board of the proposed FXLT imaging system is shown in Fig. 4.4 (left). All instruments have been installed and tested. Both the servomotor and the heavy-duty linear stage are powerful enough to rotate the gantry and move the focused X-ray tube with the heavy loads. The scintillator crystal is mounted

onto a specially designed adapter to avoid touching any fibers and cables while moving together with the focused X-ray tube on the heavy-duty linear stage. The cable management wheel adapter, as shown in Fig. 4.4 (middle), can roll up or loose the big cable bundle between the instruments on the optics board as the servomotor rotates the gantry via the ring track as shown in Fig. 4.4 (right). Fig. 4.5 shows the outside view of the FXLT imaging system (left), and the device placed in the bottom layer of the frame (right).

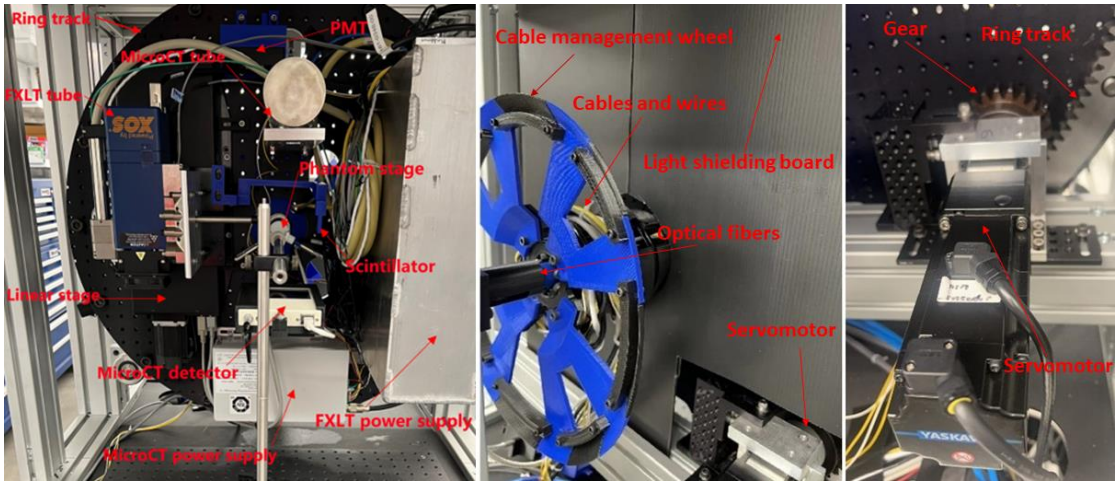

Figure 4.4. Photographs of the FXLT imaging system (inside).

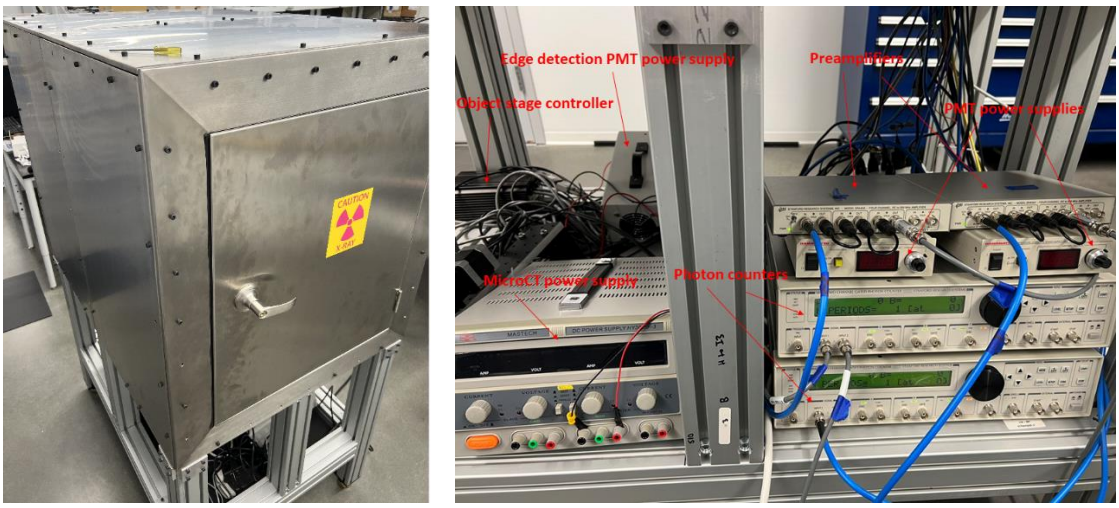

Figure 4.5. Photographs of the FXLT imaging system (outside).

4.3.2 Cone beam microCT system calibration

A projection image of the BB phantom used for the microCT calibration is shown in Fig. 4.6 (left). There are four balls in the FOV of the microCT system. Fig. 4.6(right) shows the orbital paths of individual BBs extracted from 360 projection images, from which we can calculate system parameters such as source-to-detector distance to calibrate the microCT imaging system. The microCT calibration algorithm is described in reference [108].

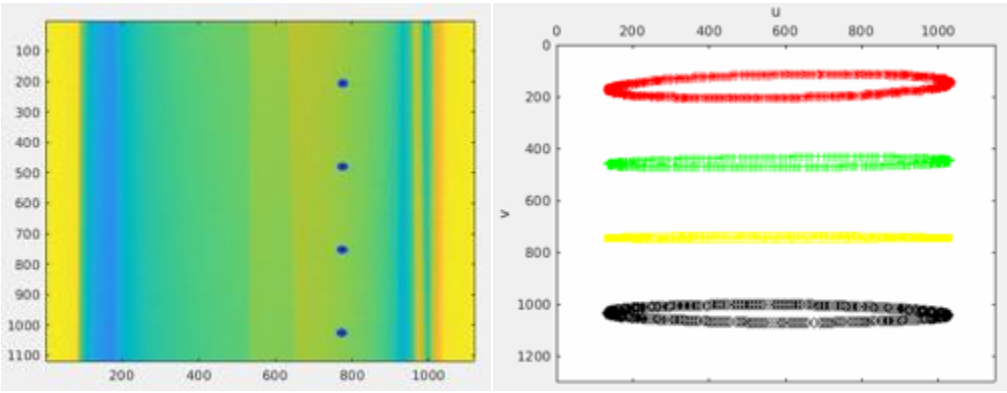

Figure 4.6. (left) A projection image of the BB phantom and (right) the orbital paths of these BB balls.

Fig. 4.7 shows the reconstructed cone beam microCT images of the cuvette phantom. Good resolution of the structure was achieved as shown by these images. We can also observe high contrast among water, air, plastic, and mental material of the cuvette.

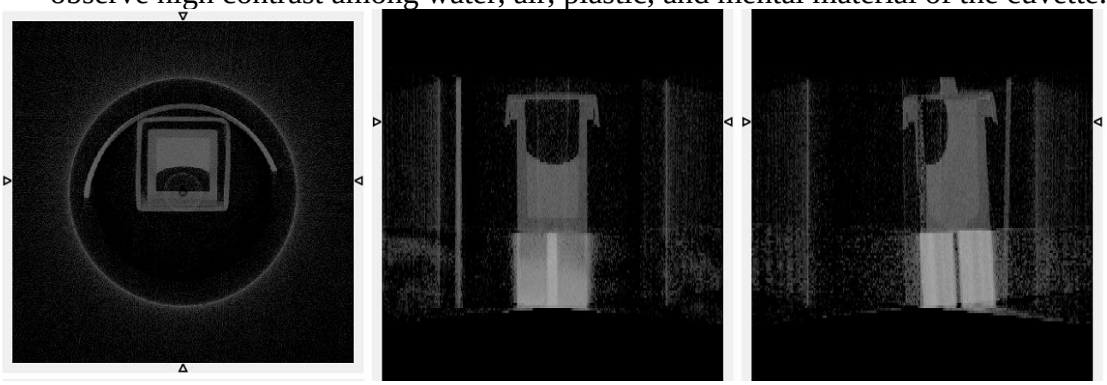

Figure 4.7. Reconstructed microCT images of the cuvette phantom.

4.3.3 Two dimensional phantom experiments

Fig. 4.8 plots one transverse section of the reconstructed cone beam microCT images of the phantom with two targets. The transverse section is the scanning section XLCT, from which we know the ground truth of the target size and positions. The edge-to-edge distance between the XLCT targets is measured to be 0.4 mm. The inner empty space inside the capillary tube as shown in the microCT images indicates the XLCT targets with a diameter of 0.58 mm.

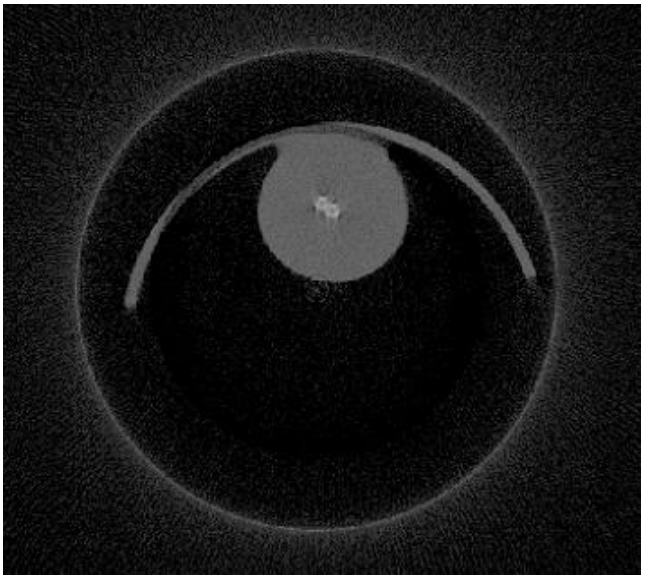

Figure 4.8. Ground truth of the phantom obtained from the cone beam microCT system.

The reconstructed XLCT image of the phantom from the FXLT scanner is shown in Fig. 4.9 (left) and the zoomed in target region is shown in Fig. 4.9 (right). The green circles indicate the ground truth of the targets obtained from the microCT image as shown in Fig. 4.8. From these results, we can see that the targets have been successfully resolved and are reconstructed at the correct locations. To quantitatively evaluate the reconstructions, the DICE similarity coefficients are calculated to be 86.76%, which is very impressive.

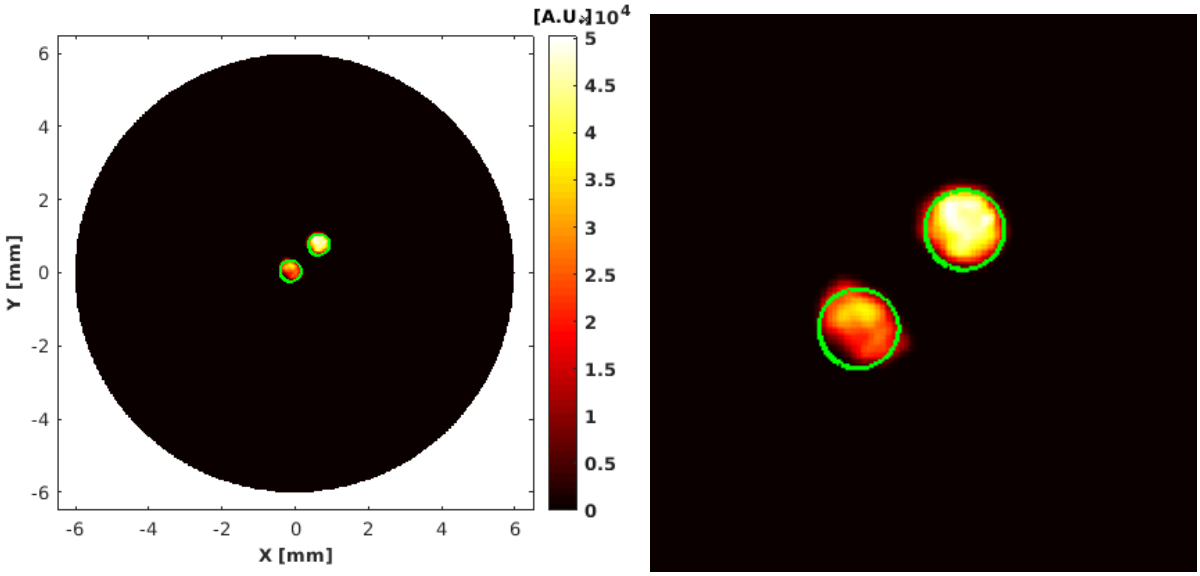

Figure 4.9. Reconstructed XLCT image of the two targets phantom.

Fig 4.10 shows the reconstruction results of the phantom with targets of negative contrast. The reconstructed XLCT image is shown in Fig. 4.10 (left) and the parallel beam CT image is shown in Fig. 4.10 (middle). Fig. 4.10 (right) plots the overlaid image of 4.10 (left) and 4.10 (middle). From these results, we can see that all the 8 targets have been successfully resolved and are reconstructed at the correct locations. The target with negative contrast is invisible in the XLCT image as expected. Good DICE similarity

coefficients of 86.86% have been achieved.

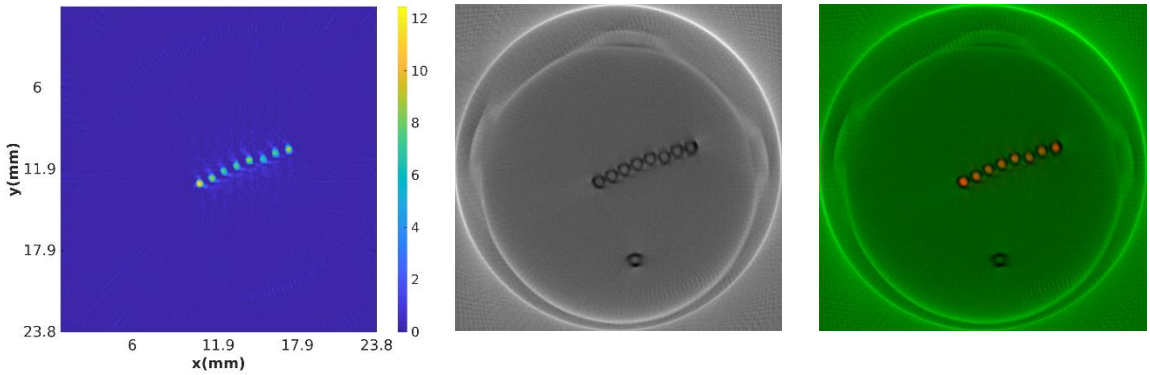

Figure 4.10. Reconstructed XLCT image (left), parallel beam CT image (middle), and the overlaid image (right) of the phantom with targets of negative contrast.

The reconstructed images of the phantom with 20 targets of different sizes are shown in Fig. 4.11. The reconstructed XLCT image, parallel beam CT image, and corresponding overlaid image are shown in the left, middle and right, respectively. Fig. 4.11 (right) plots the overlaid image of 4.11 (left) and 4.11 (middle). From these images, we can tell that the targets group with inner diameters of 0.58 mm, 0.4 mm, and 0.2 mm have all been resolved with great image quality. For the targets group with an inner diameter of 0.15 mm, three targets out of five have been resolved successfully. The overall DICE similarity coefficients are calculated to be 83.17%.

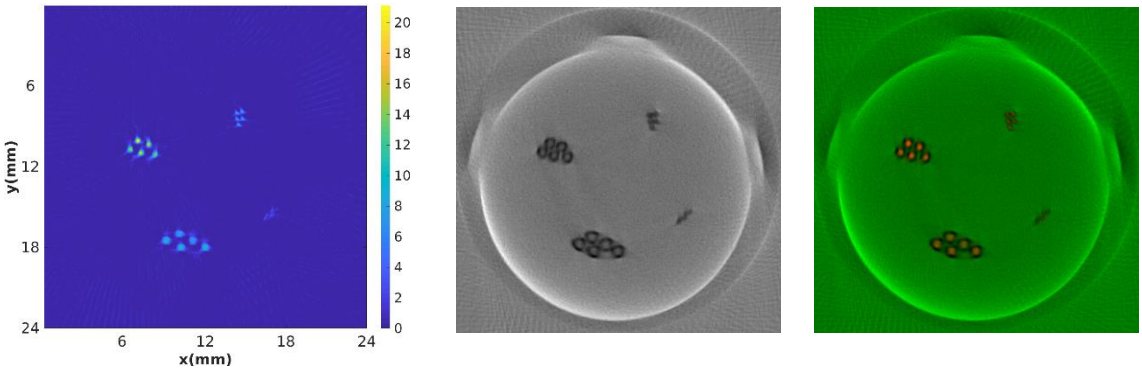

Figure 4.11. Reconstructed XLCT image (left), parallel beam CT image (middle), and the overlaid image (right) of the phantom with targets of different sizes.

And Fig 4.12 shows the reconstruction images of the phantom with 12 targets of different concentrations. The reconstructed XLCT image is shown in Fig. 4.12 (left), the parallel beam CT image is shown in Fig. 4.12 (middle), and their overlaid image is shown in Fig. 4.12 (right). Similar to the result from chapter 3, all the 12 targets have been successfully resolved and are reconstructed at the correct locations. To quantitatively evaluate the reconstructions, the DICE similarity coefficients are calculated to be 80.76%. And the ratio of the reconstructed signal among the three groups is 1: 1.79 : 3.8, which is very close to the ground truth ratio of 1: 2: 4.

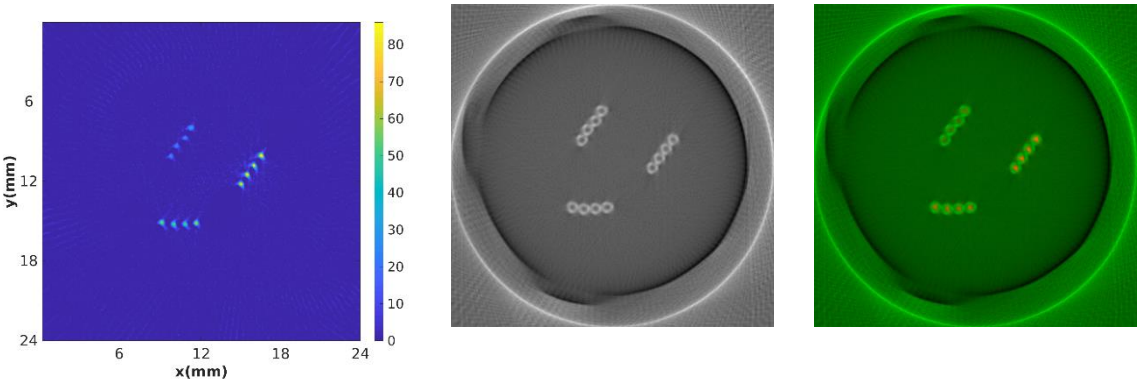

Figure 4.12. Reconstructed XLCT image (left), parallel beam CT image (middle), and the overlaid image (right) of the phantom with targets of different concentrations.

4.3.3 Three dimensional phantom experiments

Fig. 4.13 plots the reconstructed cone beam microCT images of the phantom with 10 cross targets. The three views of the images are shown in Fig. 4.13 (left) and the 3D visualization is shown in Fig. 4.13 (right).

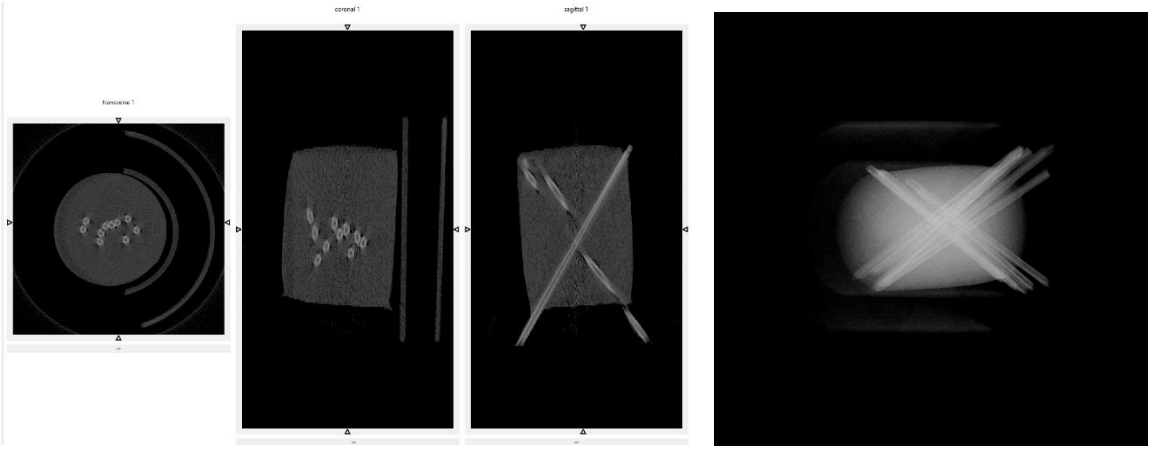

Figure 4.13. Reconstructed cone beam microCT images of the phantom with 10 cross targets.

The 15 slices of reconstructed XLCT images are shown in Fig. 4.14 and the corresponding 15 slices of parallel beam CT images are shown in Fig. 4.15. And from these images, we can get the 3D functional image which indicates the $Gd_2O_2S:Eu^{3+}$ distribution as shown in Fig. 4.16 (left) and the 3D structural image as shown in Fig. 4.16 (middle). The overlaid result of the 3D functional image and the 3D structural image is shown in Fig. 4.16 (right). From these impressive results, we can see that, for the first time, pencil beam based 3D XLCT image with high spatial resolution has been achieved.

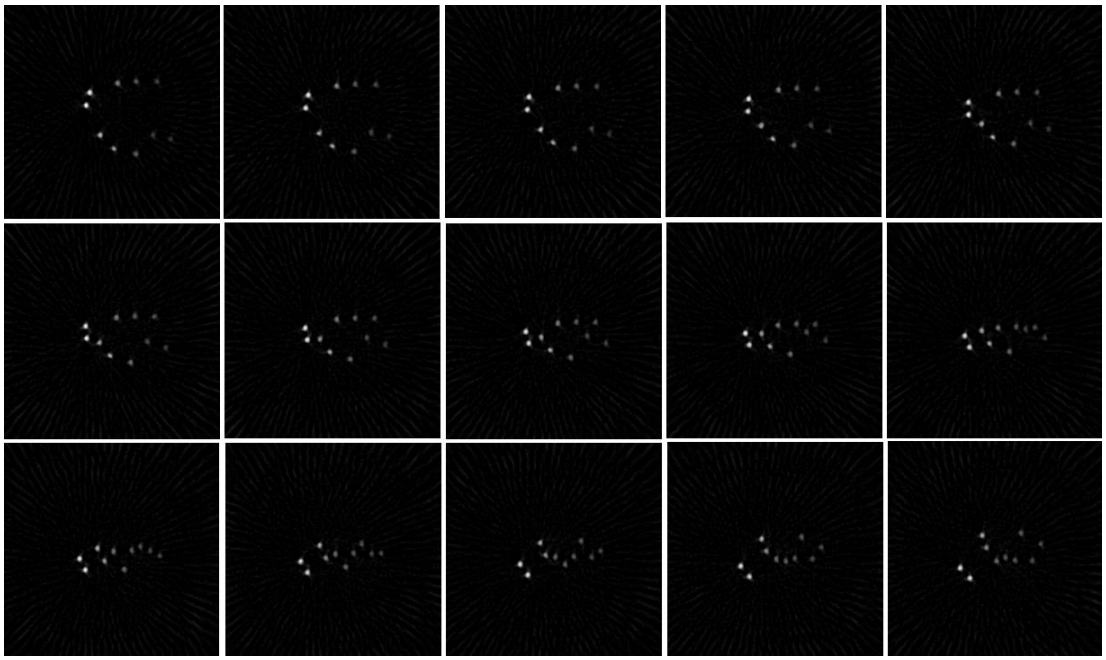

Figure 4.14. Reconstructed XLCT images of the phantom with 10 cross targets.

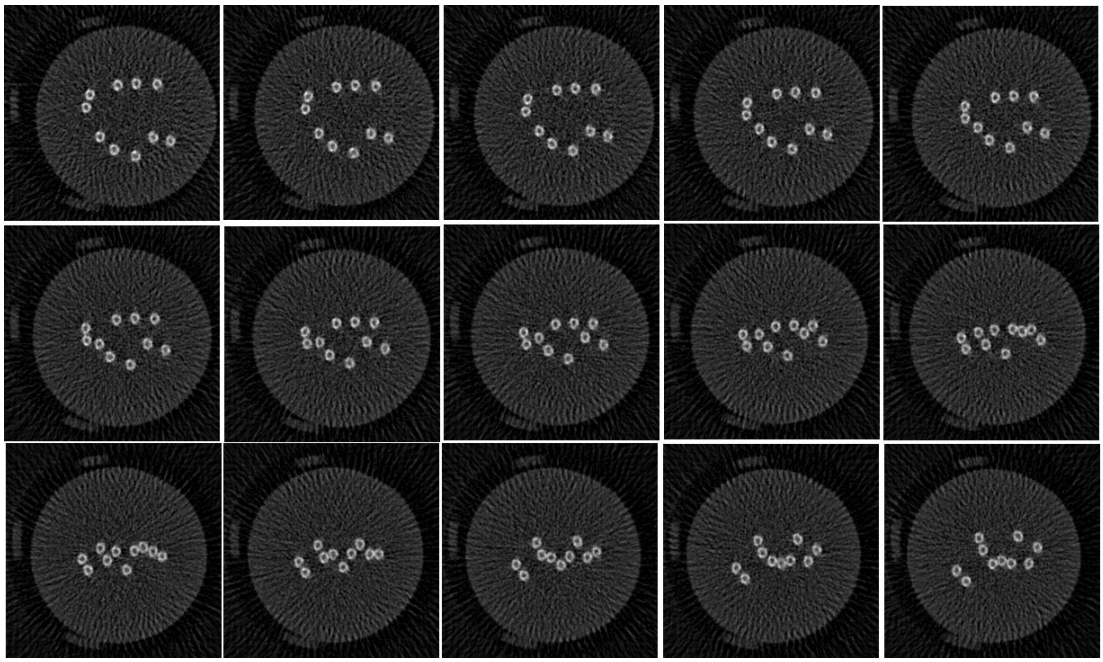

Figure 4.15. Reconstructed parallel beam CT images of the phantom with 10 cross targets.

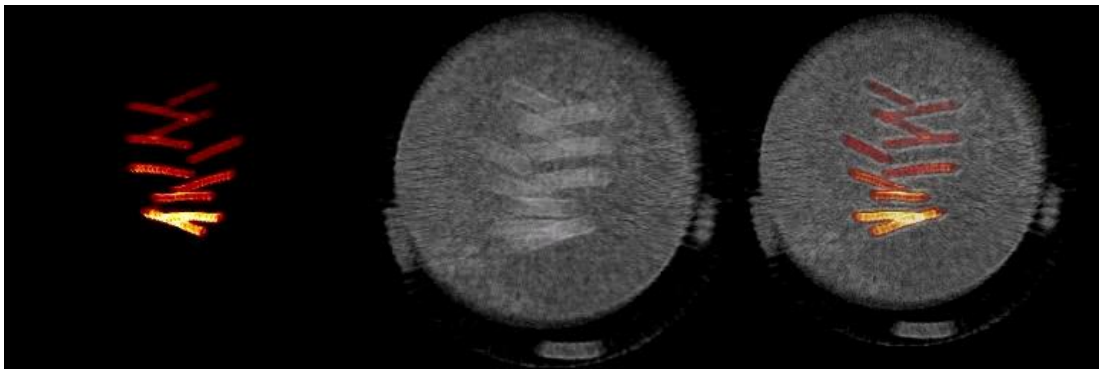

Figure 4.16. Reconstructed 3D XLCT image (left), 3D parallel beam CT image (middle), and 3D overlaid image (right) of the phantom with 10 cross targets.

Fig. 4.17 shows the reconstructed cone beam microCT images of the phantom with the 3D-printed target. The three views of the images are shown in Fig. 4.17 (left) and the 3D visualization is shown in Fig. 4.17 (right). We can see that the target is invisible in the Cone beam CT. This is because the x-ray attenuation coefficient of the 3D-printed target is smaller to the phantom and resulted in low contrast in x-ray attenuation-based CT imaging. Therefore, XLCT imaging is the only way to image the target in deep tissue.

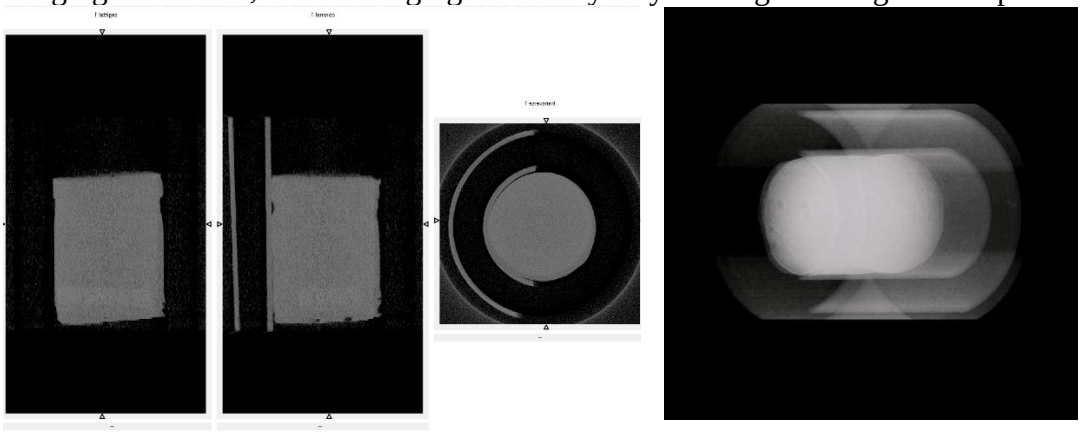

Figure 4.17. Reconstructed cone beam microCT images of the phantom with the 3D-printed targets.

The 9 slices of reconstructed XLCT images are shown in Fig. 4.18 and the corresponding 9 slices of parallel beam CT images are shown in Fig. 4.19. The 3D functional XLCT image, the 3D structural parallel beam CT image, and the 3D overlaid image are shown in Fig. 4.20 (left), Fig. 4.20 (middle), and Fig. 4.16 (right) respectively. We can find that both the cone beam microCT and the parallel beam CT are unable to image the target. And the 3D-printed board target with a “UCM” shaped hollow had a hot background, which is very challenging to image. But the results have shown the XLCT imaging still reconstructed the target successfully.

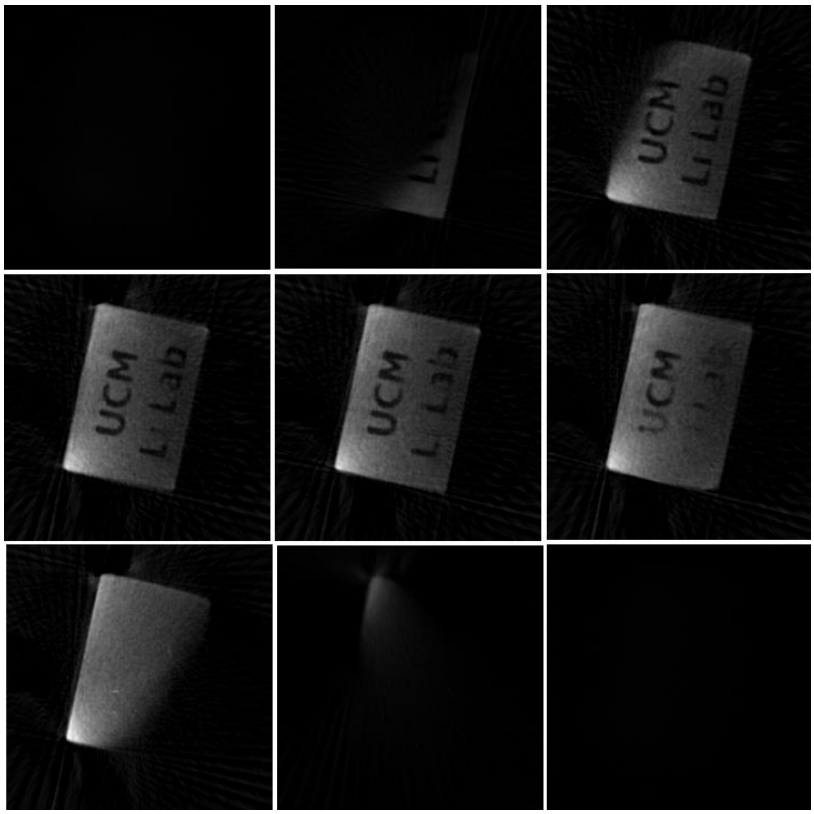

Figure 4.18. Reconstructed XLCT images of the phantom with the 3D-printed targets.

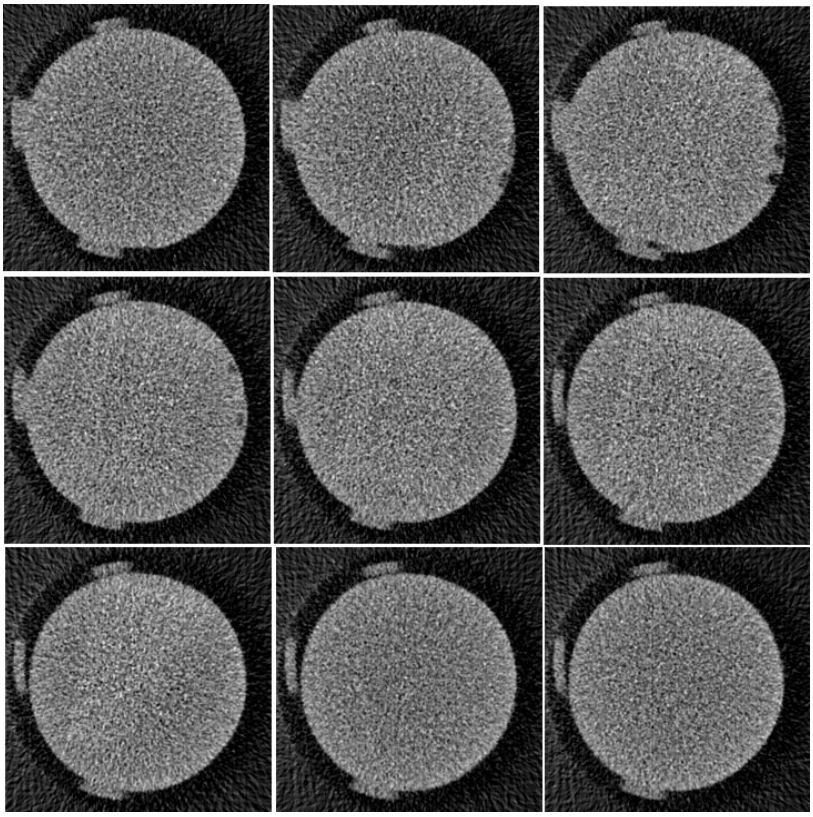

Figure 4.19. Reconstructed parallel beam CT images of the phantom with the 3D-printed targets.

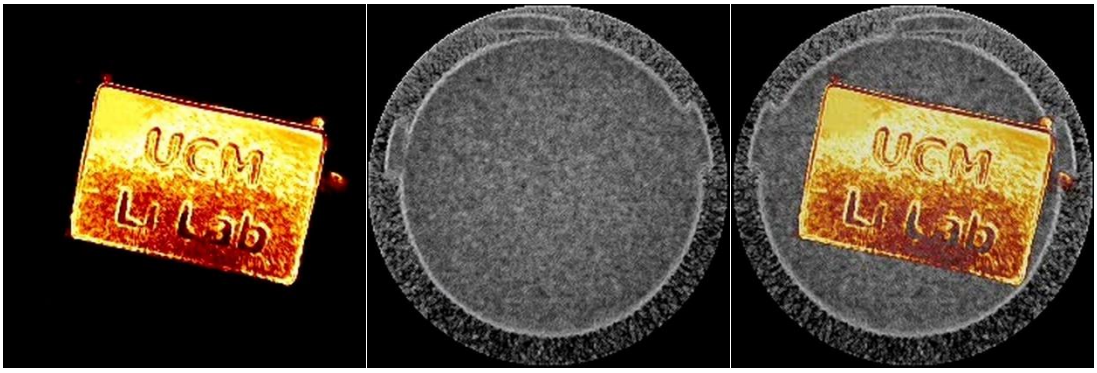

Figure 4.20. Reconstructed 3D XLCT image (left), 3D parallel beam CT image (middle), and 3D overlaid image (right) of the phantom with the 3D-printed targets.

4.4Conclusions

In this work, we have designed and built a first-of-its-kind fast and 3D FXLT imaging system. We finished the system assembly, the cable management and the X-ray leakage test. We have developed a lab-made control program to automate both microCT scan and FXLT scan. We performed the system calibration and evaluated the performance with phantom experiments. The quantitative evaluation shows great DICE coefficient and promising quantitative ratios. The results have demonstrated the feasibilities of our system and showed the high-spatial resolution capabilities. For 3D XLCT images, we moved the object axially so that different transverse sections were scanned. We plan to scan both euthanized mice with inserted capillary tubes as targets and in vivo mice with tumor targets and the experimental results will be reported soon. We will also use the machine learning algorithms for better XLCT reconstruction and will apply the bright nanoparticle to save the measurement time further [101].

Acknowledgements: I would like to thank Yibing Zhang who made the ager phantom used in the experiments and assisted me to build the FXLT imaging system. I also would like to thank Dr. Michael C. Lun who designed the 1st version of the FXLT imaging system and tested the functionality of some instruments. I have designed the upgraded FXLT imaging system, developed new scanning schemes, built and optimize the system, developed a C++ based program controller, operated the phantom experiments, and performed the data analysis and image reconstruction in this work.

CHAPTER 5

THREE-DIMENSIONAL IN VIVO IMAGING OF NANOPARTICLES IN MICE USING FOCUSED X-RAY LUMINESCENCE TOMOGRAPHY

5.1 Introduction

X-ray luminescence computed tomography (XLCT) was proposed as a hybrid imaging modality, and has shown great promise in overcoming the optical diffusion with X-ray localization [75, 76]. XLCT uses an X-ray beam to excite nanophosphors for tomographic imaging, with the emission location defined by the X-ray path and the molecular sensitivity enabled by luminescence probes [77, 78]. Using the precise location of the x-ray beam as a priori information in the reconstruction algorithm, narrow x-ray beam based XLCT imaging can achieve a high spatial resolution at the cost of a long acquisition time.

In our previous studies, we have improved the spatial resolution and the measurement speed of the narrow x-ray beam based XLCT imaging. To break the spatial resolution limit of previous study, we have proposed a scanning strategy achieved by reducing the scanning step size to be smaller than the x-ray beam size. Our numerical simulations and phantom experiment demonstrated the spatial resolution can be improved to close to the x-ray beam size [89]. To improve the imaging speed, we introduced a continuous scanning scheme to replace the selective excitation scheme [91]. In addition, we have used a gated photon counter to replace the high-speed oscilloscope to acquire measurement data [92]. Compared with the oscilloscope, the photon counter records much less data without losing any relevant information. The experimental results have verified the feasibility of our proposed approaches and the capability of 3D imaging within a reasonable time.

However, up to date, only preliminary benchtop systems have been developed to show proof-of-principle with phantom experiments [73, 106]. In order to overcome this problem, we have designed and built a first-of-its-kind Focused X-ray Luminescence Tomography (FXLT) imaging system based on a rotary gantry [101]. The FXLT system was specially designed for small animals in vivo studies. The small animal can lay down and keep stational on the object stage at the rotary center during the entire experiment. We have built and calibrated the proposal FXLT system with phantom experiments in pervious chapters [94]. To demonstrate the capacity of the FXLT system on small animal studies, we performed both euthanatized and in vivo mice experiments for 3D XLCT imaging at superhigh resolution.

5.2Methods

5.2.1 FXLT experimental system set-up

Fig. 5.1 shows photographs of the FXLT system set-up for the mice experiment. In chapter 4, this imaging system has been described in detail [94]. Briefly, there is a co-registered microCT imaging system on the same rotary gantry of the FXLT system. All the power cables and wires from the instruments on the gantry were bundled into a single big cable which was wired on a rotary disk so that the gantry could be rotated up to 540 degrees freely without any problems with the cable.

During the experiment, all the major devices expect the object stage will rotate together when the rotary gantry is driven by the high-precision servomotor. The mouse can lay down and keep stational on the object stage at the rotary center. We used two fiber bundles to collect x-ray induced photons from the nanoparticles because two out of four fiber bundles were removed to ensure there is enough space on the object stage for the mouse. We have set up an anesthesia system for the in vivo mice experiment. The system provides both anesthetic gas and oxygen through a plastic hose to keep the mice anesthetized and alive during imaging. A temperature control system by circulating warm water has been added to maintain the appropriate air temperature inside the experimental chamber during mice imaging.

Figure 5.1. Photograph of the imaging system (left), a zoomed-in view of the object stage (middle), and the anesthesia system outside the chamber (right).

5.2.2 Mice experimental set-up

5.2.2.1 Euthanized mouse with capillary tube targets

We first scanned a euthanized nude mouse with capillary tube targets using the FXLT imaging system. The mouse weighed 28.4 grams and had a glass capillary tube target inserted through its esophagus. The glass capillary tube target (outer diameter: 4.0 mm; inner diameter: 2 mm) was filled with a solution of $Gd_2O_2S:Eu^{3+}$ (GOS:Eu) (UKL63/UF-R1, Phosphor Techn. Ltd.) at a centration of 10 mg/mL.

The mouse was placed on the object stage at the rotary center of the FXLT system as

shown in Fig.5.2 (left). During the scan, the x-ray tube (fleX-Beam, XOS) was operated at 30 kVp and 1.0 mA. The measurements were acquired from 90 angular projections (4°/projection) for one transverse section. For each angular projection, the linear stage scanned in the fly-scanning scheme to capture as much data as possible and scanned a total distance of 36 mm to make sure that the mouse was scanned completely. Three channels of the photon counters were used to acquire all the photon pulses in a measurement time of 10 ms from three PMTs for each acquisition [72]. Two channels of the PMT signal recorded the X-ray induced optical luminescence photons to be used in the XLCT imaging and one channel recorded the information of the x-ray beam intensity by the single pixel scintillator detector for the parallel beam CT imaging. In this experiment, the linear scanning velocity is 2mm/second and the photon counter collected 395-400 acquisitions per projection. Based on the position information from the encoder, we select 360 acquisitions (0.1mm/ acquisition) of data for imaging reconstruction.

Figure 5.2. The euthanized mouse embedded with one capillary tube target (left) and the euthanized mouse embedded with three smaller capillary tube targets (right).

After the parallel beam CT and XLCT scan, the mouse was then placed in the FOV of the co-designed cone beam CT scanner to perform a cone beam CT scan for cross validation. For the cone beam CT scan, a cone beam x-ray tube (XTF5011, Oxford Instruments) was operated at 50 kVp and 0.4 mA and an x-ray detector (Shad-o-Box 1KHS, Teledyne DALSA) was operated at an exposure time of 456ms. We acquired data of 360 projections with the angular step size of 1 degree.

After the experiments of mouse with one capillary tube target were finished, the capillary tube target was pulled out from the mouse and replaced with three smaller glass capillary tube targets (outer diameter: 1.0 mm; inner diameter: 0.58 mm). The glass capillary tubes were filled with the same solution of $Gd_2O_2S:Eu^{3+}$ at the same centration. The mouse was placed on the object stage as shown in Fig.5.2 (right) and repeated the cone beam CT scan with the same experimental parameters and the parallel beam CT and XLCT scan of 10 transverse sections (1mm/section).

5.2.2.2 Live mouse with intratumorally administration

Before the experiments with the euthanized mice, a live nude mouse of 24.1 grams with two tumors was scanned by the same imaging system. Two xenografted tumors were introduced and grown to be around 1 centimeter in diameter for about three weeks. Before this experiment, for each tumor, we intratumorally administrated 0.1 mL of nanoparticle $Gd_2O_2S:Eu^{3+}$ solution at a concentration of 1 mg/mL. The tumors are located at the abdomen near the hind legs on each side of the mouse. The mouse was placed to lie down on the object stage at the rotary center of the FXLT system and breathed the anesthetic gas and oxygen through a plastic hose as shown in Fig. 5.3 (left). The mouse was scanned by the FXLT system approximately 40 minutes immediately after the nanoparticle injection.

Figure 5.3. The live mouse with intratumorally administration was anesthetized on the object stage (left) and was placed on the object stage after euthanasia (right).

For the parallel beam CT and XLCT scan, all the scanning parameters were the same as the previous experiments except the measurements were acquired from 4 transverse sections (0.508mm/section). The mouse was kept under anesthetized state during the total experiment time of 115 minutes for scanning 4 transverse sections.

After the parallel beam CT and XLCT scan, the mouse was then euthanized and performed a cone beam CT scan using the same experimental parameters as pervious cone beam CT scans.

Following the cone beam CT scan, the euthanized nude mouse was moved back to the FOV of the XLCT scanner to perform a 10-slice XLCT and parallel beam CT scan as shown in Fig. 5.3 (right). All the operation parameters were the same except the object stage moved 10 transverse sections (1.27mm/section).

5.2.3 Imaging reconstruction and evaluation

The cone beam microCT images were reconstructed in MATLAB using a filtered

back-projection (FBP) algorithm with a Shepp-Logan filter. For the XLCT imaging and the parallel beam CT imaging, the reconstructions were used the FBP algorithm because enough projections were measured during the experiments [72].

After all the scans were finished, the tumors were sliced into slices for cross validation. As shown in Fig. 5.4, the left tumor was sliced into 86 slices (0.1 mm/slice) on nine glass slides. Eight slides have 10 slices of tumor, and the 9th slide has 6 slices of tumor.

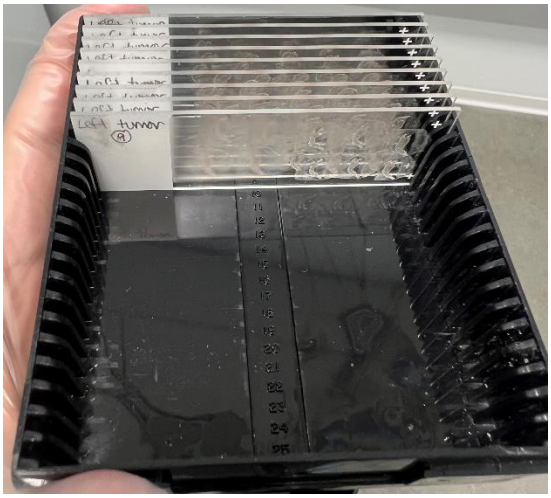

Figure 5.4. 86 slices of the left tumor on 9 glass slides.

The slices were then imaged by an EMCCD camera and an optical microscope. Fig. 5.5 (left) shows the benchtop EMCCD camera-based imaging system built in a lead-lined cabinet. We first image each glass slide with the EMCCD camera under optical light from the room lamp to obtain the structure and location of tumor slices. Then we turned off the lamp, closed the cabinet, turned on the cone beam x-ray tube at 50 kVp and 1.0 mA to excite the nanoparticles, and measured the x-ray induced optical photons with the EMCCD camera. Then, as shown in Fig 5.5 (right), the tumor slices were imaged by an optical microscope (DMi8, Leica) with a magnification factor of 10 and excited by a laser with a wavelength of 570 nm.

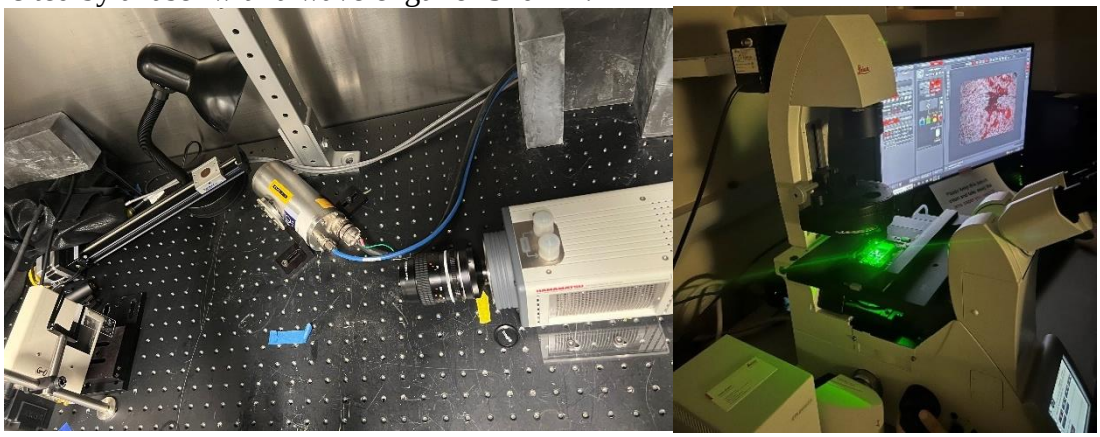

Figure 5.5. Imaging the tumor slice with: (left) EMCCD) camera and cone beam x-ray tube; (right) microscope with laser source.

5.3 Results

5.3.1 Euthanized experiments with capillary tube targets

Fig. 5.6 plots the reconstructed cone beam microCT images of the euthanized mouse with one capillary tube target (outer diameter: 4 mm; inner diameter: 2mm). The three views of the images are shown in Fig. 5.6 (left) and the 3D visualization is shown in Fig. 5.6 (right).

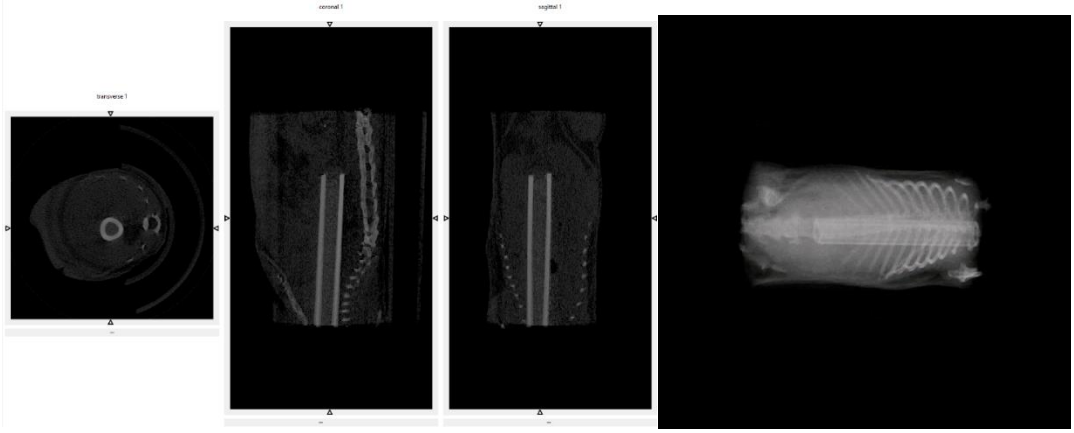

Figure 5.6. Reconstructed cone beam microCT images of the euthanized mouse with one capillary tube target.

The XLCT and parallel beam CT reconstruction results of the mouse are shown in Fig 5.7 (left) and Fig. 5.7 (right), respectively. And Fig. 5.7 (right) plots the overlaid image of the XLCT and parallel beam CT reconstructed image. From these results, we can see that the target has been successfully resolved and is reconstructed at the correct locations. And the size of the target matched the capillary tube' inner diameter of 2 mm.

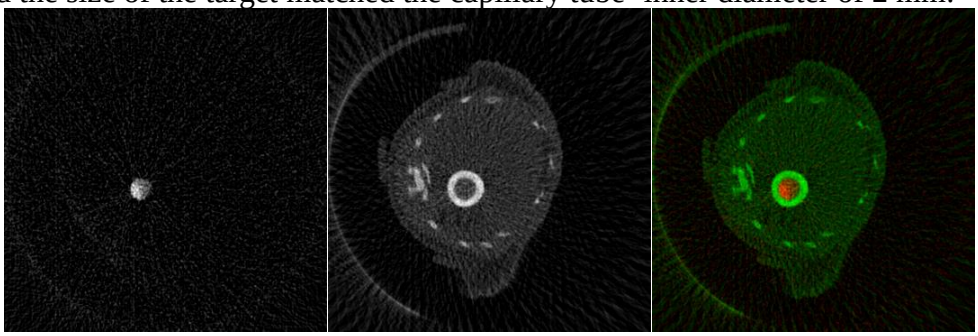

Figure 5.7. Reconstructed XLCT image (left), parallel beam CT image (middle), and the overlaid image (right) of the euthanized mouse with one capillary tube target.

Fig. 5.8 plots the reconstructed cone beam microCT images of the euthanized mouse with three capillary tube targets (outer diameter: 1 mm; inner diameter: 0.58mm). The three views of the images are shown in Fig. 5.8 (left) and the 3D visualization is shown in Fig. 5.8 (right).

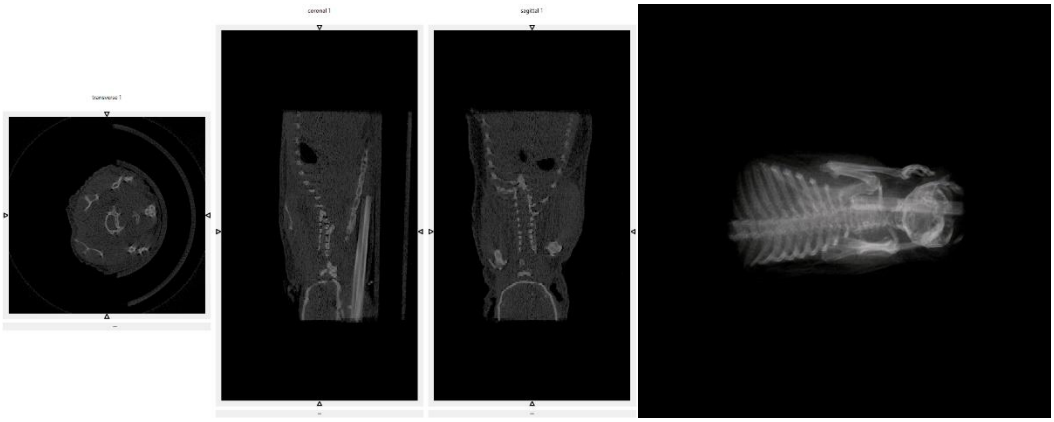

Figure 5.8. Reconstructed cone beam microCT images of the euthanized mouse with three capillary tube targets.

Similarly, the reconstructed XLCT images and parallel beam CT images of the mouse are shown in Fig 5.9 and Fig. 5.10 respectively. And Fig. 5.11 shows the reconstructed 3D results from the euthanized mouse experiment. The 3D XLCT image, 3D parallel beam CT image, and 3D corresponding overlaid image are shown in Fig. 5.11 (left), Fig. 5.11 (middle), and Fig. 5.11 (right), respectively. From these images, we can see that all the three targets have been successfully resolved and are reconstructed at the correct locations.

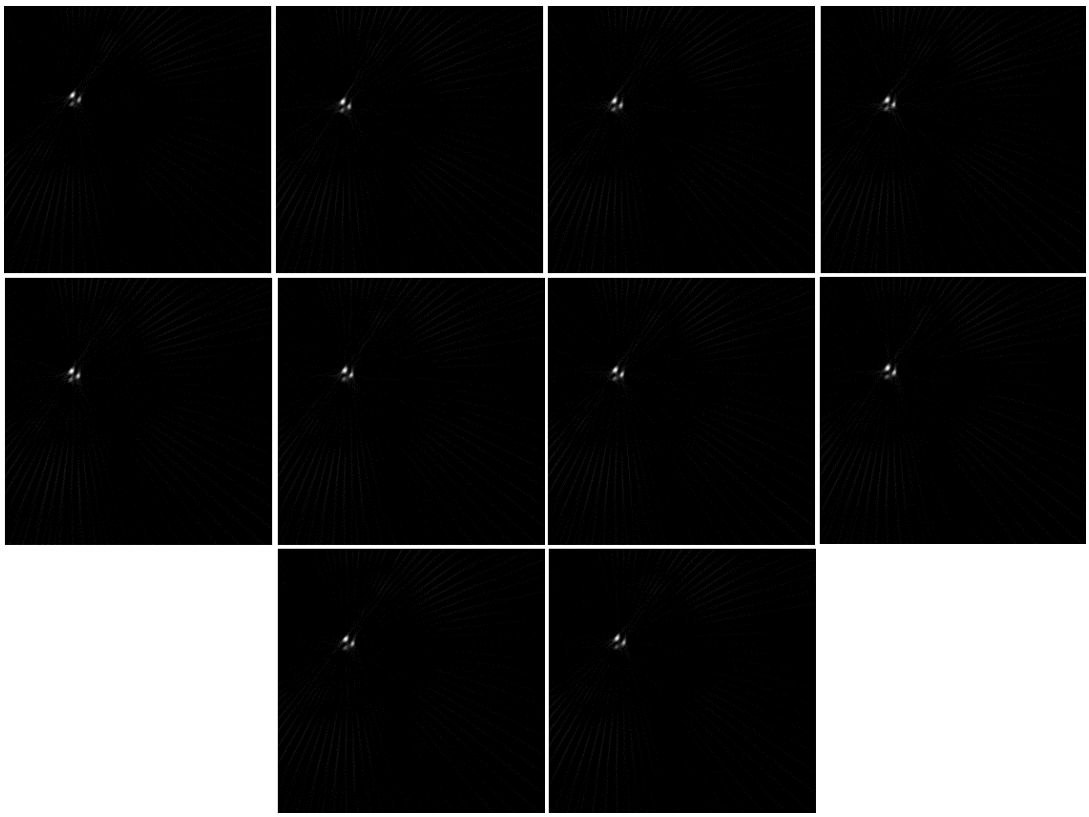

Figure 5.9. Reconstructed XLCT images of the euthanized mouse with three capillary tube targets.

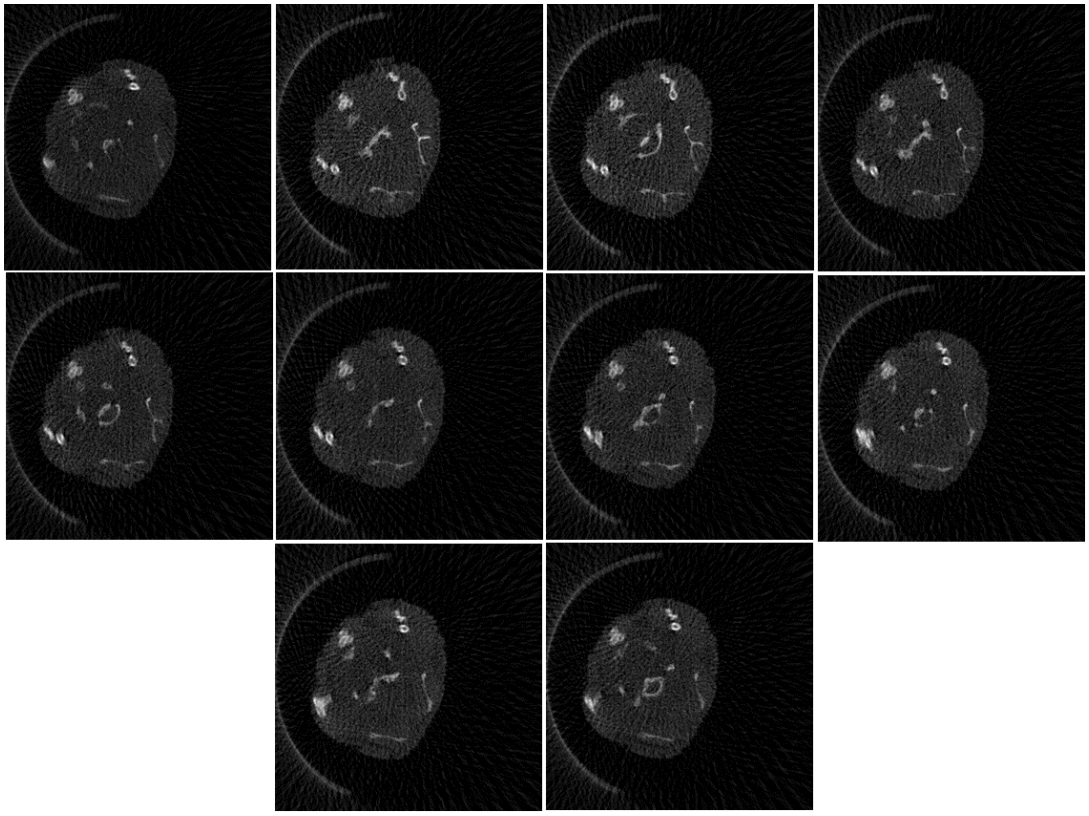

Figure 5.10. Reconstructed parallel beam CT images of the euthanized mouse with three capillary tube targets.

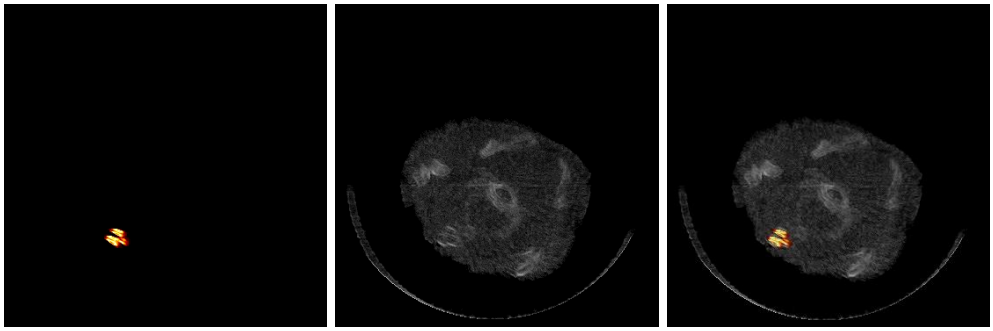

Figure 5.11. Reconstructed 3D XLCT image (left), 3D parallel beam CT image (middle), and 3D overlaid image (right) of the euthanized mouse with three capillary tube targets.

5.3.2 In vivo experiments with intratumorally administration

Fig. 5.12 shows the reconstructed functional XLCT images from the in vivo mouse experiment with different scanning depths, where we can see both tumors were successfully reconstructed. The corresponding reconstructed structural parallel beam CT images are shown in Fig. 5.13. We can find both tumors were reconstructed at the correct locations as shown in the overlaid images in Fig. 5.14.

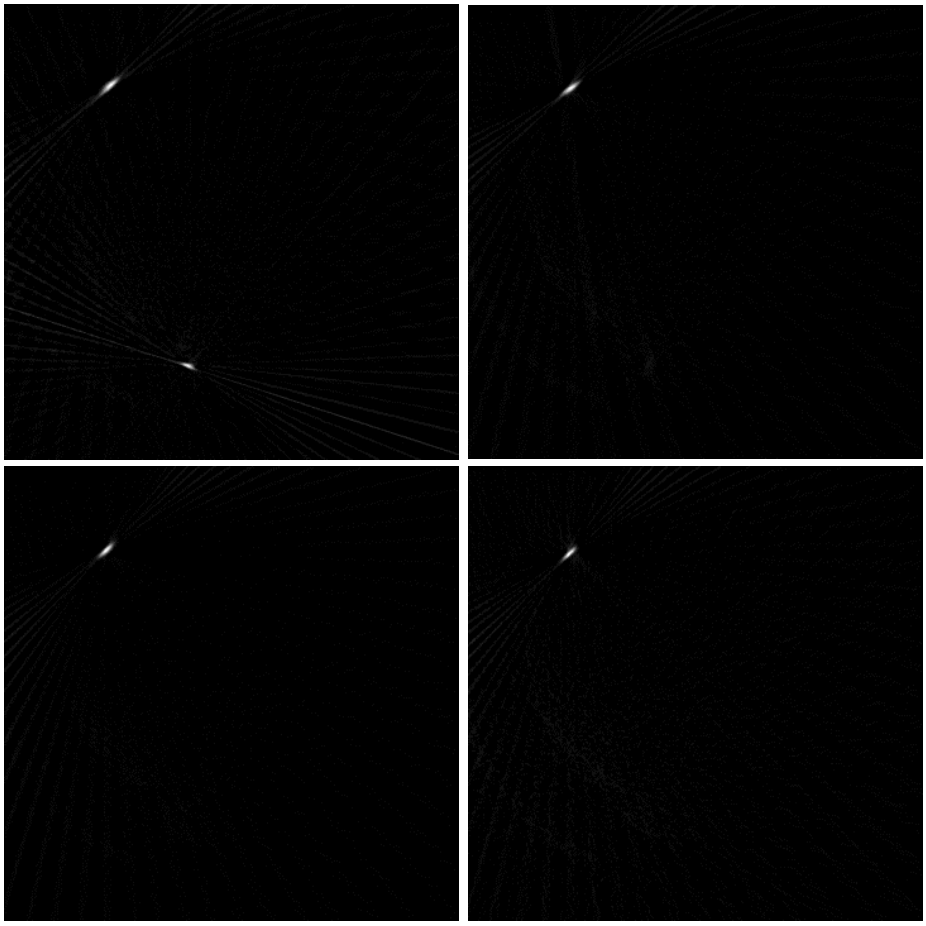

Figure 5.12. Reconstructed XLCT images of the live mouse with intratumorally administration.

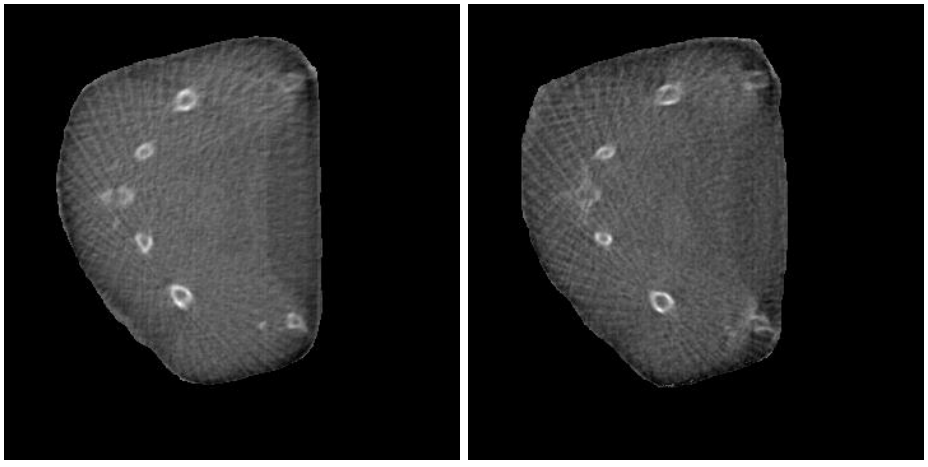

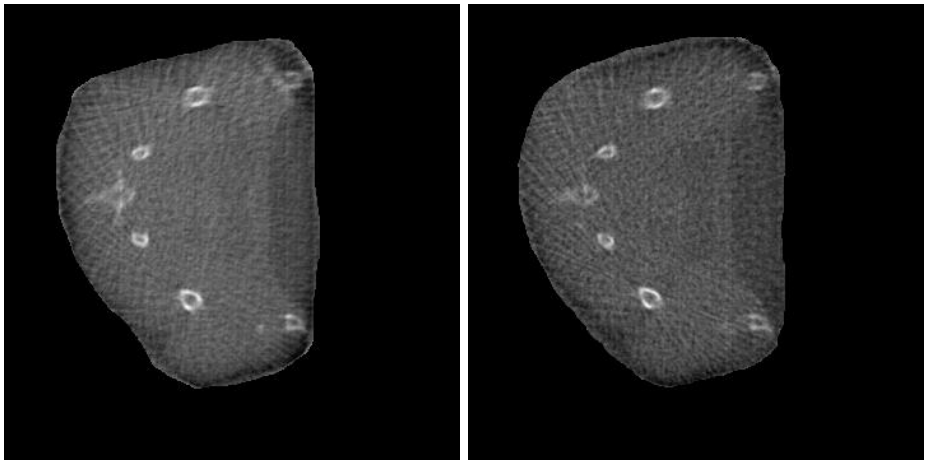

Figure 5.13. Reconstructed parallel beam CT images of the live mouse with intratumorally administration.

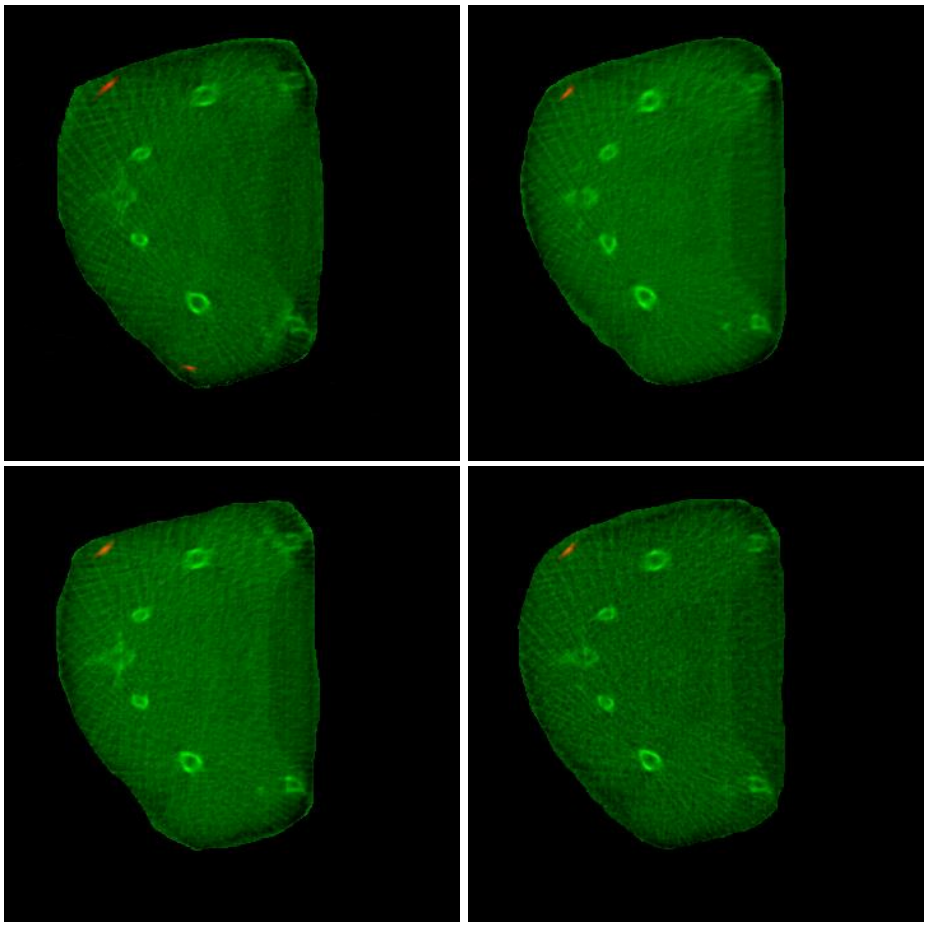

Figure 5.14. The overlaid images of Fig.5.12 and Fig.5.13.

Fig. 5.15 shows the reconstructed 3D results from the live mouse experiment. The 3D XLCT image, 3D parallel beam CT image, and 3D corresponding overlaid image are shown in Fig. 5.15 (left), Fig. 5.15 (middle), and Fig. 5.15 (right), respectively. Here, we have, for the first time, reconstructed 3D in vivo XLCT images of nanoparticles at superhigh resolution and obtained 3D in vivo parallel beam CT image simultaneously.

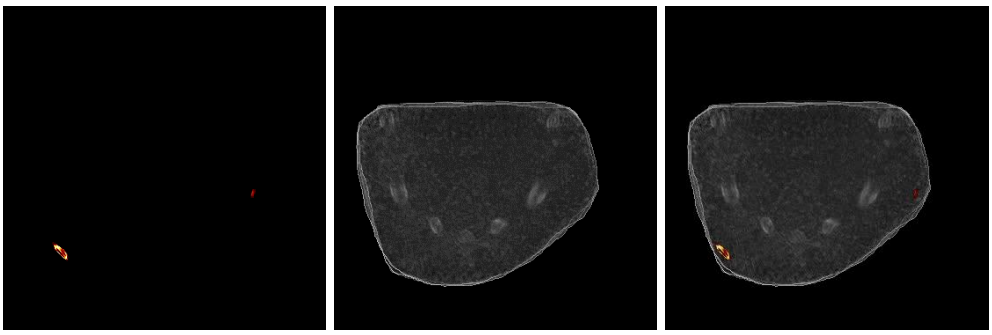

Figure 5.15. Reconstructed 3D XLCT image (left), 3D parallel beam CT image (middle), and 3D overlaid image (right) of the live mouse with intratumorally administration.

5.3.3 Euthanized experiments with intratumorally administration

In Fig. 5.16, we can see the reconstructed cone beam CT images from the euthanized mouse with intratumorally administration. Fig. 5.16 (left) shows the three views of the reconstruction and Fig. 5.16 (right) shows the 3D structure of the mouse. From these results, we can see the two bumps on the mouse body caused by the abdominal tumors.

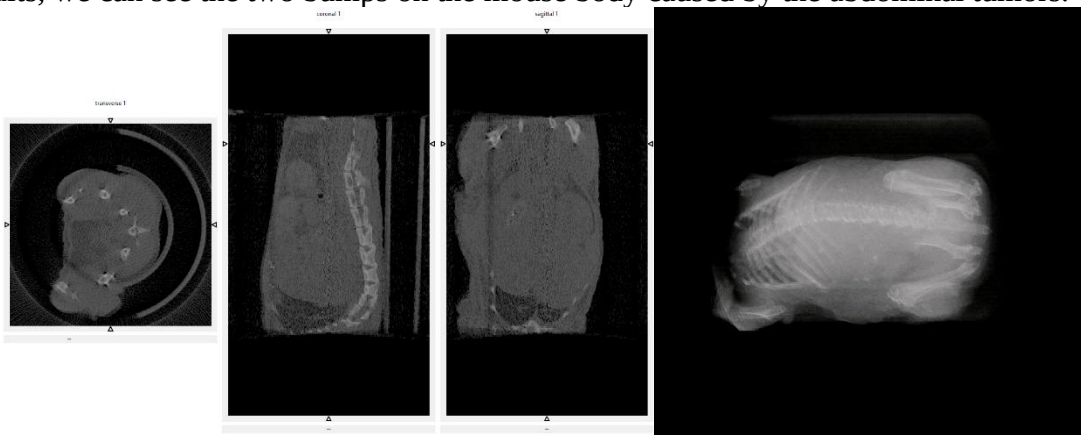

Figure 5.16. Reconstructed cone beam microCT images of the euthanized mouse with intratumorally administration.

Fig. 5.17 and Fig. 5.18 show the reconstructed XLCT images, parallel beam images at the 10 scanning sections. We can see that the left tumor was captured on the 4^{th} and 5^{th} sections and the right tumor was captured on the 6^{th}, 7^{th}, and 8^{th} sections.

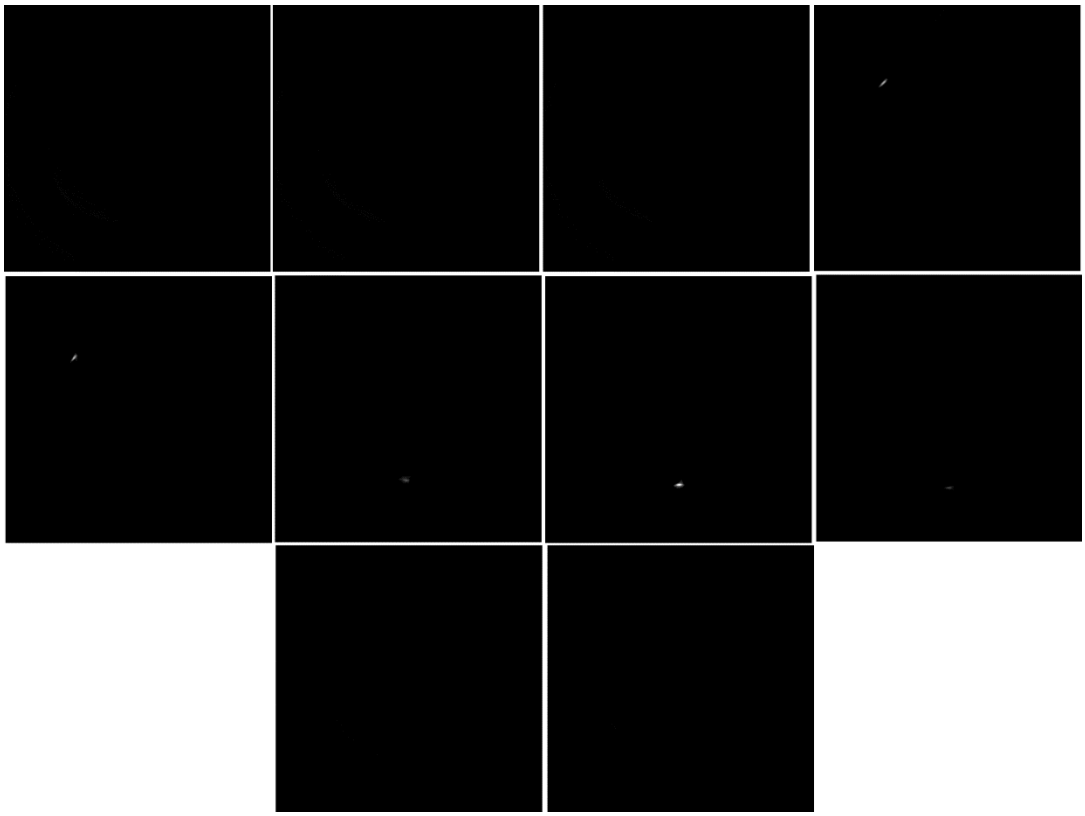

Figure 5.17. Reconstructed XLCT images of the euthanized mouse with intratumorally administration.

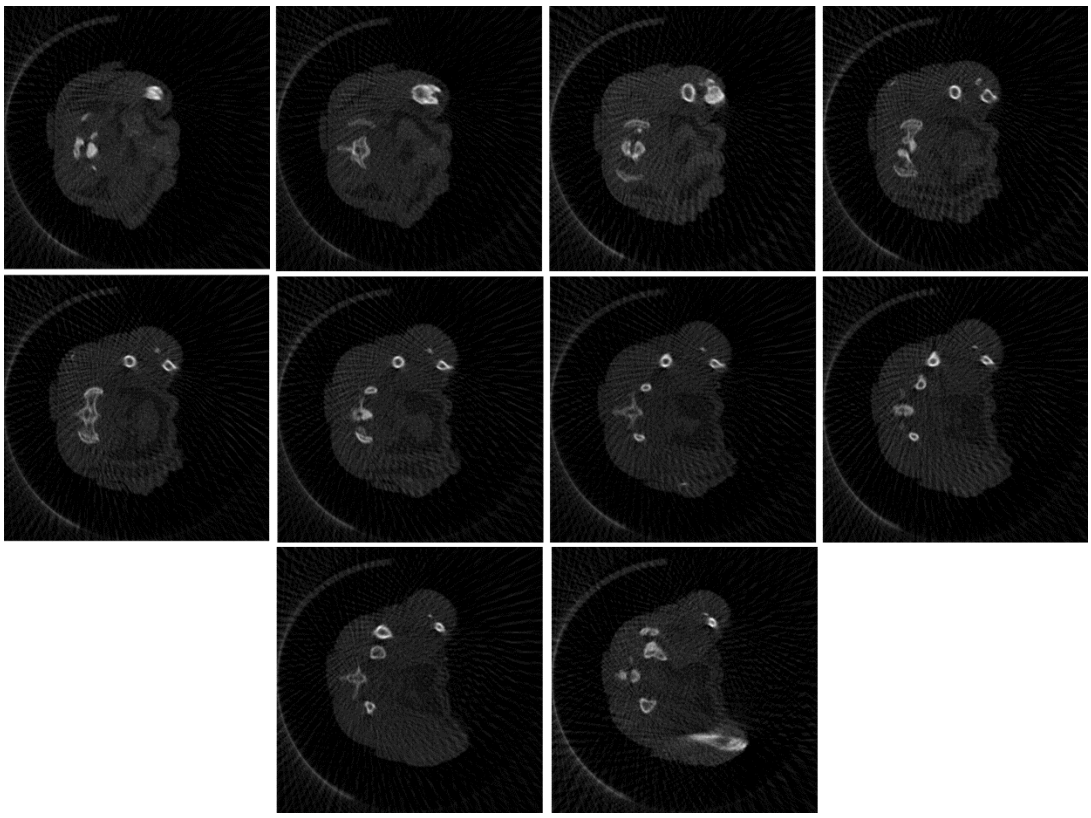

Figure 5.18. Reconstructed parallel beam CT images of the euthanized mouse with intratumorally administration.

The three views of the reconstructed 3D XLCT images, three views of the reconstructed 3D parallel beam CT images, and the three views of the corresponding overlaid images from the euthanized mouse experiment are shown in Fig. 5.19, Fig. 5.20, and Fig. 5.21, respectively. Here, we can see that both tumors were successfully reconstructed at the correct locations.

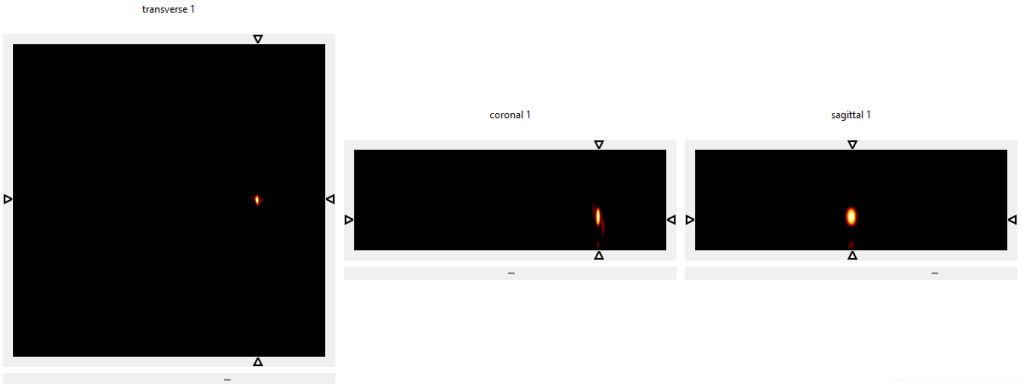

Figure 5.19. Three views of the reconstructed 3D XLCT images from the euthanized mouse with intratumorally administration.

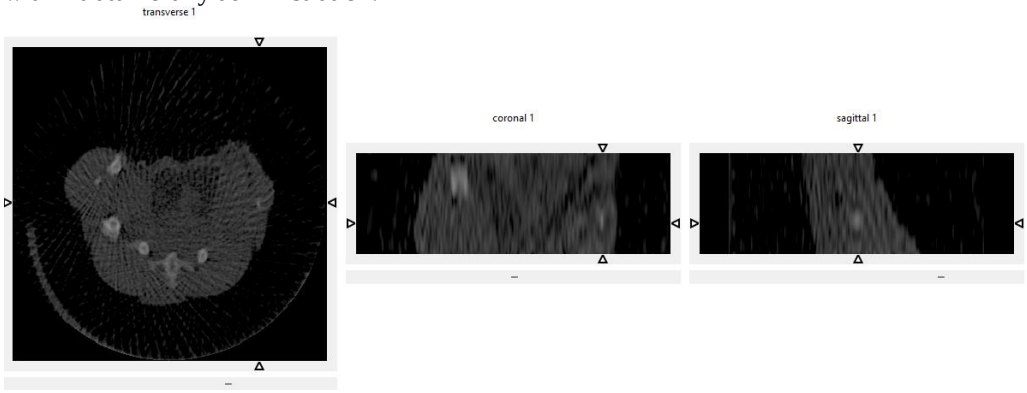

Figure 5.20. Three views of the reconstructed 3D parallel beam CT images from the euthanized mouse with intratumorally administration.

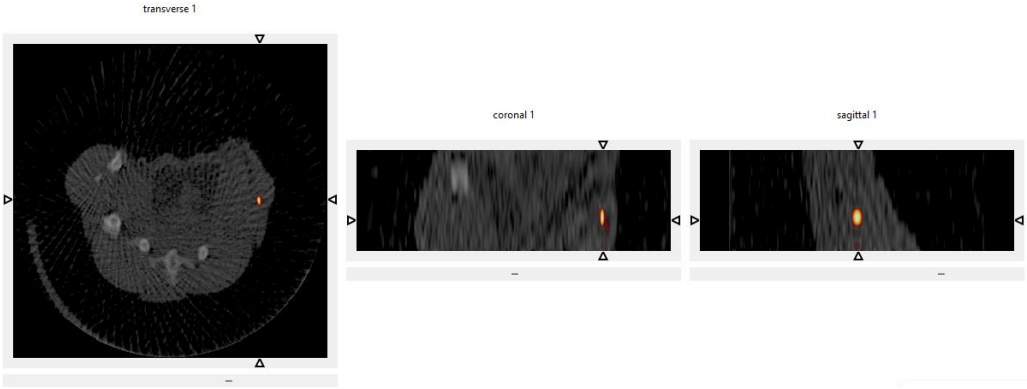

Figure 5.21. The overlaid images of Fig.5.19 and Fig.5.20.

Fig. 5.22 shows the reconstructed 3D results from the euthanized mouse experiment. The 3D XLCT image, 3D parallel beam CT image, and 3D corresponding overlaid image

are shown in Fig. 5.22 (left), Fig. 5.22 (middle), and Fig. 5.22 (right), respectively. We can see both the functional image and the structural image are reconstructed successfully with impressive spatial resolution.

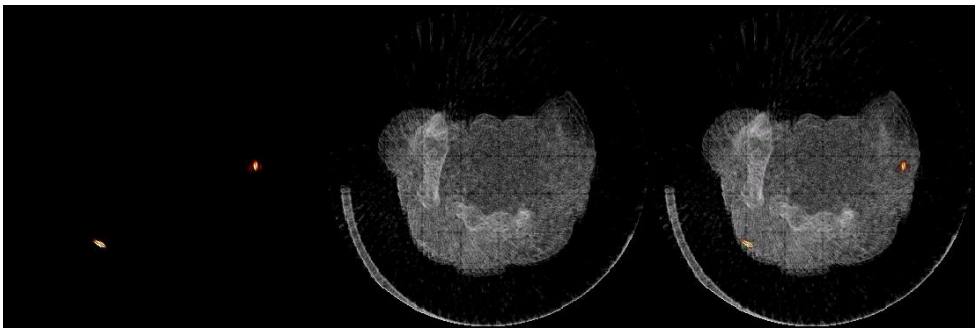

Figure 5.22. Reconstructed 3D XLCT image (left), 3D parallel beam CT image (middle), and 3D overlaid image (right) of the euthanized mouse with intratumorally administration.

5.3.4 Images of the tumor slices

The tumor slices images captured from the EMCCD camera under optical light, excited by cone beam x-rays, and the corresponding overlaid images are shown in Fig. 5.23, Fig. 5.24, and Fig. 5.25, respectively. From the overlaid images, we can find that the injection of the $Gd_2O_2S:Eu^{3+}$ nanoparticles located on from the 64th slice to the 78th slice, where we can calcite the thickness of the injection area is 1.4 to 1.5 mm. The size of the tumor is consistent with the results from the euthanized and in vivo experiments. We can also see that the $Gd_2O_2S:Eu^{3+}$ accumulated on tumor surface and didn't diffuse over a large volume.

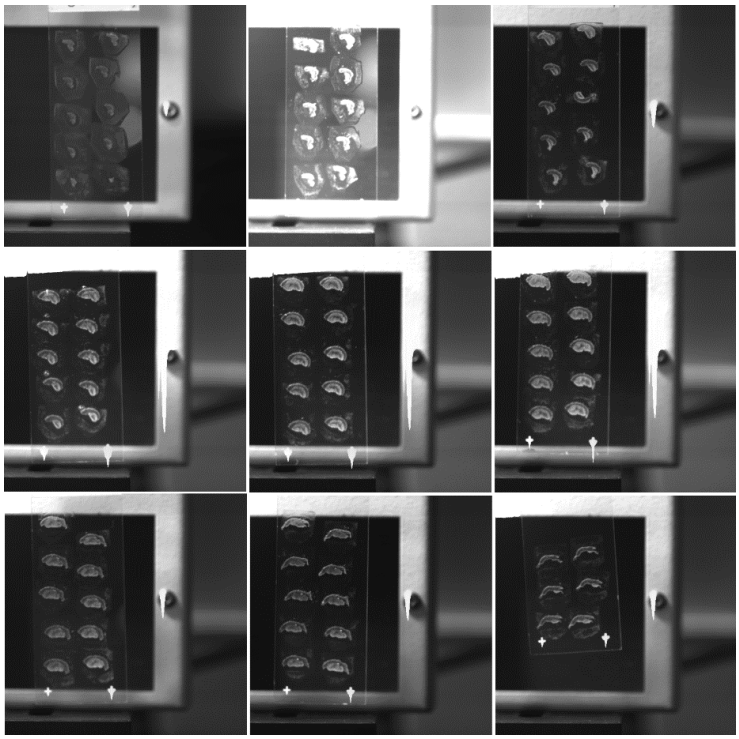

Figure 5.23. Tumor slices images from the EMCCD camera under optical light.

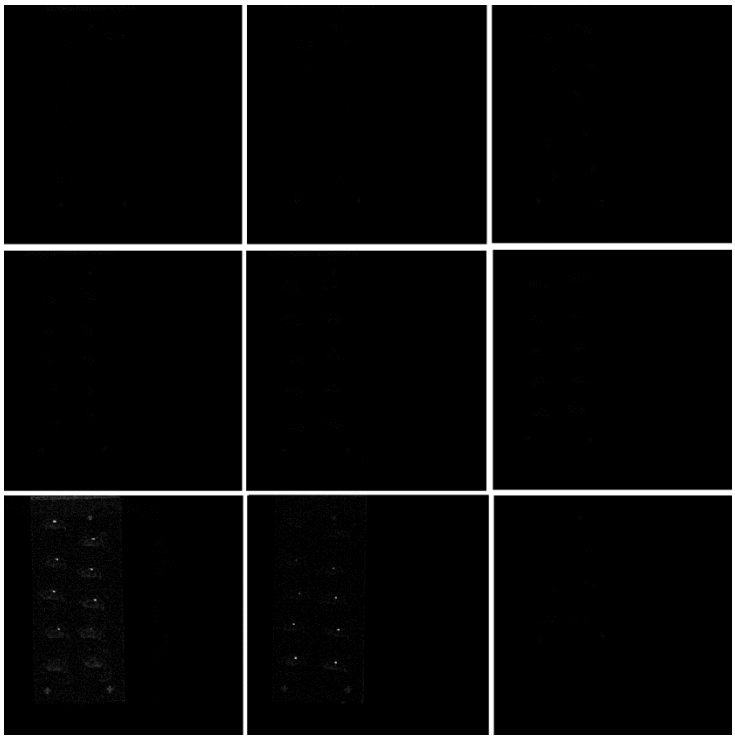

Figure 5.24. Tumor slices images from the EMCCD camera when excited by a cone beam X-ray tube.

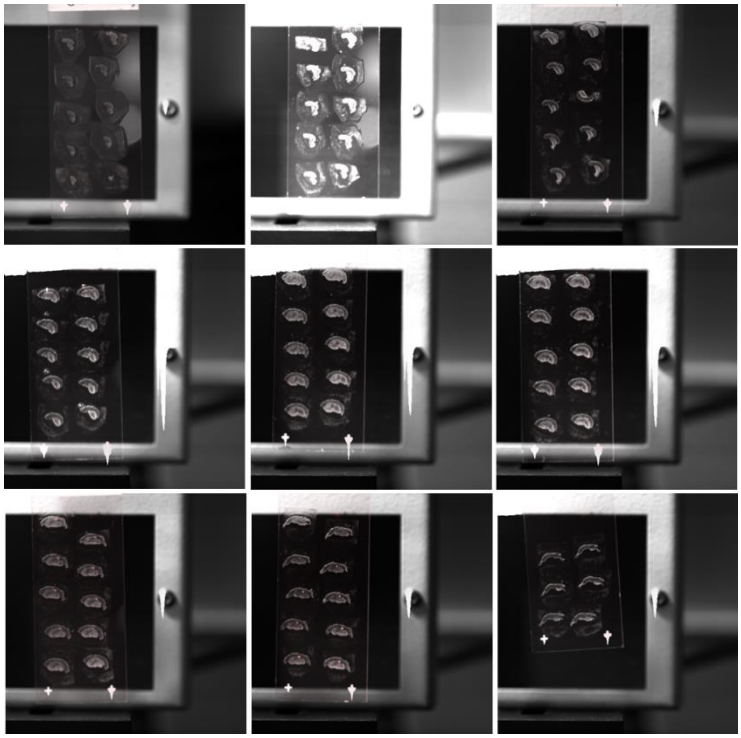

Figure 5.25. The overlaid images of Fig.5.23 and Fig.5.24.

Fig. 5.26 shows the tumor slices images captured from the microscope without and

with the laser excitation. The excitation wavelength of the laser is 570nm. From the images magnified 10 times by the microscope, we can find that the $Gd_2O_2S:Eu^{3+}$ accumulated within a small volume and didn't diffuse during the 2-hours scanning period. The size of the accumulated volume in the images is measured to be 0.7 * 0.19 mm^2 and is consistent with the reconstructed XLCT images.

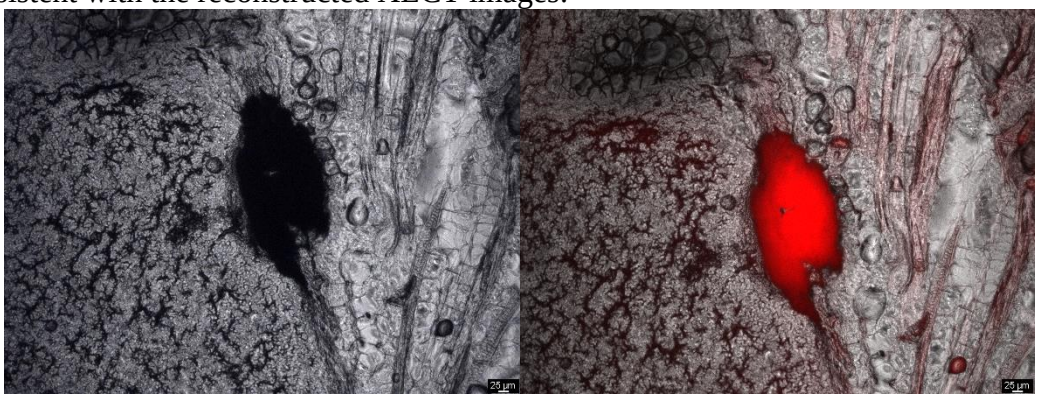

Figure 5.26. Microscopic images of tumor slices: (left) without laser excitation; (right) excited by a laser with an excitation wavelength of 570 nm.

5.4 Discussion and conclusion

In this study, we have, for the first time, reconstructed 3D in vivo XLCT images of nanoparticles at superhigh resolution. We upgraded the FXLT imaging system and added the temperature control system and anesthesia system to keep the mice warm and anesthetized during the experiment. We have performed experiments on euthanized mice with inserted capillary tubes, live mouse with intratumorally administration, and euthanized mouse with intratumorally administration. For each experiment, we performed XLCT and parallel beam CT scan, and microCT scan on the mice. We have achieve 3D in vivo functional and structural images with superhigh spatial resolution, which demonstrated that the FXLT imaging system is a power tool in molecular imaging and has the capabilities of performing in vivo and 3D imaging for small animals. We also have sliced the tumors after XLCT and CT scans and imaged tumors slices with an EMCCD camera and an optical microscope. The cross-validation results is consistent with the results from the FXLT imaging system. In future studies, we will use the machine learning algorithms for better XLCT reconstruction [101] and will apply the low toxic and highly biocompatible nanoparticles to perform intravenous injection in mice experiment.

Acknowledgements: I would like to thank Yibing Zhang who made the capillary tube targets used in the euthanized mice experiments. I also would like to thank Dr. Michael C. Lun who designed the 1st version of the FXLT imaging system. I would like to thank Eva Cai from Dr. Xuecai Ge's lab who implanted the tumors into the mice, injected nanoparticles intratumorally, and sliced the tumors after the experiments. I also would like to thank Vatthana Vongphakham from the department of animal research service who set up the anesthesia system for the mice. And I would like to thank Dr. Jeffrey N. Anker's lab for synthesizing the nanoparticle $Gd_2O_2S:Eu^{3+}$ used in the mice experiments. I have designed the upgraded FXLT imaging system, developed new scanning schemes, built and optimize the system, developed a C++ based program controller, operated the mice experiments, and performed the data analysis and image reconstruction in this work.

CHAPTER 6

CONCLUDING REMARKS AND FUTURE DIRECTIONS FOR XLCT AND XFCT IMAGING

6.1 Concluding Remarks

X-ray luminescence computed tomography (XLCT) has been emerged for over a decade as a novel and promising molecular with the high spatial resolution of X-ray imaging and high molecular sensitivity of optical imaging. XLCT uses an X-ray beam to excite nanophosphors for tomographic imaging, with the emission location defined by the X- ray path and the molecular sensitivity enabled by luminescence probes. Pencil beam-based XLCT is performed using a narrow x-ray beam that raster scans across the sample such as the first-generation computed tomography (CT) scanners, which has shown very high spatial resolution capacity due to the precise spatial encoding of the x-ray beam in the reconstruction algorithm. However, the slow acquisition speed limits its applications for 3D imaging and in vivo imaging. Besides, the current benchtop XLCT imaging system can only be used for phantom studies but incapable for in vivo small imaging. In this dissertation, these challenges were overcome through both software and hardware methods.

We first developed new scanning schemes based on the new data acquisition device and continuous scanning method. We have used a gated photon to replace the high-speed oscilloscope to acquire measurement data. The gated photon counter only counts the photon peaks in each measurement interval, while the oscilloscope records the entire waveform including both background noise data and photon peak data. The photon counter records much less data without losing any relevant information, which results in a much faster data acquisition time. We also developed a fly-scanning scheme to replace the run-and-shoot scheme. In conventional run-and-shoot scheme, the linear stage stops and waits for the oscilloscope to collect data at every measurement interval, which is very time consuming. Under the fly-scanning scheme, the program will collect as much data as possible constantly. Combe the data acquisition device improvement and the scanning method improvements, we have achieved 43 seconds per transverse scan, which is 28.6 times faster than before without compromising the XLCT image quality. With the fly-scanning scheme, 3D in vivo pencil beam-based XLCT imaging is possible to be finished within a reasonable time [72].

The next problem we solved is to build a relationship between the reconstructed XLCT signals and the ground truth concentration of the target. We have made a cylindrical agar phantom containing three groups of targets. Each group was filled with phosphor solution of different concentrations. The phantom was scanned by the upgraded benchtop pencil beam XLCT imaging system. The experimental results are analyzed quantitatively and a linear correlation between the reconstructed signals of the phosphor targets and the target concentrations was found [73].

Next, based on all the study we have done in XLCT imaging field, we have designed, built, and optimized a first-of-its-kind fast focused-x-ray luminescence tomography (FXLT) imaging system. There is a co-designed cone-beam-based microCT imaging system with a flat panel detector on the same rotary gantry of the FXLT system. Therefore, the system is capable of three imaging modalities: XLCT imaging, parallel beam CT imaging and cone beam microCT imaging. The functional XLCT imaging and the structural parallel beam CT imaging can be performed simultaneously in the FXLT scanner. We have developed a lab-made C++ based program controller to automate the experiments. We have performed phantom experiments to evaluate the performance of of the system. The reconstructed result from the phantom experiments has shown that the FXLT imaging system is capable of achieving 3D XLCT images of nanoparticles at superhigh resolution.

In the end, we performed mice experiment to demonstrate the FXLT imaging system has the capabilities of performing in vivo and 3D imaging for small animals. We have performed FXLT and cone beam microCT scans on both euthanized and in vivo mice, with glass capillary tube targets and intratumorally administration. After the experiments with FXLT imaging system, we sliced the tumors in the mice for cross evaluation. The imaging results from the EMCCD camera and microscope has verified the accuracy of the proposed system. We are very proud to say that the FXLT system is a power tool in molecular imaging and has redefine the state of the art in the field of luminescence imaging field in deep tissue.

6.2 Future Directions

6.2.1 Bio-tissue Oxygenation Nanophosphor Enabled Sensing (BONES).

This dissertation has demonstrated the XLCT imaging modality is a powerful tool in biomedical imaging field, it has the potential to be used in more applications. One future work is to image the molecular oxygen with high spatial resolution using XLCT technique. However, there are no x-ray excitable nanoparticles that are sensitive to oxygen. One solution is to attach an x-ray excitable scintillator film to an oxygenation indicator film that is sensitive to the change of molecular oxygen concentration. The oxygenation indicator film contains oxygen-dependent phosphorescence dyes. And when the scintillator film produced x-ray induced optical photons, a portion of the photons can excite fluorescence dyes, which will cause a reduction of the intensity of the detected x-ray luminescence signal.

Following this idea, our collaborator Dr. Jeffrey N. Anker's lab at Clemson University has synthesized the proposed x-ray excitable oxygen sensor films. In these films, the emission spectra of the scintillator is overlapping with the absorption spectra of the oxygen fluorescence dyes. In Phase I, we have performed x-ray luminescent experiments to test these films. Fig. 6.1 shows the schematic diagram and photographs of the system. Here, we measure the emitted x-ray luminescence signals at two different wavelengths at different oxygen concentrations. And the ratio between the detected optical signals at these two wavelengths indicates the oxygenation concentrations. The results shown in Tab. 6.1 and Tab. 6.2 have demonstrated this approach to measure molecular oxygen.

We have designed the prototype BONES system as shown in Fig. 6.2. The future work in Phase II is to perform phantom experiments and small animal studies with oxygen sensor films and the prototype imaging system. Our aim is to achieve high spatial resolution oxygenation quantification in bone marrow [106].

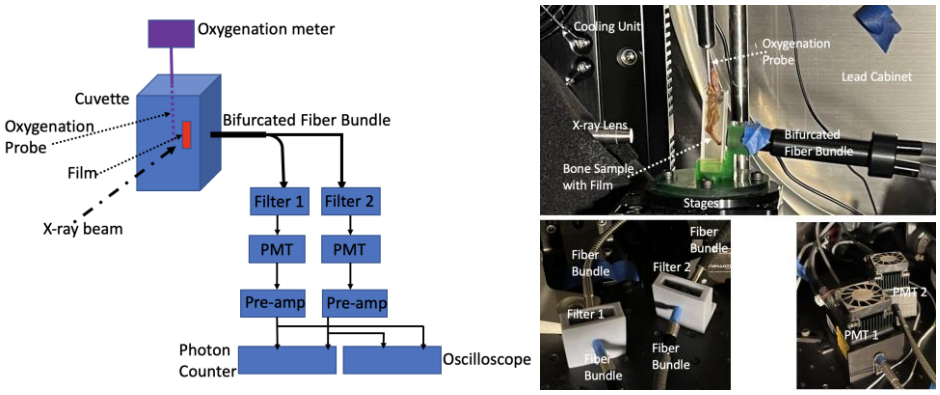

Figure 6.1. Schematic diagram and photographs of the x-ray luminescent system of Phase I.

x-ray on	Count 1	Count 2	Count 3	Count 4	Count 5	Count 6	Count 7	Count 8	Count 9	Count 10
A	11594	11623	11552	11348	11267	11513	11576	11349	11506	11569
B	3966	3684	3836	3991	3915	3900	3812	4037	3949	3812

Table 6.1. Measurements of oxygen sensors at oxygenation of 14%.

x-ray on	Count 1	Count 2	Count 3	Count 4	Count 5	Count 6	Count 7	Count 8	Count 9	Count 10
A	1690	1791	1734	1758	1740	1779	1726	1734	1719	1725
B	1523	1477	1522	1541	1595	1377	1533	1442	1473	1499

Table 6.2. Measurements of oxygen sensors at oxygenation of 0%.

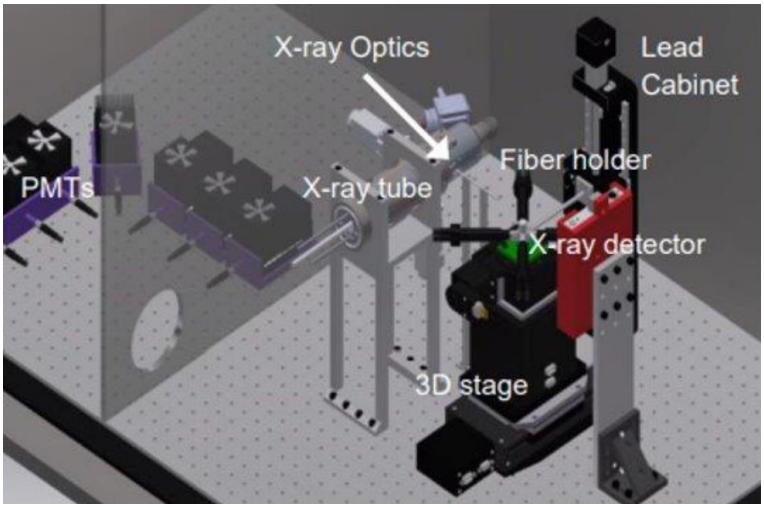

Figure 6.2. CAD design of the BONES prototype system of Phase II.

6.2.2 X-ray fluorescence computed tomography (XFCT) experimental study.

While this dissertation mainly has been forces on XLCT work, it has pointed out an approach to solve the problem laid in XFCT imaging. We have proposed a XFCT imaging system with a superfine pencil beam x-ray source and demonstrate the feasibility in GATE simulation [109-111]. However, the experimental study of XFCT faced challenges.

Fig. 6.3 shows the schematic diagram and photographs of the benchtop XFCT imaging system built in our laboratory. We have used the proposed system to scan an ager phantom (1% intralipid, 2% agar, and 97% water) embedded with one Au target and an air phantom embedded with three Au targets as shown in Fig. 6.4.

However, the reconstructed XFCT image from the ager phantom experiment has low DICE coefficients as shown in Fig. 6.5 (left). And the reconstruction of the air phantom failed due to significant noise aircraft as shown in Fig. 6.5 (right). The possible reason includes the X-ray source (lens (X-Beam Powerflux [Mo anode], XOS) was not bright enough to produce a high x-ray flux and the detection efficiency of the single CdTe detector (X-123CdTe, Amptek) is not enough considering we used up to 20 detectors in the simulation study.

Another solution is to modify and upgrade the reconstruction algorithm. When we were performing experiments in the XLCT and FXLT system, we realized that the fNUMOS algorithm we used in the XFCT reconstruction didn't consider the relative motion between the phantom and the detector. The future study is to develop a new system matrix to take the relative position change into consideration to reduce the noise from the reconstructed image. We also plan to use machine learning algorithms to further improve XFCT imaging quality.

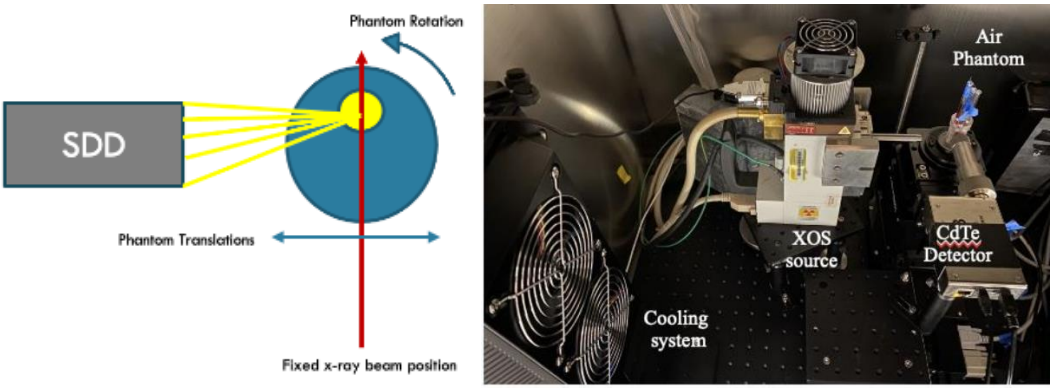

Figure 6.3. Schematic diagram and photographs of the XFCT imaging system.

Figure 6.4. Phantoms scanned by the XFCT system: (left) ager phantom with one Au target; (right) air phantom with three Au targets.

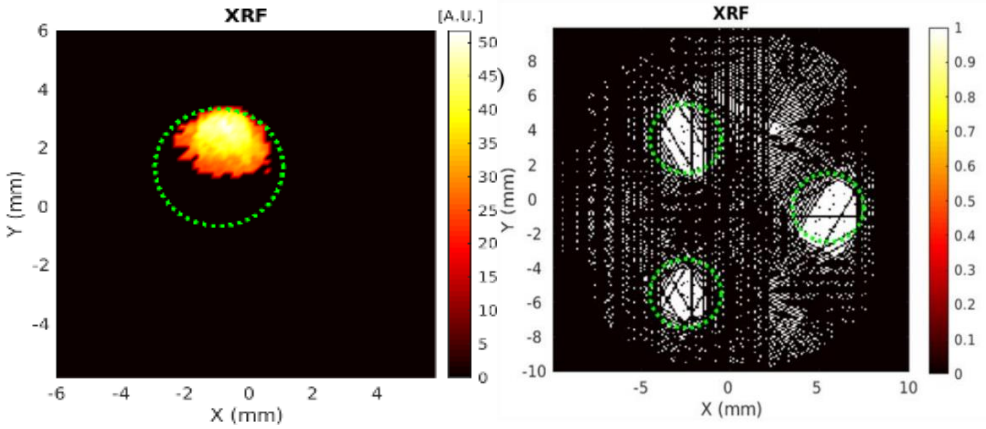

Figure 6.5. Reconstructed XFCT images: (left) phantom with one Au target; (right) phantom with three Au targets.

REFERENCES

[1] R.F. Mould, “The early history of x-ray diagnosis with emphasis on the contributions of physics in 1895-1915”, Phys. Med. Biol. **40** (1995) 1741-1787

[2] François Pontana, Julien Pagniez, Thomas Flohr, Jean-Baptiste Faivre, Alain Duhamel, Jacques Remy, and Martine Remy-Jardin. Chest computed tomography using iterative reconstruction vs filtered back projection (part 1): evaluation of image noise reduction in 32 patients. European radiology, 21 (3): 627–635, 2011

[3] Andrew Webb and George C Kagadis. Introduction to biomedical imaging. Medical Physics, 30 (8): 2267–2267, 2003.

[4] Simon R Cherry, Y Shao, RW Silverman, K Meadors, S Siegel, A Chatziioannou, JW Young, W Jones, JC Moyers, D Newport, et al. MicroPET: a high-resolution PET scanner for imaging small animals. IEEE Transactions on Nuclear Science, 44 (3): 1161– 1166, 1997.

[5] Hendee, W. R., Ritenour, E. R. & Hoffmann, K. R. Medical Imaging Physics, Fourth Edition. Medical Physics 30, 730–730 (2003)

[6] Caravan P. Strategies for increasing the sensitivity of gadolinium-based MRI contrast agents. Chem Soc Rev. 2006;35(6):512-23.

[7] Jinyi Qi and Richard M Leahy. Iterative reconstruction techniques in emission computed tomography. Physics in Medicine & Biology, 51 (15): R541, 2006.

[8] Yang YF, Wu YB, Qi JY, James SS, Du HN, Dokhale PA, Shah KS, Farrell R, Cherry SR. A prototype PET scanner with DOI-encoding detectors. J Nucl Med. 2008;49(7):1132-40. PMCID: PMC2662710.

[9] Peremans K, Cornelissen B, Van den Bossche B, Audenaert K, Van de Wiele C. A review of small animal imaging planar and pinhole SPECT Gamma camera imaging. Vet Radiol Ultrasoun. 2005;46(2):162-70.

[10] Wang G, Cong WX, Durairaj K, Qian X, Shen H, Sinn P, Hoffman E, McLennan G, Henry M. In vivo mouse studies with bioluminescence tomography. Opt Express. 2006;14(17):7801-9

[11] Gao M, Lewis G, Turner GM, Soubret A, Ntziachristos V. Effects of background fluorescence in fluorescence molecular tomography. Appl Opt. 2005;44(26):5468-74

[12] V. Ntziachristos, J. Ripoll, and R. Weissleder, “Would infrared fluorescence signals propagate through large human organs for clinical studies?”, Opt. Lett. **27**, 333-335 (2002)

[13] Zong, W. et al. Fast high-resolution miniature two-photon microscopy for brain imaging in freely behaving mice. Nature Methods **14,** 713–719 (2017)

[14] Yoon, S. et al. Deep optical imaging within complex scattering media. Nature Reviews Physics **2,** 141–158 (2020)

[15] Li CQ, Mitchell G, Dutta J, Ahn S, Leahy R, Cherry S. A three-dimensional multispectral fluorescence optical tomography imaging system for small animals based on a conical mirror design. Opt Express. 2009;17(9):7571-85. PMCID: PMC2852255

[16] Li CQ, Wang G, Qi J, Cherry S. Three-dimensional fluorescence optical tomography in small-animal imaging using simultaneous positron-emission-tomography priors. Opt Lett. 2009;34(19):2933-5. PMCID: PMC2856619.

[17] Thomas Beyer, David W Townsend, Tony Brun, Paul E Kinahan, et al. A combined PET/CT scanner for clinical oncology. The Journal of nuclear medicine, 41 (8): 1369, 2000.

[18] Andreas Boss, Sotirios Bisdas, Armin Kolb, Matthias Hofmann, Ulrike Ernemann, Claus D Claussen, Christina Pfannenberg, Bernd J Pichler, Matthias Reimold, and Lars Stegger. Hybrid PET/MRI of intracranial masses: initial experiences and comparison to PET/CT. Journal of Nuclear Medicine, 51 (8): 1198–1205, 2010

[19] Vernekohl D. X-Ray Excited Fluorescent Materials for Medical Application. Top Med Chem. Vol 9.; 2014:1-68. doi:10.1007/7355

[20] G. Pratx, C.M. Carpenter, C. Sun, R. Rao, and L. Xing, “Tomographic molecular imaging of x-ray excitable nanoparticles”, Opt. Lett. 35, 3345-3347 (2010)

[21] H. Chen, D.E. Longfield, V.S. Varahagiri, K.T. Nguyen, A.L. Patrick, H. Qian, D.G. VanDerveer, and J.N. Anker, “Optical imaging in tissue using X-ray excited luminescenct sensors”, Roy. Chem. Soc. Analyst, **136**, 3438-45 (2011).

[22] H. Chen, A.L. Patrick, Z. Yang, D.G. Vanderveer, and J.N. Anker, “High- resolution Chemical Imaging Through Tissue with an X-ray Scintillator Sensor”, ACS Analy. Chem. **83**, 5045-49 (2011)

[23] Pratx, “A tale of two photons: radioluminescence and its application in molecular imaging”, Proc. of SPIE, Vol. 10049, 1004916 (2017)

[24] Zhang, W., Zhu, D., Zhang, K. & Li, C. Microscopic x-ray luminescence computed tomography. in Multimodal Biomedical Imaging X 9316, 93160M (SPIE, 2015)

[25] G. Pratx, C.M. Carpenter, C. Sun, and L. Xing, "X-ray luminescence computed tomography via selective excitation: a feasibility study", IEEE Trans. Med. Imag 29, 1992-99 (2010)

[26] W. Cong, H. Shen, and G. Wang, ''Spectrally resolving and scattering- compensated X-ray luminescence/fluorescence computed tomography,'' J. Biomed. Opt., vol. 16, no. 6, pp. 066014-1–066014-7, 2011

[27] C. M. Carpenter, C. Sun, G. Pratx, H. Liu, Z. Cheng, and L. Xing, ''Radioluminescent nanophosphors enable multiplexed small-animal imaging,'' Opt. Exp., vol. 20, no. 11, pp. 11598–11604, May 2012

[28] C. Li, K. Di, J. Bec, and S. R. Cherry, ''X-ray luminescence optical tomography imaging: Experimental studies,'' Opt. Lett., vol. 38, no. 13, pp. 2339–2341, Jul. 2013

[29] D. Chen, S. Zhu, H. Yi, X. Zhang, Du. Chen, and J. Liang, "Cone beam x-ray luminescence computed tomography: a feasibility study", Med. Phys. **40** (3) (2013)

[30] G. Zhang, F. Liu, J. Liu, J. Luo, Y. Xie, J. Bai, and L. Xing, "Cone beam x-ray luminescence computed tomography based on Bayesian method", IEEE Trans. on Med. Imag. **36** (1) 225-235 (2017)

[31] X. Liu, Q. Liao, and H. Wang, "In vivo x-ray luminescence tomographic imaging with single-view data", Opt. Lett. **38** (22) (2013)

[32] S. Tzoumas, D. Vernekohl, and L. Xing, "Coded-aperture compressed sensing x-ray luminescence tomography", IEEE Trans. on Biomed. Eng. **65** (8) (2017)

[33] X. Liu, H. Wang, M. Xu, S. Nie, and H. Lu, "A wavelet-based single view reconstruction approach for cone beam x-ray luminescence tomography imaging", Biomed. Opt. Expr. **5** (11) (2014)

[34] W. Cong and G. Wang, "X-ray fan-beam luminescence tomography", Austin J. of Biomed. Eng. **1** (5) (2014).

[35] D. Chen, S. Zhu, X. Cao, F. Zhao, and J. Liang, "X-ray luminescence computed tomography imaging based on X-ray distribution model and adaptively split Bregman method", Biomed. Opt. Expr. **6** (7) (2015)

[36] B. Quigley, C.D. Smith, S. Cheng, J.S. Souris, C.A. Pelizarri, C. Chen, L. Lo, C.S. Reft, R.D. Wiersma, and P.J. La Riviere, "Sensitivity evaluation and selective plane

imaging geometry for x-ray induced luminescence imaging", Med. Phys. **44** (10) 5367-5377 (2017)

[37] P. Boisseau and L. Grodzins, ‘‘Fluorescence tomography using synchrotron radiation at the NSLS,’’ Hyperfine Interact., vol. 33, nos. 1–4, pp. 283–292, Mar. 1987.

[38] T. Takeda et al., ‘‘X-ray fluorescent CT imaging of cerebral uptake of stable-iodine perfusion agent iodoamphetamine analog IMP in mice,’’ J. Synchrotron Radiat., vol. 16, no. 1, pp. 57–62, Jan. 2009.

[39] S.-K. Cheong, B. L. Jones, A. K. Siddiqi, F. Liu, N. Manohar, and S. H. Cho, ‘‘X-ray fluorescence computed tomography (XFCT) imaging of gold nanoparticle-loaded objects using 110 kVp X-rays,’’ Phys. Med. Biol., vol. 55, no. 3, pp. 647–662, Feb. 2010.

[40] M. Bazalova, Y. Kuang, G. Pratx, and L. Xing, ‘‘Investigation of X-ray fluorescence computed tomography (XFCT) and K-edge imaging,’’ IEEE Trans. Med. Imag., vol. 31, no. 8, pp. 1620–1627, Aug. 2012

[41] Y. Kuang, G. Pratx, M. Bazalova, B. Meng, J. Qian, and L. Xing, ‘‘First demonstration of multiplexed X-ray fluorescence computed tomography (XFCT) imaging,’’ IEEE Trans. Med. Imag., vol. 32, no. 2, pp. 262–267, Feb. 2013.

[42] B. L. Jones, N. Manohar, F. Reynoso, A. Karellas, and S. H. Cho, ‘‘Experimental demonstration of benchtop X-ray fluorescence computed tomography (XFCT) of gold nanoparticle-loaded objects using lead- and tin-filtered polychromatic cone-beams,’’ Phys. Med. Biol., vol. 57, no. 23, p. N457, Dec. 2012.

[43] Fu G, Meng L-J, Eng P, Newville M, Vargas P, La Riviere P. Experimental demonstration of novel imaging geometries for x-ray fluorescence computed tomography. Medical Physics. 2013;40:061903, 11

[44] H. M. Hertz, J. C. Larsson, U. Lundström, D. H. Larsson, and C. Vogt, ‘‘Laboratory X-ray fluorescence tomography for high-resolution nanopar- ticle bio-imaging,’’ Opt. Lett., vol. 39, no. 9, pp. 2790–2793, May 2014.

[45] L. Vincze et al., ‘‘Three-dimensional trace element analysis by confocal X-ray microfluorescence imaging,’’ Anal. Chem., vol. 76, no. 22, pp. 6786–6791, Nov. 2004.

[46] N. Gao, I. Y. Ponomarev, Q. F. Xiao, W. M. Gibson, and D. A. Carpenter, ‘‘Monolithic polycapillary focusing optics and their applications in microbeam X-ray fluorescence,’’ Appl. Phys. Lett., vol. 69, no. 11, pp. 1529–1531, Sep. 1996.

[47] A. R. Woll et al., ‘‘Development of confocal X-ray fluorescence (XRF) microscopy at the Cornell high energy synchrotron source,’’ Appl. Phys. A, vol. 83, no. 2, pp. 235–238, May 2006.

[48] F. E. Carroll, M. H. Mendenhall, R. H. Traeger, C. Brau, and J. W. Waters, ‘‘Pulsed tunable monochromatic X-ray beams from a compact source: New opportunities,’’ Amer. J. Roentgenol., vol. 181, no. 5, pp. 1197–1202, Nov. 2003

[49] K. Nakajima, ‘‘Compact X-ray sources: Towards a table-top free-electron laser,’’ Nature Phys., vol. 4, no. 2, pp. 92–93, Feb. 2008.

[50] M. Ahmad, M. Bazalova, L. Xiang, and L. Xing, ‘‘Order of magnitude sensitivity increase in X-ray fluorescence computed tomography (XFCT) imaging with an optimized spectro-spatial detector configuration: Theory and simulation,’’ IEEE Trans. Med. Imag., vol. 33, no. 5, pp. 1119–1128, May 2014.

[51] Bazalova-Carter M. The potential of L-shell X-ray fluorescence CT (XFCT) for molecular imaging. Br J Radiol. 2015;88(1055). doi:10.1259/bjr.20140308

[52] Vernekohl D, Ahmad M, Dai X, Zhao W, Cheng K, Xing L (2019) Reduced acquisition time for L-shell x-ray fluorescence computed tomography using polycapillary x-ray optics. Med Phys

[53] Vernekohl D. X-Ray Excited Fluorescent Materials for Medical Application. In: Top Med Chem. Vol 9; 2014:1-68. doi:10.1007/7355

[54] Naczynski DJ, Sun C, Turkcan S, Jenkins C, Koh AL, Ikeda D, Pratx G, Xing L (2015) X-ray induced shortwave infrared biomedical imaging using rare-earth nanoprobes. Nano Lett 15:96–102

[55] Xing MM, Cao WH, Pang T, Ling XQ, Chen N. Preparation and characterization of monodisperse spherical particles of X-ray nano-phosphors based on Gd2O2S:Tb. Chinese Sci Bull. 2009;54(17):2982-6

[56] Sudheendra L, Das GK, Li CQ, Stark D, Cena J, Cherry S, Kennedy IM. NaGdF4:Eu3+ Nanoparticles for Enhanced X-ray Excited Optical Imaging. Chem Mater. 2014;26(5):1881-8. PMCID: PMC3985768

[57] Hainfeld JF, Powell RD. New frontiers in gold labeling. J Histochem Cytochem. 2000;48(4):471-80

[58] Sun C, Pratx G, Carpenter CM, Liu HG, Cheng Z, Gambhir SS, Xing L. Synthesis and Radioluminescence of PEGylated Eu3+-doped Nanophosphors as Bioimaging Probes. Adv Mater. 2011;23(24):H195-H9. PMCID: PMC4145869

[59] Karathanasis E, Chan L, Karumbaiah L, McNeeley K, D'Orsi CJ, Annapragada AV, Sechopoulos I, Bellamkonda RV. Tumor Vascular Permeability to a Nanoprobe Correlates to Tumor-Specific Expression Levels of Angiogenic Markers. Plos One. 2009;4(6).

PMCID: PMC2688084.

[60] Kuang Y, Pratx G, Bazalova M, Qian J, Meng B, Xing L (2013) Development of XFCT imaging strategy for monitoring the spatial distribution of platinum-based chemodrugs: instru- mentation and phantom validation. Med Phys 40:030701

[61] Bazalova M, Ahmad M, Pratx G, Xing L. L-shell x-ray fluorescence computed tomography (XFCT) imaging of Cisplatin. Phys Med Biol. 2014;59(1):219-232. doi:10.1088/0031-9155/59/1/219

[62] Geraki K, Farquharson MJ, Bradley DA (2002) Concentrations of Fe, Cu and Zn in breast tissue: a synchrotron XRF study. Phys Med Biol 47:2327

[63] Costello LC, Franklin RB (1998) Novel role of zinc in the regulation of prostate citrate metabolism and its implications in prostate cancer. Prostate 35:285–296

[64] Larsson, J.C.; Vogt, C.; Vågberg, W.; Toprak, M.S.; Dzieran, J.; Arsenian-Henriksson, M.; Hertz, H.M. High-spatial-resolution X-ray fluorescence tomography with spectrally matched nanoparticles. Phys. Med. Biol. 2018, 63

[65] Shilo, M.; Reuveni, T.; Motiei, M.; Popovtzer, R. Nanoparticles as computed tomography contrast agents: Current status and future perspectives. Nanomedicine 2012, 7

[66] Hainfeld, J.F.; Slatkin, D.N.; Smilowitz, H.M. The use of gold nanoparticles to enhance radiotherapy in mice. Phys. Med. Biol. 2004, 49

[67] Jiang, S.; He, P.; Deng, L.; Chen, M.; Wei, B. Monte Carlo Simulation for Polychromatic X-ray Fluorescence Computed Tomography with Sheet-Beam Geometry. Int. J. Biomed. Imaging 2017

[68] B. L. Jones and S. H. Cho, "The feasibility of polychromatic cone-beam X-ray fluorescence computed tomography (XFCT) imaging of gold nanoparticle-loaded objects: a Monte Carlo Study," Physics in Medicine and Biology, vol. 56, no. 12, pp. 3719–3730, 2011.

[69] M. C. Lun, Y. Fang, and C. Li, "Fast three-dimensional focused x-ray luminescence computed tomography," in Medical Imaging 2021: Biomedical Applications in Molecular, Structural, and Functional Imaging, B. S. Gimi and A. Krol, Eds., Online Only, United States: SPIE, Feb. 2021, p. 44. doi: 10.1117/12.2584335.

[70] M. C. Lun, Y. Fang, and C. Li, "Focused X-ray Luminescence Computed Tomography using a Continuous Scanning Scheme," Bioengineering, preprint, Feb. 2021. doi: 10.1101/2021.02.04.429805.

[71] Y. Fang, M. C. Lun, Y. Zhang, J. N. Anker, G. Wang, and C. Li, "Super-fast three-dimensional focused x-ray luminescence computed tomography with a gated photon counter," in Medical Imaging 2022: Biomedical Applications in Molecular, Structural, and Functional Imaging, B. S. Gimi and A. Krol, Eds., San Diego, United States: SPIE,

Apr. 2022, p. 8. doi: 10.1117/12.2613157.

[72] Y. Fang, Y. Zhang, M. C. Lun, and C. Li, “Superfast Scan of Focused X-Ray Luminescence Computed Tomography Imaging,” IEEE Access, vol. 11, pp. 134183–134190, 2023, doi: 10.1109/ACCESS.2023.3336615.

[73] Y. Fang, Y. Zhang, and C. Li, “Quantitative study of x-ray luminescence computed tomography,” in Medical Imaging 2024: Clinical and Biomedical Imaging, B. S. Gimi and A. Krol, Eds., San Diego, United States: SPIE, Apr. 2024, p. 37. doi: 10.1117/12.3009033.

[74] Y. Fang, Y. Zhang, M. C. Lun, J. N. Anker, G. Wang, and C. Li, “Development of fast and three-dimensional focused x-ray luminescence tomography system,” in Medical Imaging 2023: Biomedical Applications in Molecular, Structural, and Functional Imaging, B. S. Gimi and A. Krol, Eds., San Diego, United States: SPIE, Apr. 2023, p. 34. doi: 10.1117/12.2654091.

[75] M.C. Lun and C. Li, "High-resolution x-ray luminescence computed tomography," Proc. of SPIE 11317, Medical Imaging 2020: Biomedical Applications in Molecular, Structural, and Functional Imaging; 11317D (2020).

[76] M.C. Lun, W. Zhang, and C. Li, "Sensitivity study of x-ray luminescence computed tomography," Appl. Opt. 56 (11), 3010-9 (2017).

[77] G. Pratx, C.M. Carpenter, C. Sun, R. Rao, and L. Xing, "Tomographic molecular imaging of x-ray excitable nanoparticles," Opt. Lett. 35, 3345- 3347 (2010).

[78] G. Pratx, C.M. Carpenter, C. Sun, and L. Xing, "X-ray Luminescence Computed Tomography via Selective Excitation: A Feasibility Study," IEEE Trans. Med. Imag. 29 (12), 1992-1999 (2010).

[79] C. Li, G.S. Mitchell, J. Dutta, S. Ahn, R.M. Leahy, and S.R. Cherry, "A three-dimensional multispectral fluorescence optical tomography imaging system for small animals based on a conical mirror design," Opt. Expr. 17 (9), 7571-7585 (2009).

[80] C. Li, G. Wang, J. Qi, and S. Cherry, "Three-dimensional fluorescence optical tomography in small-animal imaging using simultaneous positron- emission-tomography priors," Optics Letters, 34(19), 2933-2935 (2009).

[81] H. M. Hertz, J. C. Larsson, U. Lundstrom, D. H. Larsson, and C. Vogt, "Laboratory x-ray fluorescence tomography for high-resolution nanoparticle bio-imaging," Opt Lett, 39(9), 2790-3 (2014).

[82] G. Zhang et al., "Cone Beam X-ray Luminescence Computed Tomography Based on Bayesian Method," in IEEE Transactions on Medical Imaging, vol. 36, no. 1, pp. 225-235, Jan. 2017.

[83] D. Chen, S. Zhu, H. Yi, X. Zhang, D. Chen, J. Liang, and J. Tian, “Cone beam x-ray

luminescence computed tomography: A feasibility study," Med. Phys., 40: 031111 (2013).

[84] X. Chen, J. Liang, X. Cao, D. Yang, D. Chen, J. Ripoll, J. Tian, "Feasibility study of endoscopic x-ray luminescence computed tomography: Simulation demonstration and phantom application.," Journal of Applied Physics, 114 (8), 084701 (2013).

[85] T. Liu, J. Rong, P. Gao, H. Pu, W. Zhang, X. Zhang, Z. Liang, H. Lu, "Regularized reconstruction based on joint L1 and total variation for sparse- view cone-beam X-ray luminescence computed tomography," Biomed. Opt. Express, 10(1), 1-17 (2019).

[86] H. Pu, P. Gao, Y. Liu, J. Rong, F. Shi and H. Lu, "Principal Component Analysis Based Dynamic Cone Beam X-Ray Luminescence Computed Tomography: A Feasibility Study," in IEEE Transactions on Medical Imaging, 38(12), 2891-2902 (2019).

[87] W. Zhang, M.C. Lun, A. Nguyen, and C. Li, "A focused x-ray beam based x-ray luminescence computed tomography," J. of Biomed. Opt. 22 (11), 116004 (2017).

[88] M.C. Lun, M. Ranasinghe, M. Arfuzzman, Y. Fang, Y. Guo, J. Anker, and C. Li, "Investigation of contrast agents for x-ray luminescence computed tomography", Applied Optics, 60 (23), 6769-6775 (2021).

[89] Y. Zhang, M.C. Lun, C. Li, and Z. Zhou, "Method for improving the spatial resolution of narrow x-ray beam-based x-ray luminescence computed tomography imaging," J. Biomed. Opt. 24(8), 086002 (2019).

[90] M.C. Lun, Y. Fang, and C. Li, "Focused X-ray Luminescence Computed Tomography using a Continuous Scanning Scheme," bioRxiv 2021.02.04.429805.

[91] M.C. Lun, Y. Fang, and C. Li, "Fast three-dimensional focused x-ray luminescence computed tomography," Proc. of SPIE 116001, Medical Imaging 2021: Biomedical Applications in Molecular, Structural, and Functional Imaging; 116001B (2021).

[92] Y. Fang, M.C. Lun, Y. Zhang, J. Anker, G. Wang, and C. Li, "Super-fast three-dimensional focused x-ray luminescence computed tomography with a gated photon counter," Proc. of SPIE 120360, Medical Imaging 2022: Biomedical Applications in Molecular, Structural, and Functional Imaging; 120360K (2022).

[93] Eric D. Jones, Bryan L. Preppernau, and James R. Matey, Department Editor, "Catching the Right Bus V: A Beginners' Guide to Programming the IEEE-488 Bus," Computers in Physics 9, 140-147 (1995).

[94] Y. Fang, Y. Zhang, M.C. Lun, J. Anker, G. Wang, and C. Li, "Development of fast and three-dimensional focused x-ray luminescence tomography system," Proc. of SPIE 12468, Medical Imaging 2023: Biomedical Applications in Molecular, Structural, and Functional Imaging; 124680Z (2023).

[95] C. Li, A. Martinez-Davalos, and S. R. Cherry, "Numerical simulation of x- ray

luminescence optical tomography for small-animal imaging," Journal of biomedical optics, vol. 19, no. 4, pp. 46002, 2014-Apr-1, 2014.

[96] D. Zhu, Y. Zhao, R. Baikejiang, Z. Yuan, and C. Li, "Comparison of regularization methods in fluorescence molecular tomography," Photonics, 1, 95-109 (2014).

[97] D. Zhu and C. Li, "Nonconvex regularizations in fluorescence molecular tomography for sparsity enhancement," Phys. Med. Biol. 59, 2901–2912 (2014).

[98] D. Zhu and C. Li, "Nonuniform update for sparse target recovery in fluorescence molecular tomography accelerated by ordered subsets," Biomed. Opt. Express 5, 4249–4259 (2014).

[99] D. Zhu and C. Li, "Accelerated image reconstruction in fluorescence molecular tomography using a non-uniform updating scheme with momentum and ordered subsets methods," J. Biomed. Opt. 21, 016004 (2016).

[100] W. Zhang, D. Zhu, M.C. Lun, C. Li, "Multiple pinhole collimator based X-ray luminescence computed tomography", Biomedical Optics Express, 7, 2506-2523 (2016).

[101] M.C. Lun, W. Cong, M. Arfuzzman, M. Ranasinghe, S. Bhattacharya, J. Anker, G. Wang, and C. Li, "Focused x-ray luminescence imaging system for small animals based on a rotary gantry," Journal of Biomedical Optics, 26(3), 036004 (2021).

[102] T Wang, Z Nie, R Wang, Q Xu, H Huang, H Xu, F Xie, XJ Liu, "PneuNet: deep learning for COVID-19 pneumonia diagnosis on chest X-ray image analysis using Vision Transformer," Med Biol Eng Comput, 61, 1395–1408 (2023).

[103] Y. Zhang, D. Hu, W. Li, W. Zhang, R.C. Chen, Y. Chen, H. Gao, "2V- CBCT: Two-Orthogonal-Projection Based CBCT Reconstruction and Dose Calculation from Real CBCT Projection Data," International Journal of Radiation Oncology Biology Physics, 117(2), 0360-3016 (2023).

[104] Ke Li, Jie Tang, and Guang-Hong Chen, "Statistical model based iterative reconstruction (mbir) in clinical ct systems: Experimental assessment of noise performance," Medical Physics, 41(4):041906, 2014.

[105] Mareike Thies, Fabian Wagner, Noah Maul, Lukas Folle, Manuela Meier, Maximilian Rohleder, Linda-Sophie Schneider, Laura Pfaff, Mingxuan Gu, Jonas Utz, Felix Denzinger, Michael Manhart, and Andreas Maier, "Gradient- based geometry learning for fan-beam ct reconstruction," Physics in Medicine Biology, 68(20):205004, oct 2023.

[106] Y. Zhang et al., “Oxygenation imaging in deep tissue with x-ray luminescence computed tomography (XLCT),” in Medical Imaging 2023: Biomedical Applications in Molecular, Structural, and Functional Imaging, B. S. Gimi and A. Krol, Eds., San Diego, United States: SPIE, Apr. 2023, p. 16. doi: 10.1117/12.2654446.

[107] Y. Fang, Y. Zhang, and C. Li, “Pencil Beam Based X-ray Luminescence Computed Tomography Imaging of Deep Targets Three-dimensionally and Quantitatively.” doi: 10.1101/2024.05.28.596355.

[108] Kai Yang, Alexander L. C. Kwan, DeWitt F. Miller, and John M. Boone, “A geometric calibration method for cone beam CT systems”, Medical Physics 33, 1695 (2006).

[109] I. Romero, Y. Fang, M. C. Lun, and C. Li, “Benchtop x-ray fluorescence computed tomography (XFCT) imaging,” in Medical Imaging 2021: Biomedical Applications in Molecular, Structural, and Functional Imaging, B. S. Gimi and A. Krol, Eds., Online Only, United States: SPIE, Feb. 2021, p. 38. doi: 10.1117/12.2584577.

[110] I. O. Romero, Y. Fang, and C. Li, “Correlation between X-ray tube current exposure time and X-ray photon number in GATE,” XST, vol. 30, no. 4, pp. 667–675, Aug. 2022, doi: 10.3233/XST-221126.

[111] I. O. Romero, Y. Fang, M. Lun, and C. Li, “X-ray Fluorescence Computed Tomography (XFCT) Imaging with a Superfine Pencil Beam X-ray Source,” Photonics, vol. 8, no. 7, p. 236, Jun. 2021, doi: 10.3390/photonics8070236.